Stony Brook University

A Look at Heavy Ion Collisions Through the SO(3)-Invariant Flow

A Dissertation Presented

by

María del Pilar Staig Fernández

to

The Graduate School

in Partial Fulfillment of the Requirements

for the Degree of

Doctor of Philosophy

in

Physics

Stony Brook University

August 2013

Stony Brook University

The Graduate School

María del Pilar Staig Fernández

We, the dissertation committee for the above candidate for the Doctor of Philosophy degree, hereby recommend acceptance of this dissertation.

Edward Shuryak – Dissertation Advisor
Distinguished Professor, Department of Physics and Astronomy

Clark McGrew – Chairperson of Defense
Associate Professor, Department of Physics and Astronomy

Axel Drees
Professor, Department of Physics and Astronomy

Roy Lacey
Professor, Department of Chemistry

Larry McLerran
Senior Scientist, Brookhaven National Laboratory

This dissertation is accepted by the Graduate School.

Charles Taber
Interim Dean of the Graduate School

Abstract of the Dissertation

A Look at Heavy Ion Collisions Through the SO(3)-Invariant Flow

by

María del Pilar Staig Fernández

Doctor of Philosophy

in

Physics

Stony Brook University

2013

One of the measurements obtained from heavy ion collisions is the correlation between two final particles as a function of the difference of azimuthal angle and pseudorapidity. These correlations show structure in the azimuthal direction that is elongated in pseudorapidity, and that has its origin in the initial state after the collision, and in its evolution.

We implemented a Glauber Monte Carlo code to study initial state fluctuations that appear on an event by event basis because of the random positions of the nucleons in the nuclei. We calculated the initial average deformations and their fluctuations as a function of the centrality of the collision and found that for central collisions all of the asymmetry parameters are on equal footing, but that as the collisions become more peripheral the second asymmetry parameter becomes more important, because of the almond-like shape of the region where the two nuclei intersect.

To study the evolution of the matter created after the collision

we used the SO(3)-invariant flow developed by S. Gubser and A. Yarom, that is an extension of Bjorken flow that includes flow in the radial direction. The hydrodynamic equations including perturbations to this background can be solved analytically in terms of known special functions that can be collected to describe the shape of a specific perturbation. We used as initial condition a Gaussian perturbation, and found that the two particle correlation obtained resembles the curve from experiments. We also explored the effects of viscosity on the final particle correlation, and on the spectra of the flow coefficients, and found that viscosity kills the higher harmonics.

The same method can be used to study other perturbations to the background. In particular, we studied fluctuations that appear near the critical temperature produced by Quark Gluon Plasma clusters undergoing a Rayleigh type collapse, and suggest that the observed widening in rapidity correlations may be an indication of sound propagating from such fluctuations.

Contents

List of Figures

viii

List of Tables

Acknowledgements

I would like to give thanks first of all to Edward Shuryak for all the interesting projects and ideas that helped me put the present work together. He has been a great advisor, full of patience, and always available for lengthy and detailed discussions about our projects. All the knowledge and insights that he has shared with me have been very beneficial for my education.

I also would like to thank the members of the committee Axel Drees, Roy Lacey, Clark McGrew, and Larry McLerran, for agreeing to participate in this defense.

Thanks to all the occupants of office C-115, Alex, Frasher, Li and Savvas, for all the conversations, and for making the office a lively place.

I would like to give thanks to all my friends at Stony Brook for the good times, especially to the latin american comunity, Aníbal, Marcos, Melvin, Pedro, Raquel, and Raul, for making me feel more at home.

Thanks to Diane Vigliotta and Sara Lutterbie, for all the help with administrative issues, and to my international student advisor Gretchen Gosnel for all the help with the visa and the work authorization.

I came to do my Ph.D. with a Fulbright-CONICYT scholarship, and I would like to acknowledge both institutions. I give thanks to the Fullbright program for sponsoring my visa, and to CONICYT for financing the first four years of my studies at Stony Brook.

Finally, I would like to thank Pedro Liendo, for his support and patience, and for sharing every day of this adventure with me.

Chapter 1

Introduction

The history of nuclear matter can be traced back to the early XX century, when Ernst Rutherford discovered the nucleus in 1911 [1]. More than a hundred years later the knowledge of nuclear physics has increased immensely, both theoretically and experimentally. Together with the proton and the neutron–the particles that form the atomic nucleus–an immense zoo of particles, named hadrons, has been discovered. The existence of all of these particles, which puzzled the community for years as more and more of what were thought to be elementary particles appeared, was solved in 1964 by the quark model [2–4], that proposed that the hadrons were in fact not elementary particles, but composite particles made out of quarks. The theory describing quarks and their interactions is known as Quantum Chromodynamics (QCD): quarks are said to come come in three different colors (charges of the strong force) and their interactions are mediated by colored bosons named gluons. At everyday energies colored particles are always bound together in color neutral combinations (mesons and baryons). This property of QCD known as confinement, ceases to exist for larger energies, when the force between quarks decreases in a phenomenon known as asymptotic freedom [5, 6]. This happens because the strong coupling constant is not a fixed parameter, it depends on the energy scale: it is large for small energies and small for large energies as Figure (1.1) exemplifies.

At high temperature and high energy density a new phase of nuclear matter, characterized for being composed of deconfined quarks and gluons, is created. The necessary conditions to create this new state of matter, known by the name Quark Gluon Plasma (QGP)–term coined in [8]– existed in the very early universe (microseconds after the Big Bang), and can now be reproduced by colliding highly energetic nuclei. The search for the QGP is carried by various collaborations at Cern in Switzerland and Brookhaven National Laboratory (BNL) in the United States. The first evidences of the creation
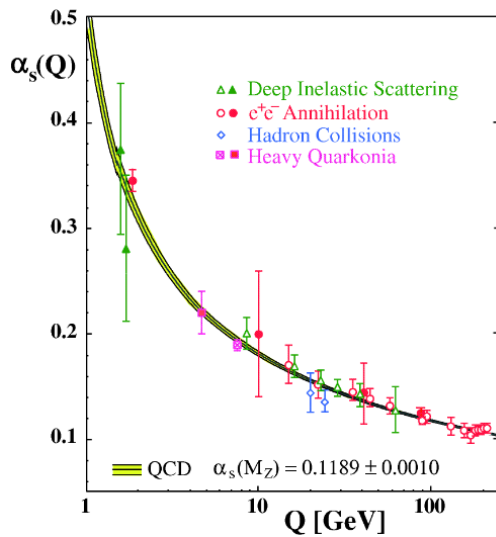
Figure 1.1: Summary of measurements (symbols) of the dependence of the strong coupling constant $\alpha_s(Q)$ on the energy scale Q, compared to QCD predictions (solid lines). Taken from [7].

of this new form of matter came from the Super Proton Synchrotron (SPS) at Cern in the year 2000 (see [9] and references within), when the results of colliding ions proved to be qualitatively different to the simple superposition of many nucleon-nucleon collisions. The signs that indicated that a new phase of matter had been created included: an enhancement in the number of hadrons containing strange quarks relative to proton-proton collisions, and a suppression of charmonium states. Another characteristic feature of heavy ion collisions detected at SPS was that the created matter at the time when all collisions between particles stop, is expanding with velocities greater than half the speed of light. This expansion, indicates an initial explosion of matter due to large pressure gradients, and it is the origin of the name Little Bang, used to designate the explosion after a heavy ion collision.

On the same year as this promising results were announced at Cern, the Relativistic Heavy Ion Collider (RHIC) at BNL–specially built to probe the hot dense matter created after heavy ion collisions–started its operations, and by 2004 further evidence of the creation of QGP was presented by the four RHIC collaborations: BRAHMS (Broad RAnge Hadron Magnetic Spectrometers), PHENIX (Pioneering High Energy Nuclear Interaction eXperiment), Phobos and STAR (Solenoidal Tracker at RHIC) [10–13].

The measurements from RHIC indicated that a very dense matter had been

created: The number of charged particles per unit rapidity in central collisions exceeded by $40\% - 50\%$ the value obtained for the yield in proton-proton collisions rescaled by the number of binary collisions, and the estimated energy density corresponded to at least $15\,\mathrm{GeV/fm^3}$ at its peak, while decreasing to about $5\,\mathrm{GeV/fm^3}$ after a time of $1\,\mathrm{fm/c}$, both well above the critical energy density estimated to be $\epsilon_c \sim 1\,\mathrm{GeV/fm^3}$ by lattice calculations [14].

Another indication of the presence of a very dense medium was the suppression of particles with high transverse momentum, quantified by the nuclear modification factor

$$R_{AA} = \frac{\frac{d^2N^{AA}}{dp_T d\eta}}{\langle N_{\text{coll}} \rangle \frac{d^2N^{nn}}{dp_T d\eta}}, \tag{1.1}$$

that is the ratio between the particle yield in nucleus-nucleus collisions and the yield in proton-proton collisions rescaled by the number of binary collisions between nucleons. This high-p_T suppression was first measured at RHIC, and it results from the interaction of energetic partons with the colored medium.

The two previous paragraphs addressed the question of the creation of a very dense medium, with energy density above the critical value, after a heavy ion collision; however, the question of how this medium behaves still remains. The answer seems to be that it behaves like a fluid: the matter presents a collective behavior, that agrees well with hydrodynamical calculations given that the thermalization time–before the matter reaches equilibrium and can be considered to be a fluid–is small $\tau_{\text{therm}} \sim 1\mathrm{fm/c}$. The maximum flow velocity calculated from RHIC data is between $0.7c$ and $0.75c$, greater than what had been measured at SPS.

At present there are two heavy ion colliders: RHIC and the Large Hadron Collider (LHC) at Cern. The latter one started running in 2010, and has three experiments that study heavy ion collisions: ALICE (A Large Ion Collider Experiment), ATLAS (A Toroidal LHC Apparatus) and CMS (Compact Muon Solenoid). Results from LHC confirm what was found at RHIC, and it is now believed that QGP has been created; however, it is not a plasma of freely moving quarks, but it is composed of strongly interacting particles, and it behaves like an almost perfect fluid, with values of shear viscosity to entropy ratio close $\eta/s = 1/(4\pi)$, that is the minimal value for this transport coefficient, and was calculated [15, 16] using the AdS/CFT correspondence [17].

1.1 Collective Flow

The first signs that evidenced the collective motion of the QGP where the presence of a radial flow, and of elliptic flow for non-central collisions. Both quantities refer to the expansion of the fireball (as the QGP created after the collision is usually called) in the transverse plane, but while radial flow is isotropically distributed in the azimuthal angle, the elliptic flow exists because of anisotropies in the transverse plane, in particular its origin is in the almond-like shape of the overlap region between the colliding nucleons, which is present in all but the most central collisions. The effects of radial flow are seen in the slope of the measured hadron spectra, that will vary for different values of the flow. The presence of elliptic flow is seen in plots of two-particle correlations as a function of the difference in azimuthal angle between them, that present two peaks located at $\Delta\Phi = 0$ and $\Delta\Phi = \pi$, indicating that most of the particles go in the same direction or in exactly opposite directions, as would be the case for an initial ellipse that expands in the direction of its short axis because of the higher pressure gradients. The quantity of interest is the v_2 coefficient that is the second coefficient of the Fourier expansion of the single-particle distribution (see Equation (1.2) below).

Relativistic hydrodynamics has been very successful in describing radial and elliptic flow data (see *e. g.* [18–21]), and in estimating from this last quantity the value of the viscosity of the QGP (see [22] for a review). However, some data from central collisions remained puzzling, because the shape of the two particle correlation differed from the already described two peaked shape attributed to elliptic flow. It has one peak on the near side ($\Delta\Phi = 0$), and two smaller peaks located at $\Delta\Phi \sim 2$ and $\Delta\Phi \sim 4$, that are connected by a flat region on the away side, as shown in Figure (1.2). The explanation to this result came from B. Alver and G. Roland [23], who suggested that the away side structure originated from triangular fluctuations to the initial conditions of the fireball.

The azimuthal distribution of final particles can be written as a Fourier expansion

$$\frac{dN}{d\Phi} \propto 1 + 2\sum_{n=1}^{\infty} v_n \cos n(\Phi - \psi_n^F)\,, \tag{1.2}$$

where v_n is known as the flow coefficient, and ψ_n^F corresponds to the event plane (EP) angle. Each of the terms in the expansion is associated to a particular geometry of the collision, and for non-central collisions the second term is the most important one, because in this case the shape of the overlap region between the nuclei is roughly elliptical. However, in more central collisions
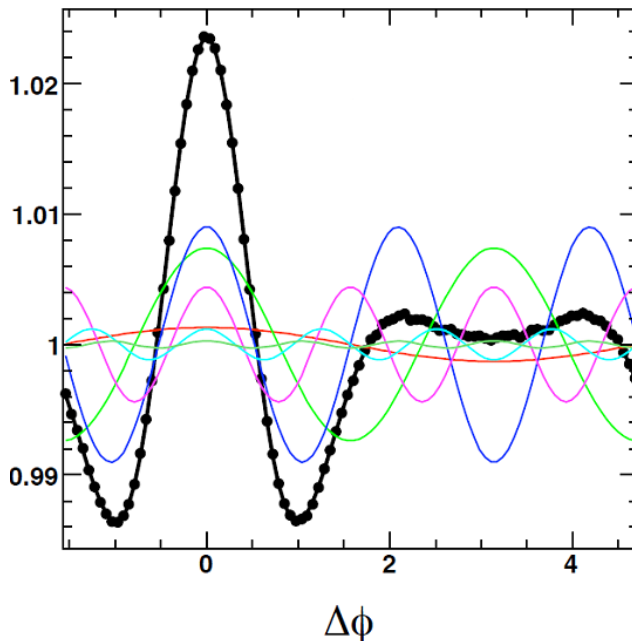
Figure 1.2: Two-particle correlation as a function of the azimuthal difference $\Delta\Phi$ from ATLAS. The black dots correspond to the data and the solid black curve is the sum of the terms of the Fourier expansion up to $n = 6$, that are shown independently in the colored curves. Taken from [24].

the initial shape of the fireball is determined by fluctuations, so contributions from the triangular flow, as well as of higher terms in the expansion become important. In fact, measurements of higher order harmonics have now been presented by five collaborations [25–29].

1.2 Outline of the Thesis

The contents of this thesis correspond to work done in collaboration with my advisor Edward Shuryak in [30–33], and our main goal was to explore perturbations to the expanding background fireball produced in heavy ion collisions, and their effect on the final particle distribution function and correlations.

Chapter 2 explores initial state fluctuations that appear right after heavy ion collisions because of the random positions of the nucleons in the nuclei. We use Glauber Monte Carlo to model these initial fluctuations, and to calculate the coefficients ϵ_n that parameterize the initial anisotropy , together with the associated angles ψ_n.

The rest of the thesis is concerned with the hydrodynamic evolution of the background fireball and of perturbations to it. We use an exact solution to the hydrodynamic equations–the SO(3)-invariant flow–developed by S. Gubser and A. Yarom [34, 35] that is an extension to Bjorken's Flow [36], and that preserves its boost invariance in the beam direction, and its rotational invariance in the transverse plane, but not the translation invariance in the transverse plane, thus allowing the fireball to expand in the radial direction. A review of the SO(3)-invariant flow is presented in Chapter 3, together with solutions to perturbations to this background solution, for ideal and viscous cases. We discuss the effects that the presence of viscosity has on perturbations, and we study the hydrodynamical evolution of certain initial conditions.

In Chapter 4 we study the final particle distribution functions, two particle correlations and flow coefficients obtained at freeze-out time. We study in detail the case where there is one Gaussian perturbation at the initial time, and the effects that viscosity and the width of the perturbation have on the final results.

Finally, in Chapter 5 we continue to study the hydrodynamic evolution of a perturbation on top of the SO(3)-invariant background, but this time the focus is not on perturbations to the initial state, but on perturbations that appear near the critical temperature T_c instead.

Chapter 2

Initial State

In heavy ion collisions the expression initial state may, depending on the context, refer to different stages of the collision such as the setting of the nuclear wave function before the collision, the state right after the collision, and the state after the matter reaches an approximate equilibrium. It is to this latter meaning that we refer to in this thesis: to the initial state that determines the initial conditions for the hydrodynamical evolution of the QGP.

There are many different ways to model the fluctuating initial conditions for hydrodynamics in heavy ion collisions. One of the most popular options is the Glauber Monte Carlo model, that consist in randomly generating the positions of the nucleons in the nuclei according to a distribution of nuclear matter, and then determine which of them collide according to their transverse separation. The local density of matter produced is assumed to be simply proportional to the local density of all participant nucleons, and the energy density is in fact calculated by asigning to each wounded nucleon (the ones that suffered a collision) a Gaussian in the transverse plane. This is the model that we use to simulate initial conditions and it is described in detail in the following Section.

2.1   The Glauber Model

The Glauber Model (for a review see *e. g.* [37]) is used to describe processes in which nucleons scatter on nuclear matter. In the context of heavy ion collisions it can be used to describe the initial conditions in the transverse plane of the matter created in the collision. The model assumes that the interactions between the two colliding nuclei are determined by the interaction among individual nucleons, each of which can experience a number of collisions with the nucleons from the other nucleus as the two nuclei pass through each other. Because the Glauber Model uses nucleon nucleon collisions, one of the
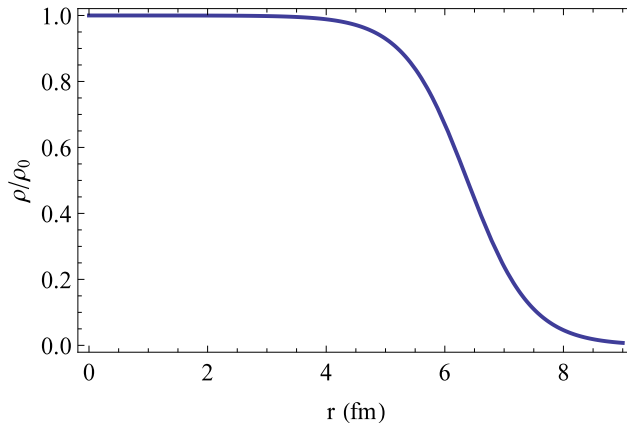
Figure 2.1: Nuclear density distribution with mean radius $R = 6.38$ fm and thickness $a = 0.535$ fm.

inputs that it requires is the nucleon nucleon cross section $\sigma_{\text{inel}}^{NN}$, that depends on the energy of the collision.

The model also needs as an input a nuclear density distribution, that can be well parameterized by the Wood-Saxon distribution

$$\rho_{\text{nuclear}}(r) \propto \frac{\rho_{0\,\text{nuclear}}}{1 + \exp \frac{r-R}{a}} \, , \tag{2.1}$$

for spherical nuclei such as gold and lead, which are used in heavy ion collisions at RHIC and LHC, respectively. In the expression $r = \sqrt{x^2 + y^2 + z^2}$ is the three dimensional radius, R is the mean nuclear radius, a is the skin depth and ρ_0 is chosen such that after spatial integration of the Wood-Saxon profile one obtains the total number of nucleons. An example of this distribution for a gold nucleus is shown in Figure 2.1, with $R = 6.38$ fm and $a = 0.535$ fm [38]. The distribution is flat up to some surface determined by the mean radius R, and then falls rapidly to zero. The witdth of this fall, where the nuclear density changes from being 90% of the maximum to 10% is of about 2.3 fm.

To use the Glauber model it is necessary to work with high energy collisions, because one of the main assumptions that is made is that the colliding nucleons travel in a straight trajectory as the nuclei pass through each other. In this way a nucleon at a given position in the transverse plane will collide with all of the nucleons from the other nucleus that occupy the same transeverse position as it does. This is represented in Figure (2.2) by the darker zones present in both nuclei: any nucleons located in the darker red zone will collide with all of the nucleons in the darker blue zone. The only parameter that determines
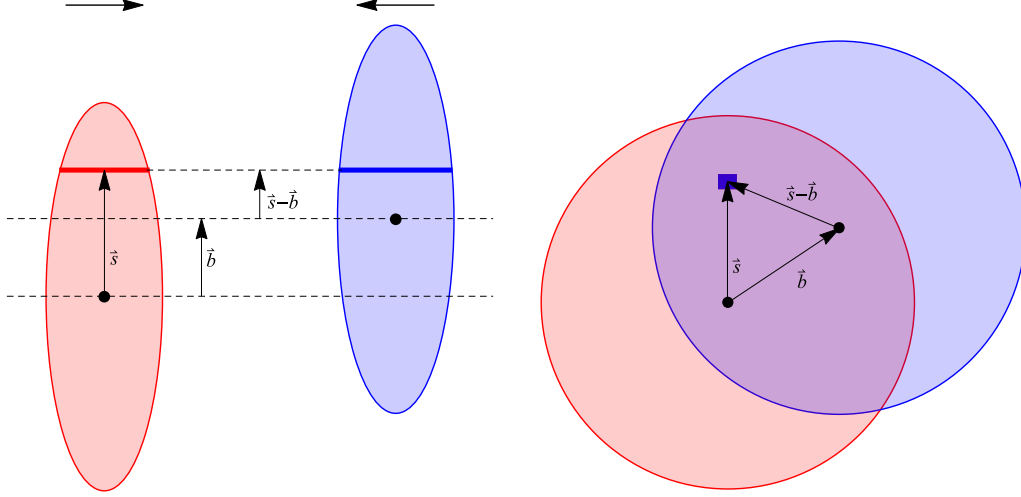
Figure 2.2: Longitudinal (right) and transverse (left) views of the collision between two nuclei in the Glauber Model. The impact parameter between the two nuclei is given by $\boldsymbol{b}$, and $\boldsymbol{s}$ is the distance to a given element in the overlapping region.

wether two nucleons collide is their relative position in the transverse plane, thus the z-coordinate may be integrated out to obtain the probability per area that a nucleon has of being in the darker zone

$$\hat{T}_A(\boldsymbol{s}) = \int \hat{\rho}_A(\boldsymbol{s}, z) dz \,, \tag{2.2}$$

where the nuclear density $\rho(r)$ has been normalized, such that

$$\hat{\rho}(r) = \frac{\rho(r)}{A} \,, \tag{2.3}$$

with A the number of nucleons in the nucleus A, and $\boldsymbol{s}$ is the location of the darker (overlapping) zone. The thickness fucntion

$$\hat{T}_{AB}(\boldsymbol{b}) = \int \hat{T}_A(\boldsymbol{s}) \hat{T}_B(\boldsymbol{s} - \boldsymbol{b}) d^2 s \,, \tag{2.4}$$

is the integral over the transverse plane of the probability that nucleons of the two colliding nuclei (A and B) are in the overlapping zone. The probability of one interaction between nucleons is $\hat{T}_{AB}(\boldsymbol{b}) \sigma_{\text{inel}}^{NN}$, and the probability of having

9

n interactions can be obtaind from the binomial distribution

$$P(n, \boldsymbol{b}) = \left(\begin{array}{c} AB \\ n \end{array} \right) \left(\hat{T}_{AB}(\boldsymbol{b}) \sigma_{\text{inel}}^{NN} \right)^n \left(1 - \hat{T}_{AB}(\boldsymbol{b}) \sigma_{\text{inel}}^{NN} \right)^{AB-n} . \tag{2.5}$$

Summing this probability over n, it is posible to obtain the cross-section of the heavy ion collision

$$\frac{d^2 \sigma_{\text{inel}}^{AB}}{db^2} = \sum_{n=1}^{AB} P(n, \boldsymbol{b}) , \tag{2.6}$$

$$= 1 - \left(1 - \hat{T}_{AB}(b) \sigma_{\text{inel}}^{NN} \right)^{AB} , \tag{2.7}$$

and by suming over it times the number of interactions one gets the number of collisions among nucleons

$$N_{\text{coll}}(b) = \sum_{n=1}^{AB} P(n, \boldsymbol{b}) , \tag{2.8}$$

$$= AB\hat{T}_{AB}(b) \sigma_{\text{inel}}^{NN} . \tag{2.9}$$

One last quantity of interest is the numer of wounded or participant nucleons given by [39]

$$N_{\text{part}}(\boldsymbol{b}) = A \int \hat{T}_A(\boldsymbol{s}) \left(1 - (1 - \hat{T}_B(\boldsymbol{s} - \boldsymbol{b}) \sigma_{\text{inel}}^{NN})^B \right) d^2 s$$

$$+ B \int \hat{T}_B(\boldsymbol{s} - \boldsymbol{b}) \left(1 - (1 - \hat{T}_A(\boldsymbol{s}) \sigma_{\text{inel}}^{NN})^A \right) d^2 s \tag{2.10}$$

that are all of the nucleons that collide when the collision among the two nuclei takes place, and it is related to the centrality of the collision.

2.1.1 Centrality

In the Glauber model there is a connection between the impact parameter b, the number of participants N_{part} and the number of binary collisions N_{coll}, but none of these quantities can be directly related to experimental measurements. A way to connect Glauber results to experiments is by defining centrality classes with both methods, and relating them.

In experiments, the centrality classes are defined using the charged particle multiplicity N_{ch} per event. This quantity can be measured for a large collection of events, yielding a distibution. The total integral of the distribution can be
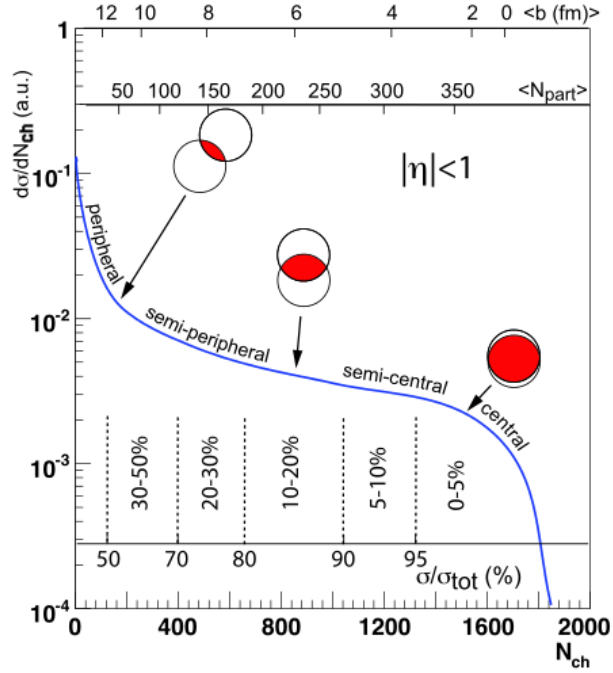
Figure 2.3: Schematic figure showing the relation between the experimental observable N_{ch} and the Glauber computed quantities N_{part} and b. Taken from[37].

calculated, and different centrality classes are defined by binning the data, where each bin corresponds to a centrality class, that is the integral over the bin is a percentage of the total integral, as shown in the schematic plot in Figure (2.3), where the vertical lines separate different bins. In a similar way, centrality classes in the Glauber model can be defined as a fraction of the total cross section [21]

$$c(b) = \frac{2\pi \int_0^b b'db' \left(1 - e^{\sigma_{NN}^{in} T_{AA}(b')}\right)}{2\pi \int_0^\infty b'db' \left(1 - e^{\sigma_{NN}^{in} T_{AA}(b')}\right)} \, , \tag{2.11}$$

where $T_{AA}(b) = AA\hat{T}_{AA}$ is the thickness function defined in Equation (2.4), and the approximation $(1+x/N)^N \sim e^x$ for large N has been used. Notice that $b = 0$ corresponds to a perfectly central collision, that is a centrality of 0%, while a completely peripheral collision would have a centrality of 100%. Table (2.1) shows the values of the ranges of impact parameter as well as the average impact parameter, and the average number of participants corresponding to

11

centrality	b_{min} (fm)	b_{max} (fm)	$\langle b \rangle$ (fm)	$\langle N_{part} \rangle$
0-5%	0.0	3.3	2.20	352.2
5-10%	3.3	4.7	4.04	294.7
10-15%	4.7	5.8	5.27	245.6
15-20%	5.8	6.7	6.26	204.2
20-30%	6.7	8.2	7.48	154.5
30-40%	8.2	9.4	8.81	103.8
40-50%	9.4	10.6	10.01	64.9
50-60%	10.6	11.6	11.11	36.6
60-70%	11.6	12.5	12.06	18.8
70-80%	12.5	13.4	12.96	7.5
80-90%	13.4	14.3	13.85	4.4

Table 2.1: Impact parameter and number of participants for different centrality ranges in Au+Au collisions. [40]

different centrality classes as calculated in [21, 40]. These centrality classes are taken to be the same as the ones calculated from experiments, thus the quantities from the Glauber model can now be related to experiment.

2.1.2 Glauber Monte Carlo

In the Glauber Monte Carlo approach for heavy ion collisions the position of the nucleons in each of the nuclei is randomly selected according to the nuclear density distribution. The distribution we use is the Woods-Saxon distribution from Equation (2.1), that resembles a realistic nuclear density, being mostly flat towards the center of the nucleus and decreasing rapidly near the edge.

Once the transverse positions of the nucleons have been selected, they remain fixed during the collision process, because it is assumed that they move in straight lines and that the nucleon nucleon cross-section of any two nucleons is independent of the previous collisions that the nucleons have encountered.

Collisions between two nucleons take place when they pass sufficiently close to each other, that is when their distance of separation d in the transverse plane satisfies

$$d \leq \sqrt{\frac{\sigma_{NN}^{inel}}{\pi}} \, . \tag{2.12}$$

The inelastic nucleon-nucleon cross-section $\sigma_{NN}^{\text{inel}}$ depends on the energy of the collision, and for RHIC with center of mass energy $\sqrt{s_{NN}} = 200$ GeV, it has
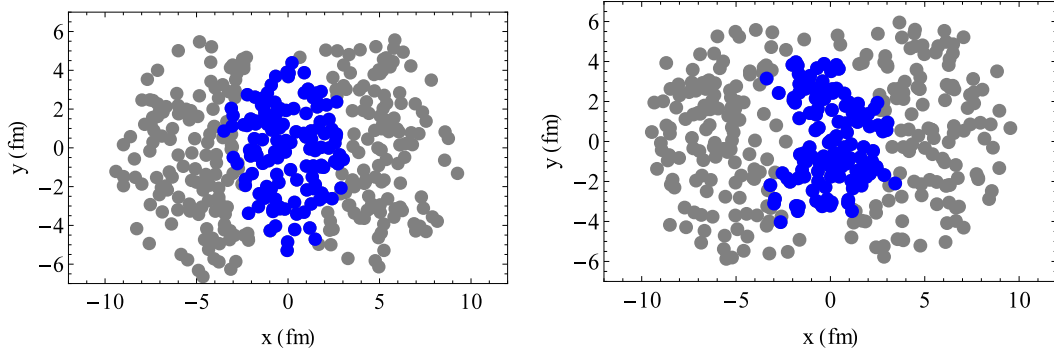
Figure 2.4: Two events generated via Glauber Monte Carlo, with the same number of participant (or wounded) nucleons N_{part}. The participant nucleons are blue and the expectators are gray.

an average value of 42 mb [41]. The internal configurations of the nucleons generate fluctuations to the nucleon nucleon cross-section, as discussed in [42, 43], and can be included in the Glauber Monte Carlo calculations by using a Gaussian distribution with variance

$$w_{NN} = \frac{\langle \sigma_{NN}^2 \rangle - \langle \sigma_{NN} \rangle^2}{\langle \sigma_{NN} \rangle^2} \,, \tag{2.13}$$

that for RHIC energies ranges between 0.2 and 0.3 [43].

Because of the randomness of the position of the nucleons in the nuclei, each simulation of a collision is different from all the others, as exemplified in Figure (2.4), where we present two different collision events for the same number of participants N_{part}, with very different results. While on the left plot the region formed by the wounded nucleons resembles the expected almond-like shape one obtains when considering a smooth nuclear density, on the plot on the right the intersection region shows some deformations. Each event that is calculated is unique–much like in real heavy ion collisions–because of the fluctuations in the relative positions of the nucleons in the nuclei, so any quantities that are analyzed are usually averaged over many events. In experiments this averaging takes place in the final stage, after freeze-out, and the average is taken over the final particle distributions. In theoretical calculations there are two approaches: the event-by-event approach where a number of randomly created initial states are let to evolve independently until freeze-out, and the average is taken over final particle distributions (see *e. g.* [44–46]), and the approach where an average is taken over initial states, and the result is the one that then goes through the hydrodynamic evolution (see [47, 48]).

Whatever the method used, it is clear now that fluctuations in the initial

13

state play a fundamental role in the final particle distribution functions and in the flow coefficients. Not only is there a fluctuating ellipticity [49], but also triangularity, as proposed by B.Alver and G. Roland in [23] and deformations associated to higher angular harmonics. In the next section we study how to quantify the deformation of the interaction zone with the asymmetry parameters ϵ_n.

2.2   Initial Conditions from Glauber Monte Carlo

We begin by simulating a large ensemble of events from which we extract the transverse radial position, and azimuthal location of the participant (or wounded) nucleons. These positions determine the two-dimensional shape of every event, and from them it is possible to compute the anisotropy parameters ϵ_n that quantify the deformation of the overlapping zone in a collision.

The participant anisotropies are calculated from

$$\epsilon_n = \frac{\sqrt{\langle r^n \cos n\phi \rangle^2 + \langle r^n \sin n\phi \rangle^2}}{\langle r^n \rangle} \, , \tag{2.14}$$

where the averages are taken over all the participating nucleons. This expression is calculated in the center of mass of the participant nucleons for each event. Therefore, the dipole moment $n = 1$ made out of the average coordinates

$$\langle x \rangle = \langle r \cos \phi \rangle = 0, \qquad \langle y \rangle = \langle r \sin \phi \rangle = 0 \tag{2.15}$$

is zero by definition.

The participant anisotropy parameters ϵ_n correspond to the coefficients of the Fourier expansion of the azimuthal distribution function

$$f(\phi) = \frac{1}{2\pi} \left(1 + 2 \sum_n \epsilon_n \cos \left(n(\phi - \psi_n) \right) \right) \, , \tag{2.16}$$

where the ψ_n are the angles between the x axis and the major axis of the participant distribution.

In our definition of the ϵ_n (2.14) we have used the standard choice of r^n, where n is the selected term in the Fourier expansion; however, the transverse shape of the event can, in principle, be expanded in a double series in x, y, or in a double series over the moments $r^m \cos n\phi$ and $r^m \sin n\phi$ with integer m, n.

Since the dipole $m = n = 1$ term is zero by construction, we define the first odd deformation ϵ_1, ψ_1 using the term of the expansion $m = 3$, $n = 1$, which appears together with the triangular deformation $m = n = 3$,

$$\epsilon_1 = \frac{\sqrt{\langle r^3 \cos \phi \rangle^2 + \langle r^3 \sin \phi \rangle^2}}{\langle r^3 \rangle} \ . \tag{2.17}$$

The participant anisotropies can be calculated for any event, in particular for the examples presented in Figure (2.4) we find that the plot on the left has $\epsilon_2 = 0.311$ and $\epsilon_3 = 0.170$, and the one on the right has $\epsilon_2 = 0.338$ and $\epsilon_3 = 0.407$, so in this last example the triangular deformation is larger than the elliptical one, even though we are dealing with a semi-peripheral collision. This example is useful to understand, the importance of initial state fluctuations, but instead of looking at individual cases, it is best to study the average behavior of the anisotropy parameters and their fluctuations, and to analyze their behavior for all centralities.

The calculated anisotropies are plotted in Figure (2.2) as a function of centrality for $n = 1..6$. The plot shows that the eccentricity has the largest value for the well known elliptic deformation ϵ_2 and a nonzero value of triangularity ϵ_3, in agreement with the results reported in [23]. Note that, for the near central collisions, $N_{\text{part}} > 300$, the elliptic deformation is no longer dominant, and it is also due to fluctuations. This conclusion becomes evident as one looks at the bottom plot in Figure (2.2), which shows the variations of these ϵ_n. An interesting observation originating from these results is that all other deformations (except for ϵ_1, which is small because the "true dipole" remains zero) are comparable in magnitude, ranging from $\epsilon_n \sim 0.1$ for central collisions to 0.3 to 0.5 for the more peripheral ones. While in the central bins these perturbations can be considered small , this is not true for the most peripheral bins, when the number of participants is smaller.

The obtained results show that there is absolutely no ground to single out ϵ_3 in the initial stage after the collision. In fact, both ϵ_4 and ϵ_5 are larger than ϵ_3, and ϵ_6 is of about the same order as ϵ_3, and they should all be studied equally.

The variance of the participant anisotropies also depends on centrality, being larger for more peripheral collisions and smaller in the central cases, and for all the six values of n it is comparable in magnitude to the average deformation.
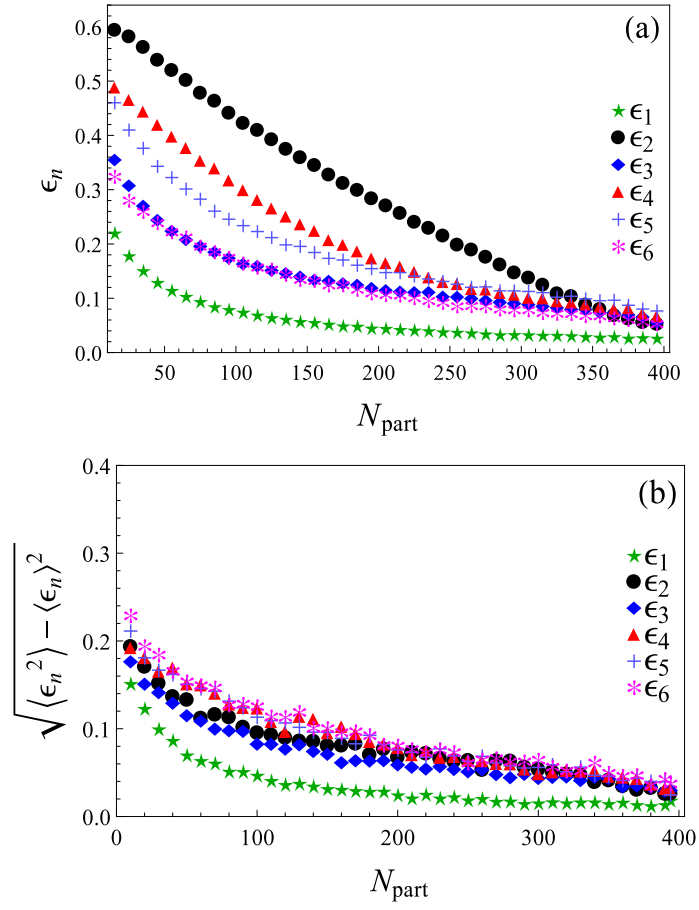
Figure 2.5: Average anisotropies ϵ_n (top) and their variance (bottom) as a function of the number of participants N_{part}, for n=1..6.

16

2.2.1 The angles

The angles ψ_n that define the direction of the major axis of the overlap region can be calculated by

$$\tan n\psi_n = \frac{\langle r^n \sin n\phi \rangle}{\langle r^n \cos n\phi \rangle} \, , \qquad (2.18)$$

except for the first angle associated to $n = 1$, that is given by

$$\tan n\psi_n = \frac{\langle r^3 \sin \phi \rangle}{\langle r^3 \cos \phi \rangle} \, , \qquad (2.19)$$

because the origin of the coordinates is set in the center of mass of the participant nucleons. These angles differ from the angles of the flow, that point in the direction of maximum flow, that is: in the direction of the small axis of the original matter distribution, where the pressure gradients are the largest. The two angles are related by

$$\psi_n^F = \psi_n + \frac{\pi}{n} \, . \qquad (2.20)$$

Using the expressions (2.18), and (2.19) for all of the calculated events with $100 < N_{\text{part}} < 300$, we obtain the distribution of the ψ_n's for the first six harmonics as shown in Figure (2.6). We discuss each of the distributions separately, starting by the ψ_n with n even, that present a more clear interpretation.

The first thing to notice from Figure (2.6) is that all of the even harmonics present peaks at some angular position. The most obvious one is the distribution of the second (elliptic) harmonic. The angle ψ_2 is strongly peaked at $\pi/2$, that corresponds to an elongation of the system in the y direction. This, of course, agrees with the expectations of having and almond-shaped overlap region between the two nuclei. The distribution of the fourth angle ψ_4 presents peaks at angles 0 and $\pi/2$, and because of the quartic symmetry of the fourth harmonic this simply means that the maxima of the distribution tend to be aligned with the coordinate axes x and y. The distribution of the sixth harmonic is different; it is peaked at the angle $\pi/6$. This means that it has no maximum in the x direction, but it has in the y direction. This results show that the even harmonics, especially the second and the fourth, are strongly correlated with the reaction plane, with all of them producing maxima along the y (out-of-plane) direction. The distribution of the sixth harmonic though also correlated to the reaction plane, is non-zero for all angles, so the correlation is not that strong in this case.
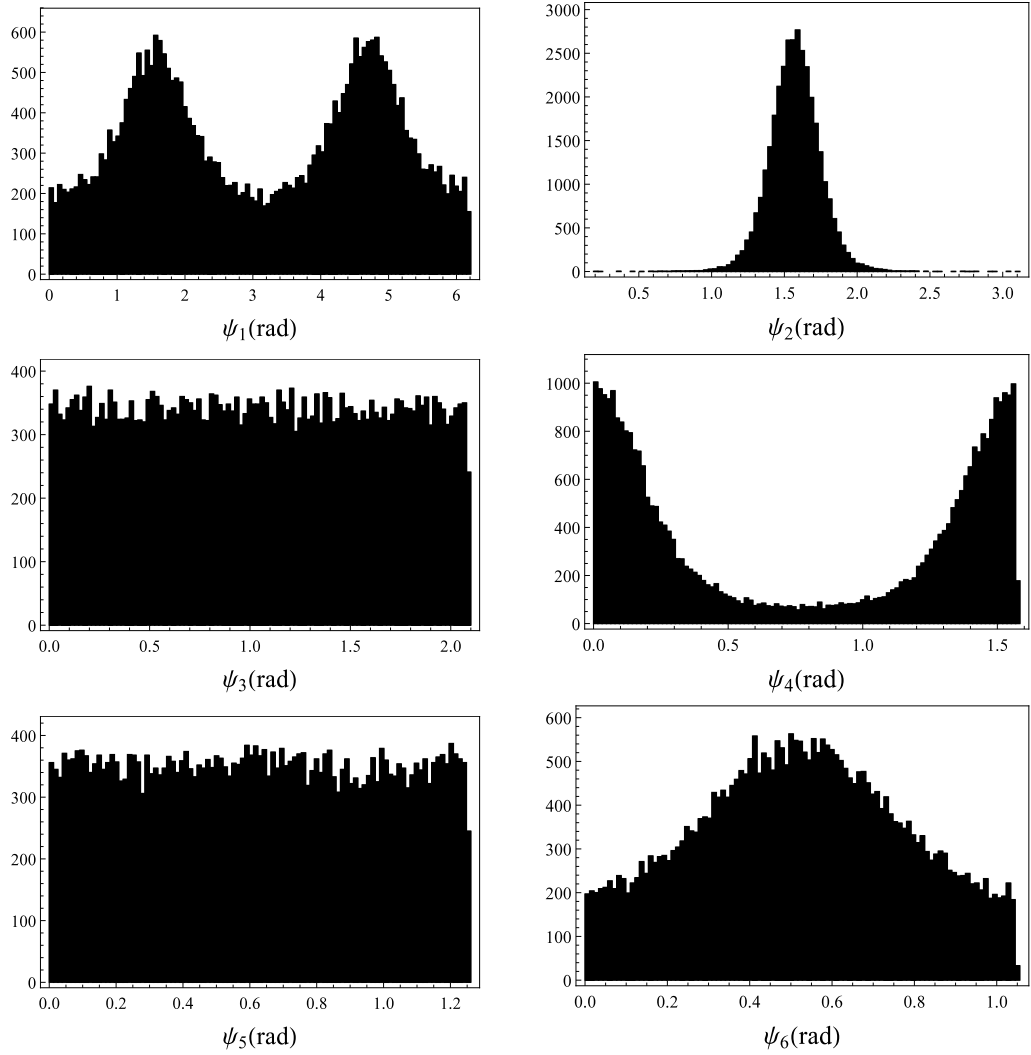
Figure 2.6: Distribution of the angles ψ_n for the first six harmonics, for a centrality bin corresponding to $100 < N_{\mathrm{part}} < 300$.

The clear correlations present for the even harmonics are not evident in the case of the odd ones. The distribution of the angle ψ_1 is nonzero at all angles, this implies that it is not very strongly correlated with the reaction plane. It has two maxima, at $\pi/2$ and at $3\pi/2$, that is: it points in the $\pm y$ direction. These peaks have their origin in what we will call "tip' fluctuations, because they are at the tips of the almond. Although the contributions from angles 0, π (in the x direction) are about twice smaller than the peaks, they also make an important contribution. We will call them "waist" fluctuations. Note that, while the area of the "waist" is larger than that of the "tips", its contribution is smaller.

The distributions for ψ_3, ψ_5 in Figure (2.6) are flat, so they are completely uncorrelated with the reaction plane (also noted in Reference [23]). However, further scrutiny shows that they are in fact well correlated with ψ_1, as shown in Figure (2.7), where we have included points repeated by periodicity. The distribution can be crudely characterized by some "bumps" plus some "stripes" connecting them.

The bumps occur when one of the vertices of the triangular shape (defined by ψ_3) coincides with the direction of ψ_1, when it is pointing in the $\pm y$ direction, and we interpret them as corresponding to events with additional hot-spots at the tips of the almond. It is a very natural place for maximal fluctuations to be, for two reasons: because this is where the participant density in both nuclei is near zero, and because of the factor r^3 they have larger weight than all other places that are closer to the center.

The stripes can be separated in two kinds: those with positive slopes and those with negative slopes. The latter ones simply follow from the ψ_1 distribution, and they correspond to $\psi_1 = \pi/2, 3\pi/2, 5\pi/2, 7\pi/2$, etc, when the dipole deformation is in the $\pm y$ direction. The stripes with positive slopes are indeed nontrivial correlations between the angles given by

$$\psi_3 = \frac{1}{3}(\psi_1 + \pi)\,, \tag{2.21}$$

$$\psi_3 = \frac{1}{3}(\psi_1 + 3\pi)\,. \tag{2.22}$$

Another way to see this correlation is by looking at the histogram of $\cos(\psi_1 - 3\psi_3)$ for all of the events in the centrality range of interest, as the one presented in Figure (2.8). It consists of two clearly different parts: a very narrow peak near -1 and a wide flat distribution between -1 and 1. This plot demonstrates the qualitative feature of the phase distribution which was pointed out earlier. The peak near -1, that happens when the combination of angles equals π, originates from two of the features discussed above: from fluctuations at
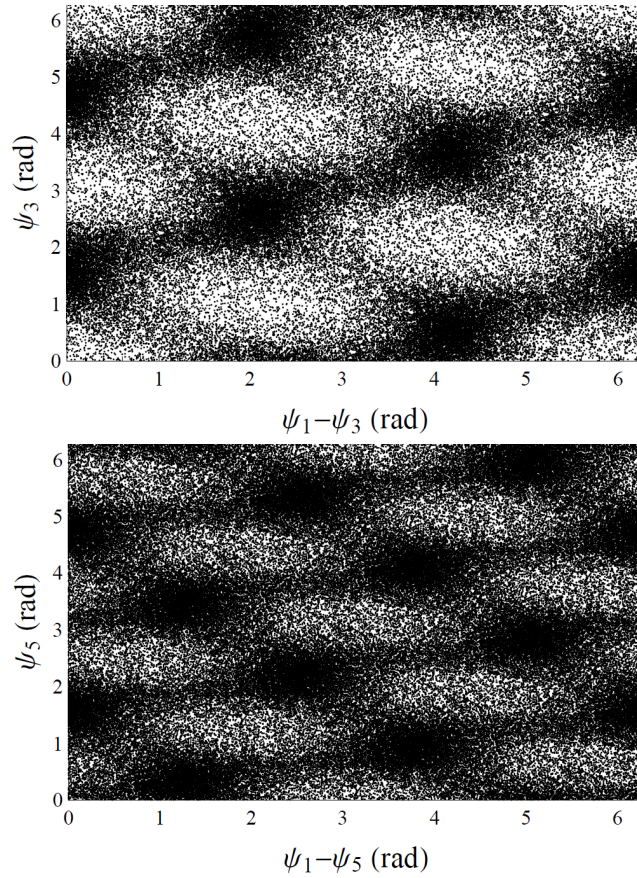
Figure 2.7: Scatter plot of the ψ_3 vs $\psi_3 - \psi_1$ and of the ψ_5 vs $\psi_5 - \psi_1$, for $100 < N_{\text{part}} < 300$.
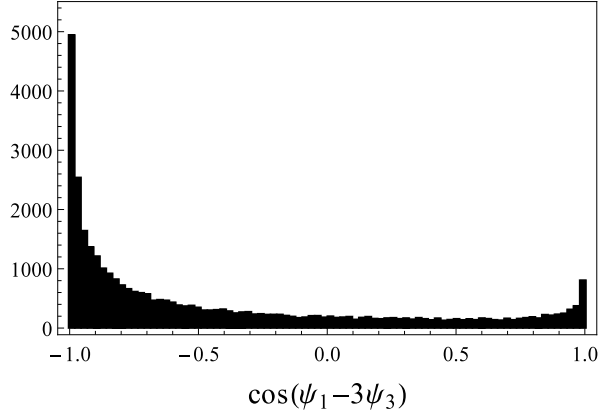
Figure 2.8: Histogram of $\cos\left(\psi_1 - 3\psi_3\right)$, for $100 < N_{\mathrm{part}} < 300$.

the tips of the almond, when both ψ_1 and ψ_3 are strongly correlated close to $\pi/2$, and from the "positive slope lines" in Figure (2.7) because, for them the combination $\psi_1 - 3\psi_3$ equals π, or an odd multiple of π.

A similar situation happens for other odd harmonics. For example, the correlation of ψ_5 with ψ_1 is analogous to the one just discussed. The stripes with negative slopes are the same as in the former case, simply a result of the ψ_1 distribution, and correspond to the angle ψ_1 pointing in the vertical direction. The bumps again indicate that one of the major axes of the the $n = 5$ distribution is aligned with the ψ_1 angle, with both pointing in the $\pm y$ direction, or the tips. The stripes with positive slopes correspond to the relations

$$\psi_5 = \frac{1}{5}\left(\psi_1 + 2\pi\right), \tag{2.23}$$

$$\psi_5 = \frac{1}{5}\left(\psi_1 + 4\pi\right), \tag{2.24}$$

and so on.

2.3 Harmonics and their Relative Phases Extracted from Correlations

2.3.1 Central collisions: two- versus many-particle correlators

In an ideal central collision, where the impact parameter is negligible, the overall system is completely symmetric in the azimuthal angle. However, any particular event has fluctuations that break this symmetry, and that give rise to different harmonics of the flow, that correspond to the coefficients of the Fourier expansion of the single-particle distribution as see in Equation (1.2). The same expression can be also written using the complex exponent

$$\frac{dN}{d\Phi} = \sum_n v_n e^{in(\Phi - \psi_n^F)} , \tag{2.25}$$

where the sum covers all integer values of n, positive and negative, with $v_0 = 1$, $v_{-n} = v_n$, and $\psi_{-n}^F = \psi_n^F$.

If the elementary perturbation is local (like *e. g.* a delta function in the transverse plane), then its angular position in the transverse plane is the only meaningful azimuthal orientation. The perturbations have random positions in the transverse plane, which we express as

$$\psi_n^F = \psi_p + \tilde{\psi}_n^F , \tag{2.26}$$

where the tilde indicates the angle relative to the perturbation, and ψ_p is the random phase due to the location of the perturbation. Because ψ_p is a random variable, all observables must be averaged over it.

To calculate the two-particle correlation, one must square the single body distribution (2.25) to get

$$\sum_{n_1, n_2} v_{n_1} v_{n_2} \exp\left[in_1\Phi_1 + in_2\Phi_2 - in_1\tilde{\psi}_{n_1}^F - in_2\tilde{\psi}_{n_2}^F - i(n_1 + n_2)\psi_p\right] , \tag{2.27}$$

and average over the ψ_p phase. As a result, in the double sum above only the terms that satisfy

$$n_1 + n_2 = 0 , \tag{2.28}$$

survive. The double sum collapses into a single sum with squared pre-exponent v_n^2, that is a function only of the difference between angles $\Delta\Phi = \Phi_1 - \Phi_2$, and

22

all the phases $\tilde{\psi}_n^F$ disappear.

The situation is different in the many-body (three or more) correlation functions. Indeed, if the single-particle distribution (2.25) is cubed (as needed to compute the three-particle correlation) , one finds a triple sum in which the random phase appears as $\exp[i(n_1 + n_2 + n_3)\psi_p]$, that leads to the "triangular" condition

$$n_1 + n_2 + n_3 = 0 \, . \tag{2.29}$$

Eliminating one of them (*e. g.* n_3), one finds the double sum

$$\sum_{n_1,n_2} v_{n_1} v_{n_2} v_{n_1+n_2} \exp\Big[in_1(\Phi_1 - \Phi_3) + in_2(\Phi_2 - \Phi_3) - in_1(\tilde{\psi}_{n_1}^F - \tilde{\psi}_{n_1+n_2}^F)$$
$$- in_2(\tilde{\psi}_{n_2}^F - \tilde{\psi}_{n_1+n_2}^F) \Big] \, , \tag{2.30}$$

in which the relative phases of different harmonics are still present. Therefore, it is possible to measure the relative phase of the harmonics experimentally, focusing on the corresponding combinations

$$\big\langle v_{n_1} v_{n_2} v_{n_3} \cos\big(n_1\psi_{n_1}^F + n_2\psi_{n_2}^F + n_3\psi_{n_3}^F\big) \big\rangle \, , \tag{2.31}$$

where the three integers must satisfy the condition (2.29).

To relate these results from final particle correlations to the initial conditions it is useful to consider (linearized) hydrodynamics, then one can approximate the flow harmonics by the product of the initial deformations and the linear response terms

$$\big\langle v_{n_1} v_{n_2} v_{n_3} \cos\big(n_1\psi_{n_1}^F + n_2\psi_{n_2}^F + n_3\psi_{n_3}^F\big) \big\rangle = \left(\frac{v_{n_1}}{\epsilon_{n_1}}\right) \left(\frac{v_{n_2}}{\epsilon_{n_2}}\right) \left(\frac{v_{n_3}}{\epsilon_{n_3}}\right)$$
$$\times \big\langle \epsilon_{n_1} \epsilon_{n_2} \epsilon_{n_3} \cos\big(n_1\psi_{n_1}^F + n_2\psi_{n_2}^F + n_3\psi_{n_3}^F\big) \big\rangle \, . \tag{2.32}$$

Then, it is necessary to change the flow angles ψ_n^F to the deformation angles ψ_n. In each of the three terms the n_i that multiplies the flow angle is canceled by the n_i in the denominator, from Equation (2.20), leaving only 3π, which is just a total sign change

$$\cos\big(n_1\psi_{n_1}^F + n_2\psi_{n_2}^F + n_3\psi_{n_3}^F\big) = - \cos\big(n_1\psi_{n_1} + n_2\psi_{n_2} + n_3\psi_{n_3}\big) \, . \tag{2.33}$$

23

2.3.2 Mid-central collisions and the two-particle correlators relative to the event plane

A non-zero impact parameter violates axial symmetry and creates an elliptic flow, no longer caused by fluctuations, but by the deformed shape of the overlap region between the nuclei. For mid-central collisions the average value of the second anisotropy coefficient is large itself, and it is also large compared to its fluctuations. For example, ϵ_2 is about 0.5 (0.3) for 100 (200) participants, with $\delta\epsilon_2 \sim 0.1$. Furthermore, as seen in Figure (2.6), its angle ψ_2 is very much directed at $\pm\pi/2$, which means that the flow angle is peaked "in-plane": $\psi_2^F = 0$, π, as indeed is observed.

If one of the harmonics in the correlation (2.34) is the second on (*e. g.* $n_3 = 2$), the product can be approximated by

$$
\left\langle v_{n_1} v_{n_2} v_{n_3} \cos\left(n_1\psi_{n_1}^F + n_2\psi_{n_2}^F + n_3\psi_{n_3}^F\right)\right\rangle = \left(\frac{v_{n_1}}{\epsilon_{n_1}}\right)\left(\frac{v_{n_2}}{\epsilon_{n_2}}\right)\left(\frac{v_{n_3}}{\epsilon_{n_3}}\right)\langle\epsilon_2\rangle
$$
$$
\times \left\langle \epsilon_{n_1}\epsilon_{n_2}\cos\left(n_1\psi_{n_1}^F + n_3\psi_{n_2}^F\right)\right\rangle ,
$$
$$(2.34)$$

where the large and non-fluctuating ϵ_2 was factored out from the other two harmonics, which are small and fluctuating, and by putting $\psi_2^F = 0$ we have selected the the frame in which the reaction plane is the x axis.

From the Glauber computations, it is possible to determine the particular combinations of amplitudes and phases of two harmonics

$$
\langle \epsilon_{n_1}\epsilon_{n_2}\cos\left(n_1\psi_{n_1} - n_2\psi_{n_2}\right)\rangle ,
$$
$$(2.35)$$

especially in the case when n_1, and n_2 differ by two units, when the triangular condition is satisfied. We have studied two examples of the kind, with odd harmonics 1, 3 and 5, and the results for different centralities are presented in Figure (2.9). Both combinations are negative, and increase in absolute value towards more peripheral collisions, while going to zero for central ones. This is expected to occur, because for central collisions the azimuthal symmetry of the the overlap region is recovered, and all of the eccentricities, including ϵ_2 become small.
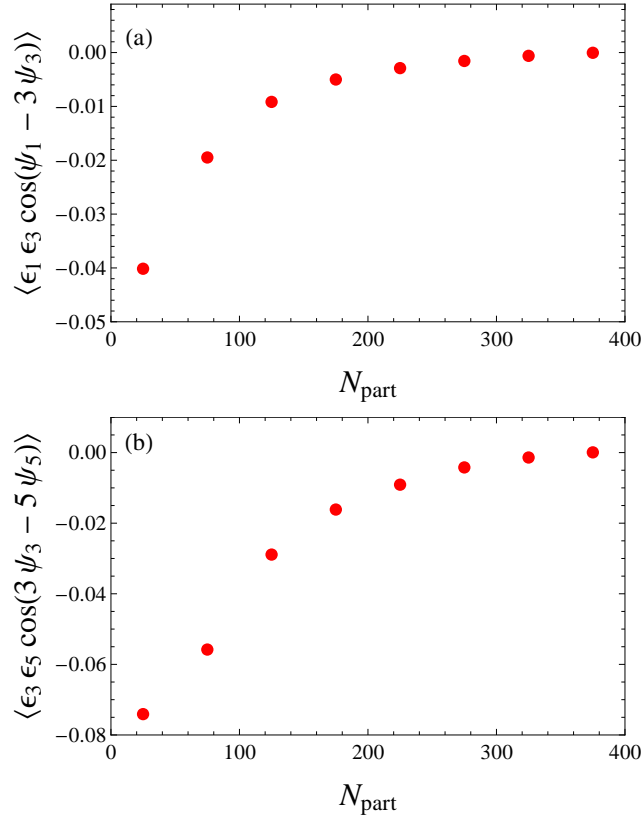
Figure 2.9: Correlators $\langle \epsilon_1 \epsilon_3 \cos(\psi_1 - 3\psi_3) \rangle$ (top) and $\langle \epsilon_3 \epsilon_5 \cos(3\psi_3 - 5\psi_5) \rangle$ (bottom) as a function of centrality.

Chapter 3

Hydrodynamic Evolution

3.1 Hydrodynamics in Heavy Ion Collisions

Hydrodynamics is a macroscopic theory that can be used to describe the collective motion of particles when the average distance traveled by them before colliding with another particle is much smaller than the size of the system. When this condition is satisfied, the matter under study can be considered to be continuous, and thus the quantities that describe it–such as the pressure, the temperature, the energy density and the velocity–can be defined at each point in spacetime.

The local conservation of energy, momentum and baryon number is described by the hydrodynamic equations

$$\nabla_\mu T^{\mu\nu} = 0 \,, \tag{3.1}$$

$$\nabla_\mu J_B^\mu = 0 \,, \tag{3.2}$$

where $T^{\mu\nu}$ is the stress-energy tensor, and J_B^μ is the baryon current. In all of our calculations we disregard the baryon conservation Equation (3.2), because in the region of the phase diagram that is explored in heavy ion collisions, the baryon content is very small, so we take it to be zero. The ∇_μ represents the covariant derivative

$$\nabla_\mu T^{\mu\nu} = \partial_\mu T^{\mu\nu} + \Gamma^\mu_{\mu\lambda} T^{\lambda\nu} + \Gamma^\nu_{\mu\lambda} T^{\mu\lambda} \,, \tag{3.3}$$

with the Christoffel symbols corresponding to

$$\Gamma^\sigma_{\mu\nu} = \frac{1}{2} g^{\sigma\rho} (\partial_\mu g_{\nu\rho} + \partial_\nu g_{\rho\mu} - \partial_\rho g_{\mu\nu}) \,, \tag{3.4}$$

which, of course, become zero when the Minkowski metric $g_{\mu\nu} = \eta_{\mu\nu}$ is used,

but are important in curved space or when curved coordinates are used, as it will be seen below.

The stress-energy tensor for a perfect fluid (no viscosity and no heat conduction) can be written in terms of the energy density, the pressure and the fluid four-velocity, and to determine its precise form, one can go to the frame where the fluid is at rest, where only the diagonal elements of the tensor survive with the T^{00} component being the energy density, and all the T^{ii} components corresponding to the pressure. Writing this in a frame-invariant way, one gets

$$T_{\mu\nu} = (\epsilon + p)u_\mu u_\nu + pg_{\mu\nu}\,, \tag{3.5}$$

that is the stress-energy tensor for a perfect fluid valid in any frame.

There is one more element missing to have the problem of ideal hydrodynamics completely formulated, and that is the equation of state (EoS), that holds information about the nature of the fluid under study. In particular, in heavy ion collisions we use an equation of state that establishes the relation between the energy density and the pressure. In this thesis, we take this relation to be

$$\epsilon = 3p\,, \tag{3.6}$$

that corresponds to the equation of state of conformal matter, and that is usually used to describe the QGP. This choice of equation of state makes the stress-energy tensor traceless, which implies that is is invariant under conformal transformations, a property necessary for the development of the SO(3)-invariant flow that we use in our calculations, and that we describe in detail later in this chapter.

Results from heavy ion collisions, seem to indicate that the QGP is an almost perfect fluid, with a very small viscosity (for a review on viscosity in the QGP see [22]). To include this viscosity in the ideal description of a fluid that we have just given, it is necessary to add all gradients of the velocity to the stress-energy tensor. In the limit in which these gradients are small, the expansion is done up to first order in derivatives of the flow, and in this case one has

$$T_{\mu\nu} = (\epsilon + p)u_\mu u_\nu + pg_{\mu\nu} - \eta\sigma_{\mu\nu} - \zeta(\nabla_\lambda u^\lambda)P_{\mu\nu}\,, \tag{3.7}$$

where

$$\sigma_{\mu\nu} = P_\mu^\alpha P_\nu^\beta \left(\nabla_\alpha u_\beta + \nabla_\beta u_\alpha - \frac{2}{3}g_{\alpha\beta}\nabla_\lambda u^\lambda\right)\,, \tag{3.8}$$

27

is a symmetric, and traceless tensor, and

$$P_{\mu\nu} = u_\mu u_\nu + g_{\mu\nu} \,, \tag{3.9}$$

is the projection tensor. The coefficients of the third and fourth term in Equation (3.7) correspond to the shear viscosity η, and the bulk viscosity ζ. We will only study the effects of the shear viscosity on the flow, and will neglect the bulk viscosity, which multiplies a tensor with non-vanishing trace, and thus cannot be included when the matter is required to be conformal.

3.1.1 Sound

It is possible to add small perturbations to the zeroth order hydrodynamical description just detailed. This is done by modifying the stress-energy tensor

$$T^{\mu\nu} = T_0^{\mu\nu} + \delta T^{\mu\nu} \,, \tag{3.10}$$

which simply consists in adding perturbations to both the energy density, and the flow four-velocity. When these perturbations are small, the problem can be treated in the linear approximation, an the solution to the hydrodynamic equations (3.1) for the perturbations corresponds to a propagating mode: the sound, that moves with speed

$$c_s^2 = \frac{\partial p}{\partial \epsilon} \,. \tag{3.11}$$

For the equation of state that we use (3.6) the speed of sound is $c_s = 1/\sqrt{3}$. The sound waves traveling through the medium perturb it, generating compression and rarefaction of the medium, and thus zones with greater energy density than others. It is the effects of this propagating sound modes in the QGP, that we study in this Chapter, for a particular solution to the hydrodynamic equations (3.1).

3.2 Bjorken's Flow

To apply hydrodynamics to heavy ion collisions it is necessary to determine the symmetries and the initial conditions that the fluid must respect. Depending on how these characteristics are fixed, the solution to the fluid equations, and thus the behavior of the fluid itself will change. One possible solution that describes the evolution of matter produced in the region of midrapidity was developed by J.D. Bjorken [36], and is commonly referred to as Bjorken's flow.

Bjorken's solution only takes into account the expansion of the fluid in the longitudinal direction, while neglecting the radial expansion, it is thus a useful description of the region near the beam axis , where the expansion of the fluid is mostly longitudinal. The symmetries that it preserves are: translation and rotation invariance in the transverse plane, and longitudinal boost invariance. The latter means that at the middle–the location where the collision took place–the matter remains at rest while it moves with speed z/t at a distance z from the center, where t is the time since the collision and z the position in the direction of beam axis. Because of these symmetries it is more convenient to study Bjorken's solutions in hyperbolic-cylindrical coordinates (τ, r, ϕ, η), that are related to the usual cartesian coordinates by

$$t = \tau \cosh \eta, \quad x = r \cos \phi, \tag{3.12}$$
$$z = \tau \sinh \eta, \quad y = r \sin \phi, \tag{3.13}$$

or

$$\tau = \sqrt{t^2 - z^2}, \tag{3.14}$$
$$\eta = \frac{1}{2} \ln \frac{t+z}{t-z}, \tag{3.15}$$

where τ is the proper time and η the rapidity. The metric in the new coordinates is given by

$$g_{\mu\nu} = \begin{pmatrix} -1 & 0 & 0 & 0 \\ 0 & 1 & 0 & 0 \\ 0 & 0 & r^2 & 0 \\ 0 & 0 & 0 & \tau^2 \end{pmatrix}, \tag{3.16}$$

and the four-velocity of the fluid is simply

$$u^\mu = (1, 0, 0, 0). \tag{3.17}$$

Placing these terms in Equation (3.7), one obtains the stress energy tensor

$$T_{\mu\nu} = \begin{pmatrix} \epsilon(\tau) & 0 & 0 & 0 \\ 0 & p(\tau) & 0 & 0 \\ 0 & 0 & p(\tau) & 0 \\ 0 & 0 & 0 & p(\tau) \end{pmatrix}, \tag{3.18}$$

in the case with no viscosity. Both the energy density and the pressure depend only on the proper time, thus preserving all the required symmetries: boost

29

invariance along the beamline, and translation and rotation invariance in the transverse plane. To solve the hydrodynamic equations it is necessary to use the Christoffel symbols defined in Equation(3.4) that correspond to

$$\Gamma^\eta_{\tau\eta} = \Gamma^\eta_{\eta\tau} = \frac{1}{\tau}, \qquad \Gamma^\tau_{\eta\eta} = \tau\,, \tag{3.19}$$

$$\Gamma^\phi_{r\phi} = \Gamma^\phi_{\phi r} = \frac{1}{r}, \qquad \Gamma^r_{\phi\phi} = -r\,, \tag{3.20}$$

and to determine the relation between the energy density and the pressure. Using the conformal equation of state $\epsilon = 3p$, the energy density solution is

$$\epsilon(\tau) = \frac{\epsilon_0}{\tau^{4/3}} \tag{3.21}$$

In a heavy ion collision, the nuclei ar finite, and so is the matter produced after the collision, so the Bjorken description with its translation and rotation invariance in the transverse plane is only an approximation of reality near the beam axis in central collisions.

3.3   Gubser's SO(3)-Invariant Flow

Gubser's flow [34, 35] is a solution to the relativistic Navier-Stokes equations that generalizes Bjorken's flow by replacing the translational invariance in the transverse plane by a symmetry under a special conformal transformation, while keeping the boost invariance and the axial symmetry in the transverse plane. In this way, the matter together with expanding longitudinally also expands in the transverse plane giving rise to radial flow. In this section we discuss Gubser's solution as it was formulated in [34], and then rederived in [35].

What Gubser does is to modify Bjorken's solution by changing the simmetries that must be conserved in the medium. In particular, he changes the translation invariance in the transverse plane by the following special conformal transformation

$$\xi_i = \frac{\partial}{\partial x^i} + q^2 \left(2x_i x^\mu \frac{\partial}{\partial x^\mu} - x^\mu x_\mu \frac{\partial}{\partial x^i} \right)\,, \tag{3.22}$$

where $x^i = x_i = x, y$ and q is a quantity with dimensions of inverse length that determines the transverse size of the matter. If one takes the limit of $q \to 0$, the transverse size of the fireball goes to infinity, and one recovers Bjorken's flow. The transformations (3.22) together with rotations in the transverse

30

plane form an SO(3) group, that gives the name to the new solution: SO(3)-invariant flow.

For Gubser's solution to hold the matter needs to be conformal, this means the stress-energy tensor must be traceless. This requirement is accomplished by using

$$\epsilon = 3p \sim T^4 \tag{3.23}$$

as an equation of state, which implies a speed of sound $c_s = 1/\sqrt{3}$ in the medium, and by setting the bulk viscosity ζ to zero. Another thing to bear in mind is that the existence of azimuthal rotation invariance in Gubser's solution implies that it is only a representative of central collisions, and not applicable to peripheral collisions that do not preserve rotation symmetry.

Working in the $(\tau,\ r,\ \phi,\ \eta)$ coordinates with the metric

$$ds^2 = -d\tau^2 + \tau^2 d\eta^2 + dr^2 + r^2 d\phi^2 \,, \tag{3.24}$$

the only form of the four-velocity that respects rotation invariance, boost-invariance and invariance under longitudinal reflections $(\eta \to -\eta)$ is

$$u_\mu = (-\cosh\kappa(\tau,\ r),\ \sinh\kappa(\tau,\ r),\ 0,\ 0) \,. \tag{3.25}$$

The transverse velocity of the medium then corresponds to

$$v_\perp = \tanh\kappa(\tau,\ r) \,, \tag{3.26}$$

where the function $\kappa(\tau,\ r)$ is

$$\kappa(\tau,\ r) = \operatorname{arctanh}\left(\frac{2q^2\tau r}{1 + q^2\tau^2 + q^2 r^2}\right) \,. \tag{3.27}$$

To get the expression for the energy density it is necessary to plug in the velocity and the equation of state in the equations for relativistic hydrodynamics

$$\nabla^\mu T_{\mu\nu} = 0 \tag{3.28}$$

and in the ideal case, when not only the bulk viscosity but also the shear viscosity vanishes, it takes the form

$$\epsilon = \frac{\hat{\epsilon}_0 (2q)^{8/3}}{\tau^{4/3} \left[1 + 2q^2(\tau^2 + r^2) + q^4(\tau^2 - r^2)^2\right]^{4/3}} \,, \tag{3.29}$$

where $\hat{\epsilon}_0$ is some normalization parameter.

Gubser's solution is invariant under an SO(3) group, however this invariance is not evident in the form of the velocity and the energy density presented in Equation (3.25) and Equation (3.29), respectively. In Reference [35] Gubser and Yarom rederived the same solution, but doing a Weyl rescaling of the metric and changing to a new set of coordinates, where the SO(3)-invariance is clearly visible. The rescaling of the metric is accomplished by dividing it by τ^2,

$$d\hat{s}^2 = \frac{ds^2}{\tau^2} \, , \tag{3.30}$$

$$= \frac{-d\tau^2 + dr^2 + r^2 d\phi^2}{\tau^2} + d\eta^2 \, . \tag{3.31}$$

The new, rescaled metric has a hat (ˆ), as do all the quantities in the rescaled frame, to distinguish them from the same quantities in the usual flat space.

With the change of coordinates both the ϕ and the η coordinates are left untouched, while τ and r are replaced by the new set ρ and θ, that relate to the original coordinates by

$$\sinh \rho = -\frac{1 - q^2\tau^2 + q^2 r^2}{2q\tau} \, , \tag{3.32}$$

$$\tan \theta = \frac{2qr}{1 + q^2\tau^2 - q^2 r^2} \, . \tag{3.33}$$

In these new coordinates the rescaled metric takes the form

$$d\hat{s}^2 = -d\rho^2 + \cosh \rho \left(d\theta^2 + \sin^2\theta d\phi^2 \right) + d\eta^2 \, , \tag{3.34}$$

where the ρ-coordinate takes the place of the new time coordinate, and the θ-coordinate is the new radial coordinate. Gubser's solution is invariant under the SO(3)group of rotations parametrized by θ and ϕ. It is necessary to keep in mind that the θ-coordinate does not correspond to the typical polar angle that is measured from the beamline, so these rotations are not in the usual polar and azimuthal angles, but in θ as defined in Equation (3.33) and the azimuthal angle.

The four velocity of the fluid must, as before, preserve boost invariance and rotation invariance, the last of which is included in the SO(3)-invariance that the flow must conserve. In the new coordinates (ρ, θ, ϕ, η) a four-velocity that satisfies these requirements is given by

$$\hat{u}_\mu = (-1, \, 0, \, 0, \, 0) \, . \tag{3.35}$$

The velocity has no dependence on any of the coordinates, thus the fluid is at rest in the rescaled geometry.

The rescaled energy density in the new coordinates takes the simple form

$$\hat{\epsilon} = \frac{\hat{\epsilon}_0}{(\cosh \rho)^{8/3}} \, , \tag{3.36}$$

which again is invariant under all the required symmetries, because it depends only on the temporal ρ-coordinate. The same is true of the rescaled temperature, which is related to the energy density by

$$\hat{T} = \hat{\epsilon}^{1/4} \, . \tag{3.37}$$

In the viscous case, the equations become more complicated when one works with the energy density, and it becomes more natural to change to the temperature. Again in this case the solution only depends on the new time ρ, and it is given by

$$\hat{T}(\rho) = \frac{\hat{T}_0}{(\cosh \rho)^{2/3}} \left(1 + \frac{H_0}{9\hat{T}_0} \sinh^3 \rho \, _2F_1 \left(\frac{3}{2}, \frac{7}{6}, \frac{5}{2}, -\sinh^2 \rho \right) \right) \, , \tag{3.38}$$

where H_0 is a dimensionless constant that relates the shear viscosity to the energy density according to $\eta = H_0 T^3$, and $_2F_1$ is the hypergeometric function. In the inviscid case the second term vanishes, so the solution is just the first term of the expression.

3.3.1 Taking the results back to flat space

To understand how Gubser's solution relates to heavy ion collisions it is necessary to go back to the usual coordinates (τ, r, ϕ, η) and to rescale the quantities that describe the fluid.

Different quantities X rescale differently according to a given conformal weight α_x as in the relation

$$X = \Omega^{-\alpha_x} \hat{X} \, . \tag{3.39}$$

For example, in Gubser's case the metric was rescaled by

$$ds^2 = \tau^2 d\hat{s}^2 \, , \tag{3.40}$$

so $g_{\mu\nu}$ ($g^{\mu\nu}$) has a conformal weight -2 (2). The conformal weights for relevant quantities in d-dimensional spacetime are presented in the Table (3.1).

quantity	$g_{\mu\nu}$	u_μ	$T_{\mu\nu}$	ϵ	p	T
conformal weight	-2	-1	d-2	d	d	1

Table 3.1: Conformal weights for the metric, the four-velocity, the stress energy tensor, the energy density, the pressure and the temperature on d-dimensional spacetime.

We are particularly interested in the four velocity, and the energy density. The four velocity in Minkowski space and in the (τ, r, ϕ, η) coordinates can be obtained from the one in the rescaled metric and in $(\rho, \theta, \phi, \eta)$ coordinates from the relation

$$u_\mu = \tau \frac{\partial \hat{x}^\nu}{\partial \hat{x}^\mu} \hat{u}_\nu \,, \tag{3.41}$$

that gives us back expression in Equation (3.25). The energy density transformation is simply

$$\epsilon = \frac{1}{\tau^4} \hat{\epsilon} \,. \tag{3.42}$$

3.3.2 Gubser's Flow and Heavy Ion Collisions

The SO(3)-invariant flow is an idealization of the flow present in the matter that is produced after a heavy ion collision. It requires the conformal EOS $\epsilon = 3p$, that resembles the EOS of nuclear matter only during the QGP phase, where the speed of sound is about $1/\sqrt{3} = 0.557$. In the near-T_c domain and during the hadronic phase, the conformal EOS is no longer applicable, and the speed of sound in the matter changes in the near T_c region, and during the hadronic phase. So, in principle, Gubser's flow should be a good description of the QGP phase of matter produced after a collision. To make the match between the idealized description and the reality of the collision, it is necessary to fix some parameters of the Gubser description such as q and T_0, and also f_* the constant of proportionality between the energy density and the fourth power of the temperature.

Let us start by addressing the issue of fixing the q-parameter. To do this we follow [34, 35] who, based in calculations from [50], chose $q = 1/4.3$ fm^{-1}. To determine this value of the parameter, they looked at the nuclear distribution before the collision, where both nuclei are taken to be moving towards each

other at the speed of light, with stress-energy tensor of the form

$$T_{uu} = f(r)\,\delta(u)\,, \qquad T_{vv} = f(r)\,\delta(v)\,, \tag{3.43}$$

with

$$u = t - z\,, \qquad v = t + z\,. \tag{3.44}$$

The function $f(r)$ describes the distribution of matter in the nucleus and its shape depends on the particular model used. In order to obtain Gubser's flow after the collision, it is necessary that the nuclei before the collision satisfy SO(3)-invariance, this together with reflection invariance imply that the distribution of nuclear matter before the collision should be [50]

$$f_{SO(3)} = \frac{2q^2 E}{\pi\left(1 + q^2 r^2\right)^3}\,, \tag{3.45}$$

where E is the energy in each of the nuclei. The distribution of matter in a real nucleus does not quite look like $f_{SO(3)}$; it is better represented by a Woods-Saxon profile,

$$f_{WS}(r) = \frac{E}{-8\pi a^3 \mathrm{Li}_3\left(-e^{R/a}\right)} \int_\infty^\infty \frac{dz}{1 + e^{\left(\sqrt{r^2 + z^2} - R\right)/a}}\,, \tag{3.46}$$

where R is the nuclear radius, a the nuclear skin depth and Li_3 a polylogarithm function. This distribution is mostly flat, and falls off towards the nuclear edge. To make the $f_{SO(3)}$ profile closer to the real distribution function the value of q is chosen such that the root-mean-squared radius weighted with the energy profile,

$$\left\langle r^2 \right\rangle = \frac{\int r^2 f(r) d\boldsymbol{r}}{\int f(r) d\boldsymbol{r}} \tag{3.47}$$

is equal when using $f_{SO(3)}$ and f_{WS}. For a gold nucleus, with values of the nuclear radius of $R = 6.38$ fm and of the nuclear skin depth of $a = 0.535$ fm [38], the parameter q is fixed to be $(4.3\,\mathrm{fm})^{-1}$, as mentioned earlier. So, while the mean squared radius of the two distributions is the same, their general shape differs. As Figure (3.1) shows the $f_{SO(3)}$ profile is more peaked at the center, and also it decays more slowly, compared to the Wood-Saxon distribution which is more spread out and decays rapidly near the nuclear edge. These differences are evidence that the model is a bit far from reality, however, it is very useful for studying the hydrodynamic phenomena that occur after the collision
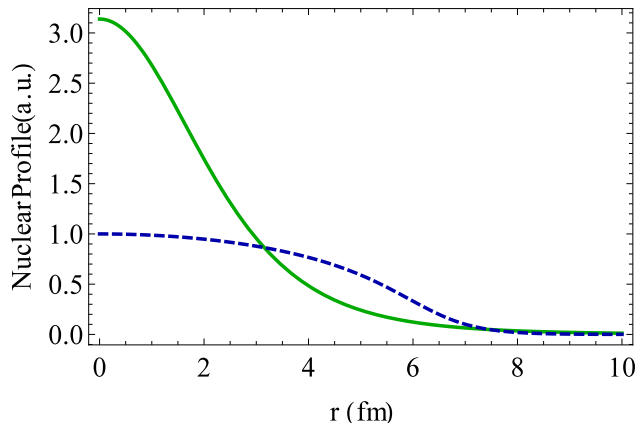
Figure 3.1: Comparison of the nuclear energy density profile for the SO(3)-invariant model (solid green) and for the Wood-Saxon model (dashed blue) in arbitrary units (a.u.). The Wood-Saxon profile is normalized to be 1 at $r = 0$, while $f_{SO(3)}$ has been normalized to have the same integral value that f_{WS} and its width has been selected to have the same root-mean-squared radius as f_{WS}, as in [50].

because, even after perturbations to the smooth background are included, the solutions to the hydrodynamic equations remain mostly analytical.

Having fixed the transverse size of the nucleus, and thus the shape of the initial energy density profile, we also need to determine the value of the $\hat{\epsilon}_0$ or equivalently of the $\hat{T}_0$ parameter, that will set the initial value of the energy density/temperature. To calculate $\hat{T}_0$, we again follow the calculations in Reference [34], and start from the total entropy for a slice of constant time τ, that is given by

$$S = \int n^\mu s_\mu \sqrt{\det\left(g_{ij}\right)} dr d\phi d\eta \,, \tag{3.48}$$

where g_{ij} is the metric for 3D space in (r, ϕ, η) coordinates, n^μ is the vector normal to the surface, and

$$s^\mu = s u^\mu \,, \tag{3.49}$$

is the entropy current, with s the entropy density, that in the case of conformal invariance corresponds to

$$s = \frac{4}{3}\frac{\epsilon}{T} \,. \tag{3.50}$$

36

We can get rid of the temperature in this equation by noting that the energy density and the temperature satisfy the relation

$$\epsilon = f_* T^4 \tag{3.51}$$

for values above the critical temperature T_c. We use $f_* = 11$, the same value adopted in Reference [34], that was extracted from lattice calculations [14, 51]. From Equation (3.48) we can get the entropy per unit rapidity

$$\frac{dS}{d\eta} = 2\pi\tau \int s u^\tau r dr \,, \tag{3.52}$$

$$= \frac{8\pi}{3\tau^2} f_*^{1/4} \hat{\epsilon}_0^{3/4} \int \frac{\cosh\kappa(\tau, r)}{(\cosh\rho(\tau, r))^2} r dr \,, \tag{3.53}$$

with κ defined in Equation (3.27) and ρ the new time coordinate from Equation (3.32). After the integral is done we can solve for

$$\hat{\epsilon}_0 = \frac{1}{f_*^{1/3}} \left(\frac{3}{16\pi} \frac{dS}{d\eta} \right)^{4/3} \,, \tag{3.54}$$

or for

$$\hat{T}_0 = \frac{1}{f_*^{1/12}} \left(\frac{3}{16\pi} \frac{dS}{d\eta} \right)^{1/3} \,, \tag{3.55}$$

that is the quantity that we use. Note that there is no time dependence on the result because we were working in the ideal case, so entropy is conserved throughout the whole process. This is not true for the viscous case, where a different calculation is needed. This computation was performed in Reference [34] for a shear viscosity to entropy ratio of $\eta/s = 0.134$ and the $\hat{T}_0$ obtained in the ideal case differed in around only 2% from the result obtained when viscosity was included, so in our calculations we simply use the same value of $\hat{T}_0$ in all cases.

The entropy per unit rapidity in Equation (3.55) can be related to experiment by the relation

$$\frac{dS}{d\eta} \approx 7.5 \frac{dN_{ch}}{d\eta} \,, \tag{3.56}$$

where the number of charged particles per unit rapidity $dN_{ch}/d\eta$ can be measured and the number 7.5 comes from calculations in Reference [50]. For central $(0-5\%)$ collisions at LHC the number of charged particles per unit rapidity

corresponds to $dN_{ch}/d\eta \sim 1600$ [52], that when plugged in Equation (3.55) gives a value of $\hat{T}_0 \approx 7.3$. When this estimate is used, the freeze-out time is approximately $\tau_{fo} \sim 6$ fm, a rather short time compared to the more realistic value of $\tau_{fo} \sim 12$ fm. We are mostly interested in studying the propagation of sound perturbations, and the size of the sound horizon depends on the freeze-out time, so to have a more realistic estimate of the displacement of the perturbations, we use $\hat{T}_0 = 10.1$, that corresponds to having about $2.6(dN_{ch}/d\eta)_{LHC}$.

In the ideal case, the background temperature in flat space corresponds to

$$T = \frac{1}{\tau f_*^{1/4}} \frac{\hat{T}_0}{(\cosh \rho(\tau,\, r))^{2/3}} \; ; \tag{3.57}$$

this means we are using an initial temperature at the center of the fireball of about 630 MeV. The temperature and overall entropy that we use in our calculations is rather large, however, by fixing $\hat{T}_0$ thus, we ensure a realistic size of the fireball at freeze-out, and overall transverse expansion velocities that mimic the reality of RHIC/LHC collisions.

Now that we have fixed the parameters of the flow, there is still one more issue we must determine before we can start exploring it: we need to set the time when the hydrodynamical description starts to be applicable. Right after the collision the system is not in equilibrium, and it needs to reach an approximate equilibrium before hydrodynamics starts to give a correct description of the situation. While the mechanism of equilibration remains unknown, its duration is known to be of about a fraction of fm/c. In our calculations we assume that thermalization occurs at time $\tau = 1$ fm/c, and it is at this time that we define our initial conditions and start evolving using hydrodynamics. The evolution lasts until the final freeze-out is reached, at which point the interaction between secondaries becomes ineffective and sound propagation stops.

3.4 Perturbations on Top of the SO(3)-invariant Flow

The SO(3)-inavariant flow gives a smooth description of the energy density, temperature, and flow of the matter formed after a heavy ion collision; however, in reality there are fluctuations of these quantities due to the fluctuations of the positions of the nucleons in the nuclei as described in Chapter 2. To include this in our description of the fireball, it is necessary to consider small perturbations to Gubser's flow, that will modify the overall temperature and
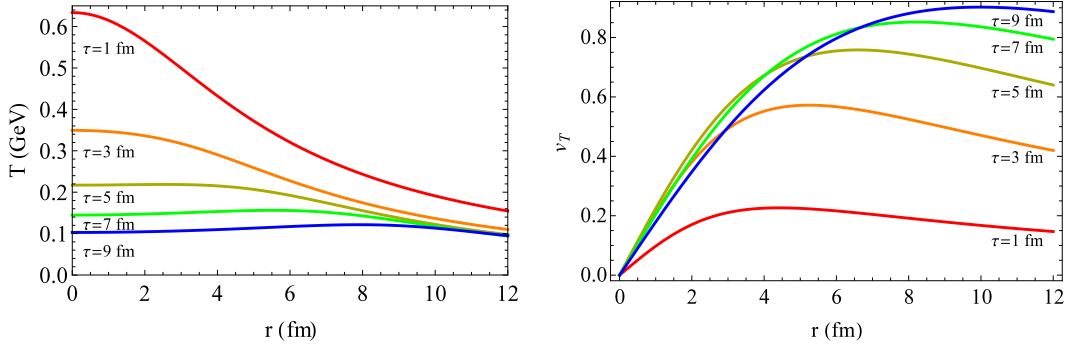
Figure 3.2: Temperature (left) and transverse velocity(right) profiles for the SO(3)-invariant flow solution at different times.

velocity profiles of the nuclear matter under study. It is now, when looking at perturbations to the background flow, that the benefits of performing the Weyl rescaling and the change of coordinates to make the SO(3)-invariance explicit become evident. In what follows of this section we describe how perturbations to the flow are added to the SO(3)-invariant flow as it was done in [35] and later in [31].

Let us first describe the ideal case, where the background temperature is given by just the first term in Equation (3.38). Both the background temperature (now called $\hat{T}_B$) and the background four-velocity (now $\hat{u}_{B\,\mu}$) receive a perturbation such that the total temperature and four-velocity in the rescaled frame correspond to

$$\hat{T} = \hat{T}_B(1+\delta)\,, \tag{3.58}$$

$$\hat{u}_\mu = \hat{u}_{B\,\mu} + \hat{u}_{P\,\mu}\,, \tag{3.59}$$

where δ and $\hat{u}_{P\,\mu}$ are the perturbations to the original solutions for the temperature and the velocity, respectively. Both of these quantities could in principle depend on all four coordinates (ρ, θ, ϕ, η), but for the time being we will disregard perturbations in rapidity. The reasoning behind this decision is that for now we are only interested in including perturbations in the transverse plane, so that the waves they induce propagate also in the transverse plane only. This is because the features present in two particle correlations from RHIC and LHC–the near side ridge and the away side shoulders–are rapidity independent, and we work under the assumption that they appear because of rapidity-independent initial state perturbations in the transverse plane. So for

39

now we will use

$$\delta = \delta(\rho,\,\theta,\,\phi) \tag{3.60}$$

$$\hat{u}_{P\,\mu} = (0,\,\hat{u}_\theta(\rho,\,\theta,\,\phi),\,\hat{u}_\phi(\rho,\,\theta,\,\phi),\,0)\,, \tag{3.61}$$

and reserve perturbations in rapidity for a later chapter. Notice that corrections to the ρ-component of the four velocity have been omitted, this is because they only appear at quadratic order, they do not contribute to the linear perturbations that we explore.

When the expressions (3.58) and (3.59) are plugged into the hydrodynamic equations and only the linear terms in the perturbation are kept, one obtains a system of coupled first-order differential equations. These equations may be re-written as a second-order differential equation for one of the perturbations; for delta the equation reads

$$\frac{\partial^2 \delta}{\partial \rho^2} - \frac{1}{3\cosh^2\rho}\left(\frac{\partial^2\delta}{\partial\theta^2} + \frac{1}{\tan\theta}\frac{\partial\delta}{\partial\theta} + \frac{1}{\sin^2\theta}\frac{\partial^2\delta}{\partial\phi^2}\right) + \frac{4}{3}\tanh\rho\frac{\partial\delta}{\partial\rho} = 0\,. \tag{3.62}$$

This equation can be solved exactly, but before going into that we start by simply studying the solution in the short wavelength approximation, to get a general idea of its behavior.

3.4.1 The short wavelength approximation for the sound waves on top of the SO(3)-invariant flow

We want to look at the oscillatory behavior of the solution, so we start by assuming that the solution will be an oscillatory exponential function times some function that will determine the amplitude. Furthermore, we use variable separation, so we start from a function of the form

$$\delta = e^{i(f_\rho(\rho) - f_\theta(\theta) - f_\phi(\phi))} F_\rho(\rho) F_\theta(\theta) F_\phi(\phi)\,, \tag{3.63}$$

where $f_i >> 1$, such that the derivatives taken over the exponential are dominant. When we take this solution and plug it into Equation (3.62) we have terms with different powers of the derivatives of the f_i functions; in this way, we study the equation separating it in different equations depending on which power of the derivatives over the exponent they have. The first step is to look only at the second derivatives, because they produce terms of second order in

the exponent, they are the leading ones. In this way we find

$$f_\rho(\rho) = \pm \frac{2}{\sqrt{3}} k \arctan e^\rho + A \,, \tag{3.64}$$

$$f_\theta(\theta) = \pm \int d\theta \sqrt{k^2 - \frac{m^2}{\sin^2\theta}} + B \,, \tag{3.65}$$

$$f_\phi(\phi) = \pm m\phi + C \,. \tag{3.66}$$

The integral in (3.65) can be solved, but it gives a cumbersome result. So in what follows (of this subsection) we assume no ϕ dependence just to get an idea of the result. When we do this, the functions in the exponent reduce to

$$f_\rho(\rho) = \pm \frac{2}{\sqrt{3}} k \arctan e^\rho + A \,, \tag{3.67}$$

$$f_\theta(\theta) = \pm k\theta + B \,. \tag{3.68}$$

$$\tag{3.69}$$

The function $f_\rho(\rho)$ is almost linear in ρ in the region that we are interested in studying $(-2 < \rho < 1)$, so we find the phase of the solution to be $\sim k\rho$, which means that we indeed expect to find solutions in the form of the sound wave propagation (in this region).

Now that we have found the functions in the exponent we look for the wave amplitude by canceling among themselves the terms with the first power of the large exponent: By doing this we find the amplitudes to be

$$F_\rho(\rho) \sim \frac{1}{(\cosh \rho)^{1/6}} \,, F_\theta(\theta) \sim \frac{1}{\sin \theta} \tag{3.70}$$

3.4.2 The exact separation of variables for the perturbation

In the previous section we studied the general behavior of the solution to the perturbation equation (3.62) in the short wavelength approximation, but now we look for the exact solution. Again we use variable separation, and plug $\delta(\rho, \theta, \phi) = \delta(\rho)\Theta(\theta)\Phi(\phi)$ in Equation (3.62), finding three separate equations

for the $\delta(\rho)$, $\Theta(\theta)$ and $\Phi(\phi)$ functions

$$\delta''(\rho) + \frac{4}{3}\tanh\rho\,\delta'(\rho) + \frac{\lambda}{3\cosh^2\rho}\delta(\rho) = 0\,, \tag{3.71}$$

$$\Theta''(\theta) + \frac{1}{\tan\theta}\Theta'(\theta) + \left(\lambda - \frac{m^2}{\sin^2\theta}\right)\Theta(\theta) = 0\,, \tag{3.72}$$

$$\Phi''(\phi) + m^2\Phi(\phi) = 0\,, \tag{3.73}$$

that are analytically solvable, and yield

$$\delta(\rho) = \frac{1}{(\cosh\rho)^{2/3}}\left(C_1 P^{2/3}_{-\frac{1}{2}+\frac{1}{6}\sqrt{12\lambda+1}}(\tanh\rho) + C_2 Q^{2/3}_{-\frac{1}{2}+\frac{1}{6}\sqrt{12\lambda+1}}(\tanh\rho)\right) \tag{3.74}$$

$$\Theta(\theta) = C_3 P^m_l(\cos\theta) + C_4 Q^m_l(\cos\theta) \tag{3.75}$$

$$\Phi(\phi) = C_5 e^{im\phi} + C_6 e^{-im\phi} \tag{3.76}$$

where $\lambda = l(l+1)$ and P and Q are associated Legendre Polynomials. The part of the solution depending on θ and ϕ can be combined to form spherical harmonics $Y_{lm}(\theta, \phi)$, such that $\delta(\rho, \theta, \phi) \propto \delta_l(\rho)Y_{lm}(\theta, \phi)$. The spherical harmonics are orthogonal functions, so any function can be decomposed into a sum of them, this will allow us to define a desired shape for the initial conditions and to write them as combinations of the $Y_{lm}(\theta, \phi)$. Then, by simply multiplying the spherical harmonics by the ρ-dependent part of the solution $\delta(\rho)$, one can obtain the evolution of the specified initial system.

Using Gubser's solution one has from the beginning of the hydrodynamic evolution an analytical fuction that describes the ϕ-dependence of the temperature and the velocity of othe fluid. This dependence can be related to the final particle distribution in the azimuthal angle ϕ, that is usually expanded in its Fourier components and quantities associated to different values of m are referred to as different harmonics. In this model, to each m correspond many values of l, as long as the condition $l \leq m$ holds. The radial dependence is associated to the number l, and thus different values of l will produce different radial dependences, though traditionally (as we did when using the Glauber model in Chapter 2), to each value of m is associated only a r^m term, except for $m = 1$ that uses r^3. Now, we consider a more general form for the radial dependence, just determined by the initial conditions for θ and for the evolution in ρ.

Let us now explore the asymptotic behavior of the Legendre functions when

$l >> 1$ that is given by Reference [53]:

$$P_l^m(\cos\theta) = \frac{2}{\sqrt{\pi}} \frac{\Gamma(l+m+1)}{\Gamma(l+\frac{3}{2})} \frac{\cos\left[(l+\frac{1}{2})\theta - \frac{\pi}{4} + \frac{m\pi}{2}\right]}{\sqrt{2\sin\theta}} \qquad (3.77)$$

$$Q_l^m(\cos\theta) = \sqrt{\pi}\frac{\Gamma(l+m+1)}{\Gamma(l+\frac{3}{2})} \frac{\cos\left[(l+\frac{1}{2})\theta + \frac{\pi}{4} + \frac{m\pi}{2}\right]}{\sqrt{2\sin\theta}} \qquad (3.78)$$

These expressions show that for large l the solution presents oscillatory behavior in θ with an amplitude given by $\frac{1}{\sqrt{\sin\theta}}$, the same as we obtained in the short wavelength approximation for $F_\theta(\theta)$ in the previous section.

For the ρ-dependent part of the solution we proceeed in the same way. In the large l limit the Legendre polynomials as a function of $\tanh\rho$ correspond to

$$P_l^m(\tanh\rho) = \sqrt{\frac{2}{\pi}}\frac{\Gamma(l+m+1)}{\Gamma(l+3/2)}\sqrt{\cosh\rho}$$
$$\cos\left(\left(l+\frac{1}{2}\right)\arccos(\tanh\rho) - \frac{\pi}{4} + \frac{m\pi}{2}\right), \qquad (3.79)$$

$$Q_l^m(\tanh\rho) = \sqrt{\frac{\pi}{2i}}\frac{\Gamma(l+m+1)}{\Gamma(l+3/2)}\sqrt{\cosh\rho}$$
$$\cos\left(\left(l+\frac{1}{2}\right)\arccos(\tanh\rho) + \frac{\pi}{4} + \frac{m\pi}{2}\right). \qquad (3.80)$$

Again we see an oscillatory behavior and a wave amplitude. In this case the amplitude is given by $\sqrt{\cosh\rho}$ and if we divide this by $(\cosh\rho)^{2/3}$ as we have in the exact solution (3.74), we get an amplitude for the wave of $\frac{1}{(\cosh\rho)^{1/6}}$, which is the same as we got in the preceding section using the short wavelength approximation.

So we have checked that for large l the function $\delta(\rho,\theta,\phi)$, and therefore the temperature perturbation in the rescaled frame $\hat{T}_1(\rho,\theta,\phi) = \hat{T}_b(\rho)\delta(\rho,\theta,\phi)$, does behave like a sound wave. In Figure (3.3) we present the evolution in ρ of both the $\delta_l(\rho)$ and the $v_l(\rho)$ function in the region of interest that coincides with the time during which the fireball evolves hydrodynamically. Only terms with values of l up to 10 are presented, and in both cases they show oscillatory behavior for larger values of l, as expected.

3.4.3 Viscous Effects

In [30] we introduced the viscosity-based scale, which all structures produced by pointlike perturbations would obtain at freeze-out. Without going into
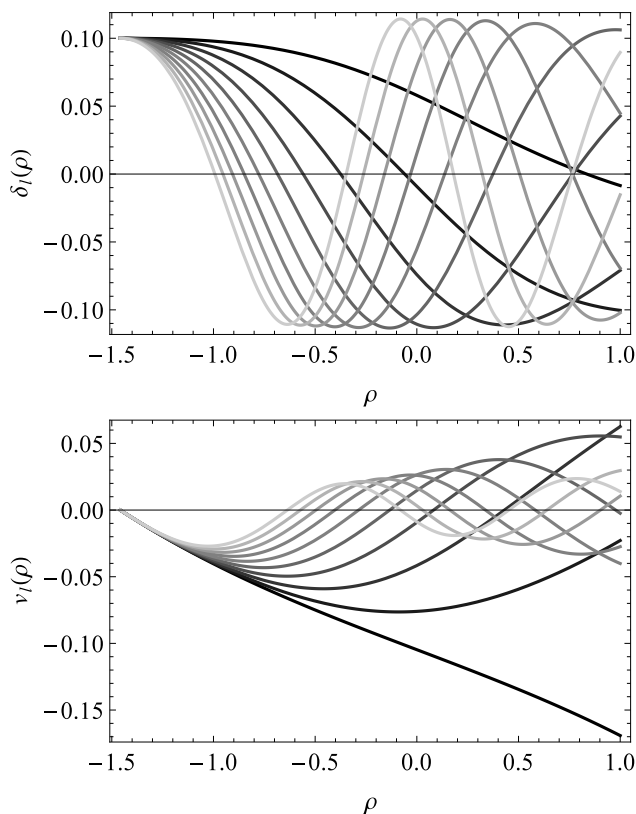
Figure 3.3: The ρ-dependent part of the temperature $\delta_l(\rho)$ (top) and the velocity $v_l(\rho)$ (bottom) perturbations to Gubser's flow for values of l=1..10, the shade of gray of the curves gets lighter as l increases.

detail, let us just remind the reader that while the width of the circle grows with time as $\tau^{1/2}$, its radius grows as τ, and therefore the relative contrast (the former divided by the latter) is improving as $\tau^{-1/2}$. As far as the amplitude of the wave is concerned, in a short-plain-wavelength approximation the stress tensor harmonics with momentum k are attenuated by a factor

$$\delta T_{\mu\nu}(t,k) = \exp\left(-\frac{2}{3}\frac{\eta}{s}\frac{k^2 t}{T}\right)\delta T_{\mu\nu}(0,k) \tag{3.81}$$

known from textbooks on sound (*e. g.* [54]), sometimes called the viscous filter. Note that the exponent contains the momentum squared, owing to the extra derivative in the viscous tensor, and therefore, the effect of viscosity for the higher harmonics is strongly enhanced (see [55] for studies of the viscous filter). Obviously, the same qualitative behavior is expected for our l, m harmonics.

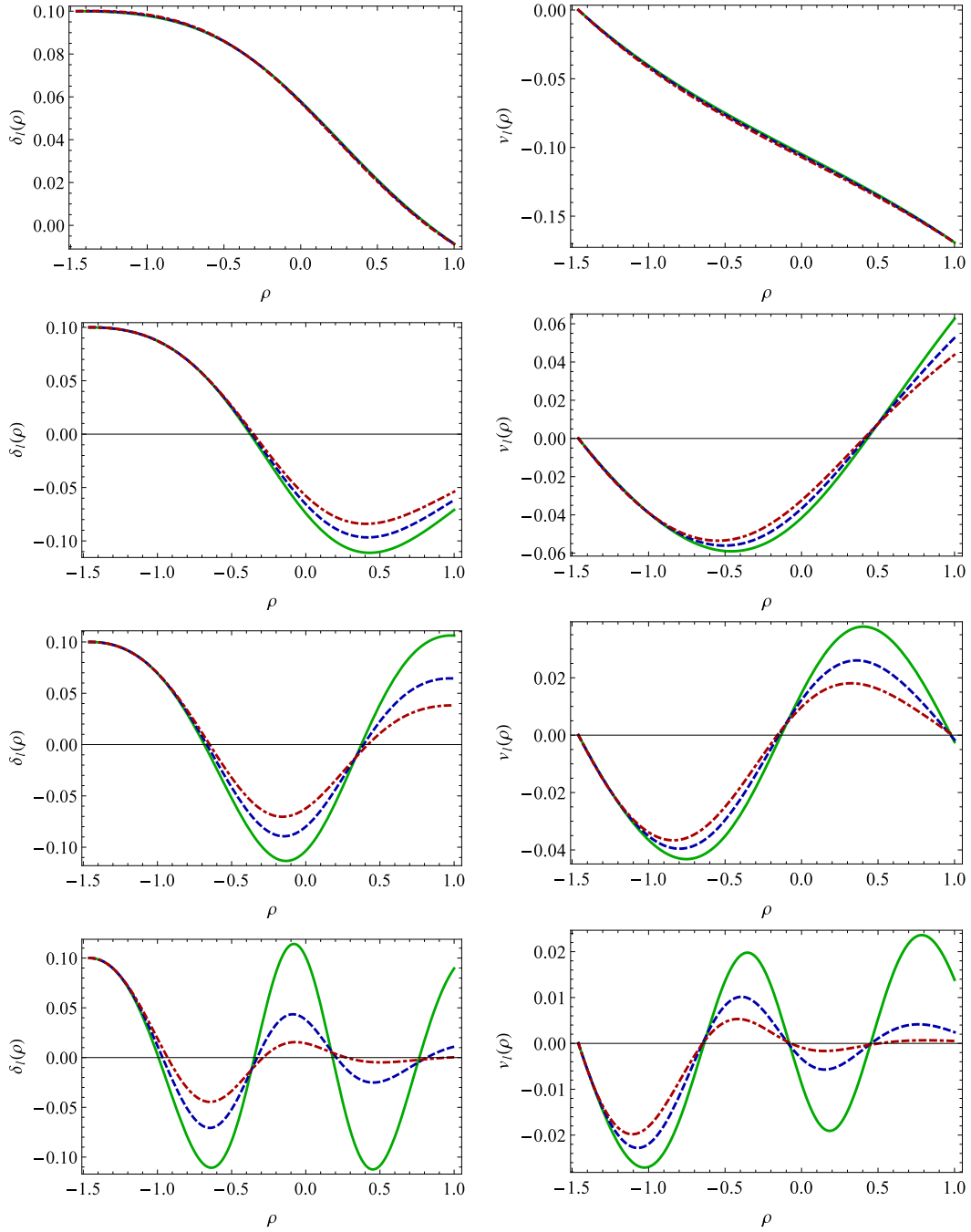Figure 3.4: The effect of viscosity on the ρ-dependent part of the temperature $\delta_l(\rho)$ (left) and the velocity $v_l(\rho)$ (right) perturbations to Gubser's flow for four different values of l (l=1,3,5,10) increasing from top to bottom. The values of η/s used are 0 (solid green line), $1/4\pi$ (dashed blue line), and $1/2\pi$ (dash-dotted red line).

The basic equations for the ρ-dependent part of the perturbation, now with viscosity terms, can be written as a system of coupled first-order equations [35]. We are assuming rapidity independence; thus, the systems of Eqs. (107), (108), and (109) from the referred paper become two coupled equations, for the ρ-dependent part of the temperature and the velocity perturbations,

$$\frac{d\boldsymbol{w}}{d\rho} = -\Gamma\boldsymbol{w}, \qquad \boldsymbol{w} = \begin{pmatrix} \delta_v \\ v_v \end{pmatrix} \tag{3.82}$$

where the index v stands for viscous and the matrix components are

$$\Gamma_{11} = \frac{H_0 \tanh^2 \rho}{3\hat{T}_B} \tag{3.83}$$

$$\Gamma_{12} = \frac{l(l+1)\left(H_0 \tanh \rho - \hat{T}_B\right)}{3\hat{T}_B \cosh^2 \rho} \tag{3.84}$$

$$\Gamma_{21} = 1 + \frac{2H_0 \tanh \rho}{H_0 \tanh \rho - 2\hat{T}_B} \tag{3.85}$$

$$\Gamma_{22} = \frac{8\hat{T}_B^2 \tanh \rho + H_0 \hat{T}_B \left(-4\left(3l(l+1) - 10\right)(\cosh \rho)^{-2} - 16\right) + 6H_0^2 \tanh^3 \rho}{6\hat{T}_B \left(H_0 \tanh \rho - 2\hat{T}_B\right)} \tag{3.86}$$

This system can also be written as a closed second-order differential equation for δ_v:

$$\frac{d^2\delta_v}{d\rho^2} - \frac{d\delta_v}{\delta\rho}\left(\Gamma_{11} - \frac{1}{\Gamma_{12}}\frac{d\Gamma_{12}}{d\rho} + \Gamma_{22}\right)$$
$$- \delta_v\left(\frac{d\Gamma_{11}}{d\rho} - \frac{\Gamma_{11}}{\Gamma_{12}}\frac{d\Gamma_{12}}{d\rho} + \Gamma_{11}\Gamma_{22} + \Gamma_{12}\Gamma_{21}\right) = 0 \tag{3.87}$$

Unfortunately, unlike the zero-viscosity case considered above, the equations one gets after separation of variables cannot all be solved analytically and thus they need to be solved numerically, which has been done using MATHEMATICA's ordinary differential equation solver. The part of the solution that depends on θ and ϕ is not affected by viscosity, so it continues to be given by the spherical harmonics $Y_{lm}(\theta, \phi)$.

Our results for the nonzero viscosity use either $H_0 = 0.33$ ($\eta/s = 0.134$), such as in Reference [35], or the value $H_0 = 0.19$ ($\eta/s = 1/(4\pi) = 0.08$), the conjectured lowest value possible predicted by AdS/CFT in the strong coupling limit.

In Figure (3.4) we plot the time dependence $\delta_{vl}(\rho)$ for several harmonics and compare them to the inviscid case $\delta_l(\rho)$ for some l's. As expected, the viscosity reduces higher harmonics more, but as far as time dependence is compared to the inviscid case, we see that viscosity literally kills the contribution at a certain time, which becomes shorter and shorter for larger l. As the time is limited by freeze-out time, we observe that contributions of all sufficiently large $l > l_{max} \sim 10$ become completely negligible.

The ρ-dependent part of the velocity can be calculated once δ_{vl} is known

$$v_{vl}(\rho) = -\frac{\delta'_{vl} + \Gamma_{11}\delta_{vl}}{\Gamma_{12}} \tag{3.88}$$

The curves for the ρ-dependent part of the velocity $v_{vl}(\rho)$ are plotted in Figure (3.4), for differnt values of viscosity. Comparing this to $v_l(\rho)$ at zero viscosity we see that the amplitude for the velocity is also damped in the viscous case for large l and increasing ρ.

3.5 Propagation of a local initial state perturbation

We have already described the tools for the evolution of the SO(3)-invariant flow and of perturbations on top of it, now we will proceed to describe the initial conditions that we study. Motivated by the idea of hot spots described in Chapter 2 we will consider a Gaussian perturbation to the background, and study its evolution.

The idea is that when a heavy ion collision takes place, there will be hot spots formed in the new matter at locations in the transverse plane where a large number of nucleons collide. These hot spots, as well as the average background, are expected to evolve through the hydrodynamic equations until the matter freezes out, leaving a particular azimuthal distribution that can be then measured in detectors. What we do is to simulate one of these hot spots by placing a Gaussian at $\rho = \rho_0$. We use as starting time for hydrodynamics the time $\tau = 1$ fm, so the value of ρ_0 is determined by this time and by the radial position where the hot spot is placed.

The initial Gaussian in the θ and ϕ coordinates

$$\delta(\rho_0,\,\theta,\,\phi) \propto e^{\frac{\theta^2+\theta_0^2-2\theta\theta_0\cos{(\phi-\phi_0)}}{2s^2}}, \tag{3.89}$$

where θ_0 is the location of the perturbation in the θ-coordinate determined by $\tau = 1$ fm, and by the radial position of the Gaussian, and ϕ_0 is the azimuthal

location of the Gaussian, may be re-written as a sum of spherical harmonics.

$$\delta(\rho_0, \theta, \phi) = \sum_{lm} c_{lm} \delta_l(\rho_0) Y_{lm}(\theta, \phi), \qquad (3.90)$$

where the function $\delta_l(\rho)$, will determine the evolution. The coefficients c_{lm} will be specific for any initial condition, and they are calculated using the orthogonality condition of the spherical harmonics

$$c_{lm} = \int_0^{2\pi} \int_0^{\pi} \delta(\rho_0, \theta, \phi) Y_{lm}^*(\theta, \phi) \sin\theta d\theta d\phi. \qquad (3.91)$$

The function $\delta_l(\rho)$, presented in Equation(3.74) needs to have its constants C_1 and C_2 fixed at some value. To fix them we use two initial conditions $\delta(\rho_0) = 1$ and $v_l(\rho_0) = 0$, and because for inviscid case

$$v_l(\rho) = \frac{3\cosh^2\rho}{l(l+1)} \frac{d\delta_l}{d\rho}, \qquad (3.92)$$

the second condition just means that

$$\left. \frac{d\delta_l}{d\rho} \right|_{\rho=\rho_0} = 0. \qquad (3.93)$$

With this, the constants C_1 and C_2 are fixed, and the function δ_l is given by

$$\delta_l(\rho) = \frac{\left.\frac{dq_l}{d\rho}\right|_{\rho_0} p_l(\rho) - \left.\frac{dp_l}{d\rho}\right|_{\rho_0} q_l(\rho)}{\left.\frac{dq_l}{d\rho}\right|_{\rho_0} p_l(\rho_0) - \left.\frac{dp_l}{d\rho}\right|_{\rho_0} q_l(\rho_0)} \qquad (3.94)$$

with

$$p_l(\rho) = \frac{1}{(\cosh\rho)^{2/3}} P^{2/3}_{-\frac{1}{2}+\frac{1}{6}\sqrt{12l(l+1)+1}}(\tanh\rho), \qquad (3.95)$$

and

$$q_l(\rho) = \frac{1}{(\cosh\rho)^{2/3}} Q^{2/3}_{-\frac{1}{2}+\frac{1}{6}\sqrt{12l(l+1)+1}}(\tanh\rho). \qquad (3.96)$$

It is interesting to note that the denominator in Equation (3.94) has the form of Wronskian of the fucntions p_l and q_l evaluated at ρ_0. Because the associated Legendre functions P^ν_μ and Q^ν_μ are linearly independent, the denominator is
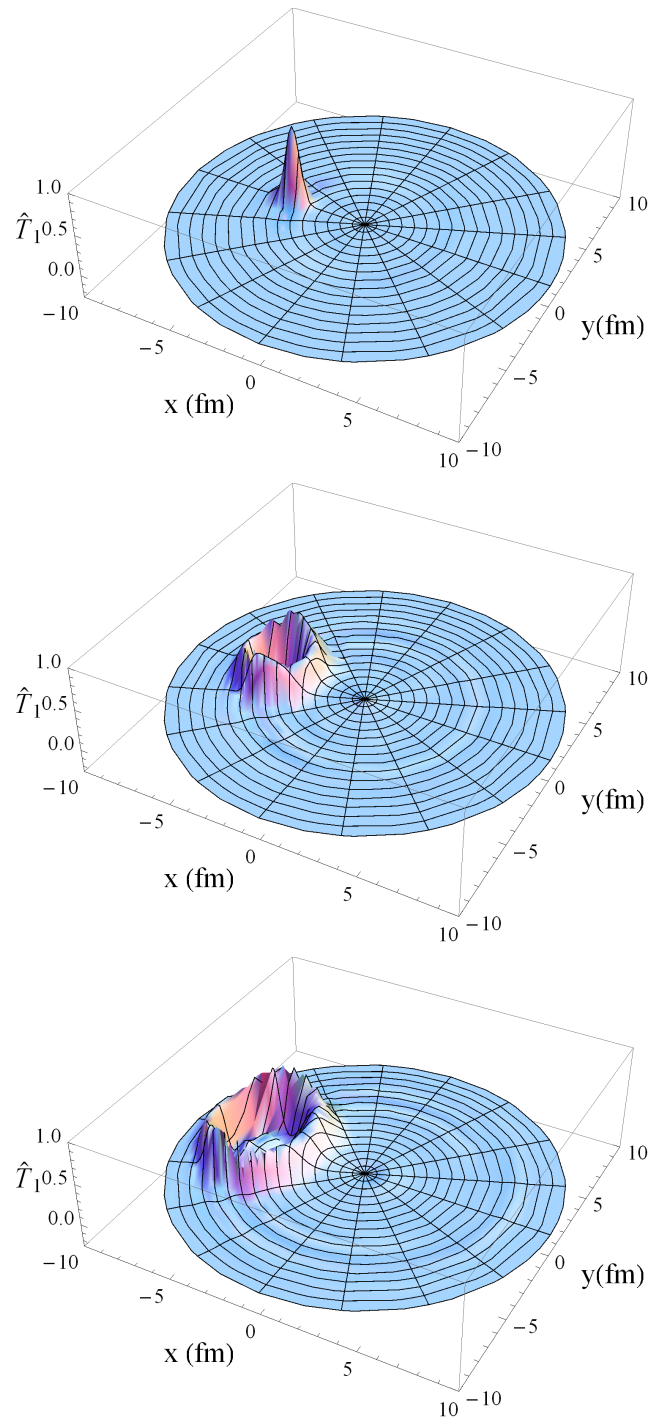
Figure 3.5: Evolution of the initial Gaussian perturbation in the rescaled frame but in the regular coordinates (τ, r, ϕ). From top to bottom: $\tau = 1$ fm/c, $\tau = 4$ fm/c, $\tau = 6$ fm/c.

going to be non-zero for any value of ρ_0 that is chosen, thus the function $\delta_l(\rho)$ will always be finite.

With all the constants determined by the chosen initial conditions, it is possible to study the evolution of the initial Gaussian perturbation. Figure (3.5) shows a Gaussian perturbation in the rescaled frame at initial time, and how it has evolved into an expanding circle after some time has elapsed. The Gaussian shown here was originally placed at $\tau = 1$ fm, $\theta = 1.5$, and $\phi = \pi$, and has a width $s = 0.1$. When changing to the more usual coordinates this corresponds to an original radial position $r = 4.1$ fm and a width of 0.4 fm. The picture was obtained by combining all the spherical harmonics with $|m| < l$ up to $l = 30$, that as can be seen add up coherently to form a consistent picture of sound-wave propagation.

Chapter 4

Final Particle Distribution and Flow Harmonics

In this chapter we try to connect our results to real data measured in heavy ion collisions. Detectors at both, RHIC and LHC, measure the particles that go through them, so to be able to compare the results we obtain using the SO(3)-invariant flow to the experiments it is necessary to change from the fluid description that we have been considering to a particle description. The final particle distribution, and also the correlations between particles are measured in experiment, and thus these are the quantities that we need to obtain as a final result.

4.1 Freeze-out and the Cooper-Frye Mechanism

As a consequence of the expansion of the fireball its temperature and energy density decrease, and when the latter is around $\epsilon \sim 1$ GeV/fm the process of hadronization–when partons become hadrons–takes place. The hadronic matter continues to interact through elastic and inelastic scattering. The moment when inelastic scattering stops is known as chemical freeze-out, while the moment when aslso elastic scattering stop is known as kinetic freeze-out. The surface at which all scattering processes stops is the freeze-out surface, also called the surface of last scattering. It is at this point–when the matter becomes dilute and thus the interactions, ineffective–that we change from the fluid description to the particle description. The distribution of particles that one obtains on the freeze-out surface should be the same as the one measured in the detectors, because at this point all of the interactions have stopped.

The Cooper-Frye formula [56], connects the fluid and the particle descriptions, and gives the distribution of particles after freeze-out. The method is described nicely in many references (see *e. g.* [57–59]), but for completeness we include it here. The distribution of particles in phase-space after freeze-out is given by

$$E\frac{dN}{d^3p} = \frac{dN}{dyp_Tdp_Td\Phi} = \int f\left(\frac{P^\mu u_\mu}{T}\right)p^\mu d\Sigma_\mu\,, \tag{4.1}$$

where f is the distribution function, $d^3\Sigma_\mu$ is the normal to the freeze-out hyper-surface, T is the temperature, p_T is the transverse momentum of the particle,

$$y = \frac{1}{2}\ln\frac{E+p_L}{E-p_L} \tag{4.2}$$

is the rapidity,

$$m_T = \sqrt{m^2 + p_T^2}\,, \tag{4.3}$$

is the transverse mass, and Φ momentum azimuthal angle. The distribution function depends on the kind of particle being studied, it can be either a Bose or a Fermi distribution

$$f\left(\frac{p^\mu u_\mu}{T}\right) = \frac{g_i}{(2\pi)^3}\frac{1}{e^{\frac{p^\mu u_\mu - \mu_i}{T}} \pm 1} \tag{4.4}$$

depending on if one is dealing with bosons or with fermions. The coefficient g_i represents the degeneracy of the species i of particles. Because we study cases with high transverse momentum ($p_T \gtrsim 1$) GeV we may use the classical approximation, the Boltzmann distribution function

$$f\left(\frac{p^\mu u_\mu}{T}\right) = \frac{g_i}{(2\pi)^3}e^{\frac{-p^\mu u_\mu}{T}}\,, \tag{4.5}$$

that for large p_T's is similar to both the Bose and the Fermi distributions.

The integral that we want to calculate to compute the final distribution of particles is

$$\frac{dN_i}{dyp_Tdp_Td\Phi} = -\frac{g_i}{(2\pi)^3}\int e^{\frac{p^\mu u_\mu}{T}}p^\mu d\Sigma_\mu\,, \tag{4.6}$$

where the minus sign in the exponent has been removed because we work in the

$(-, +, +, +)$ signature, and expressions (4.4),(4.5) were for the mostly minus metric. For the same reason, a minus sign is in front of the whole expression.

The four-momentum in Minkowski space is

$$p^\mu = (p^0,\, p^x,\, p^y,\, p^z) \tag{4.7}$$
$$= (m_T \cosh y,\, p_T \cos \Phi,\, p_T \sin \Phi,\, m_T \sinh y)\,, \tag{4.8}$$

but we work using the hyperbolic metric in the $(\tau,\, r,\, \phi,\, \eta)$ coordinates, performing the transformation:

$$p_\mu = \frac{\partial \bar{x}^\nu}{\partial x^\mu} p_\nu\,, \tag{4.9}$$

the four momentum becomes

$$p^\mu = (p^\tau,\, p^r,\, p^\phi,\, p^\eta)\,, \tag{4.10}$$
$$= (m_T \cosh(y-\eta),\, p_T \cos(\Phi-\phi),\, \frac{p_T}{r}\sin(\Phi-\phi),\, \frac{m_T}{\tau}\sinh(y-\eta))\,. \tag{4.11}$$

To calculate the term in the exponent we need also the four-velocity

$$u_\mu = (u_\tau,\, u_r,\, u_\phi,\, u_\eta)\,, \tag{4.12}$$
$$= (u_{B\tau} + \delta u_\tau,\, u_{Br} + \delta u_r,\, \delta u_\phi,\, 0)\,, \tag{4.13}$$

where

$$u_{B\tau} = -\cosh \kappa(\tau, r)\,, \tag{4.14}$$
$$u_{Br} = \sinh \kappa(\tau, r)\,, \tag{4.15}$$

are the background flow, while all the other terms are due to the perturbation of the background, and are given explicitly by

$$\delta u_\tau = \tau \frac{\partial \theta}{\partial \tau} \hat{u}_\theta\,, \tag{4.16}$$
$$\delta u_r = \tau \frac{\partial \theta}{\partial r} \hat{u}_\theta\,, \tag{4.17}$$
$$\delta u_\phi = \tau \hat{u}_\phi\,. \tag{4.18}$$
$$\tag{4.19}$$

For now we only work in the transverse plane, that is why no perturbation in the η direction was included. The terms with hats $\hat{u}_\theta$ and $\hat{u}_\phi$ correspond

to the θ and ϕ components of velocity perturbations in the rescaled frame, respectively. Then the product $p^\mu u_\mu$ in the exponent is

$$p^\mu u_\mu = m_T \cosh{(y-\eta)}\left(u_{B\tau} + \delta u_\tau\right) + p_T \cos{(\Phi - \phi)}\left(u_{Br} + \delta u_r\right)$$
$$+ p_T \frac{\sin{(\Phi - \phi)}}{r}\delta u_\phi\,. \tag{4.20}$$

The last thing needed to compute the final particle distribution is the freeze-out surface,

$$\Sigma^\mu = \left(\Sigma^0,\,\Sigma^x,\,\Sigma^y,\,\Sigma^z\right), \tag{4.21}$$

and its normal. In general, the freeze-out surface, being a 3-dimensional space, can be parameterized by three parameters

$$\Sigma^\mu = \left(\tau_{fo}(r,\,\phi)\cosh\eta,\,x,\,y,\,\tau_{fo}(r,\,\phi)\sinh\eta\right) \tag{4.22}$$

or in $(\tau,\,r,\,\phi,\,\eta)$ coordinates

$$\Sigma^\mu = \left(\Sigma^\tau,\,\Sigma^r,\,\Sigma^\phi,\,\Sigma^\eta\right), \tag{4.23}$$
$$= \left(\tau_{fo}(r,\phi),\,r,\,\phi,\,\eta\right). \tag{4.24}$$

τ_{fo} is the freeze-out time, and in general it could also depend on the η-coordinate, but because we are only looking at perturbations in the transverse plane, we don't include this dependence. The freeze-out time is the time at which decoupling occurs, when the matter transitions from a state of thermal equilibrium to free particles. To determine this time, and thus the freeze-out surface, there are different prescriptions such as to consider isochronous freeze-out, when the decoupling happens at a constant time, or isothermal freeze-out, when it happens at a constant temperature. This last approach, resembles more a realistic situation, when the decoupling happens as the fireball expands and the energy density decreases, and it is thus

$$T(\tau,\,r,\,\phi) = T_{fo} \tag{4.25}$$

the freeze-out condition that we use.

The normal to the freeze-out surface is calculated by

$$d^3\Sigma_\mu = -\sqrt{-\det g}\,\varepsilon_{\mu\nu\lambda\rho}\frac{\partial\Sigma^\nu}{\partial r}\frac{\partial\Sigma^\lambda}{\partial\phi}\frac{\partial\Sigma^\rho}{\partial\eta}dr d\phi d\eta\,, \tag{4.26}$$

$$= -\varepsilon_{\mu\nu\lambda\rho}\frac{\partial\Sigma^\nu}{\partial r}\frac{\partial\Sigma^\lambda}{\partial\phi}\frac{\partial\Sigma^\rho}{\partial\eta}\tau r dr d\phi d\eta\,, \tag{4.27}$$

where

$$\epsilon^{\mu\nu\lambda\rho} = -\epsilon_{\mu\nu\lambda\rho} = \left\{ \begin{array}{cl} 1 & \text{even permutation} \\ -1 & \text{odd permutation} \\ 0 & \text{otherwise} \end{array} \right. , \qquad (4.28)$$

so in the case of isochronous freeze-out the surface elmente is given by

$$d^3\Sigma_\mu = (-1,\, 0,\, 0,\, 0)\tau r dr d\phi d\eta \qquad (4.29)$$

while for isothermal freeze-out it corresponds to

$$d^3\Sigma_\mu = (-1,\, \frac{\partial\tau}{\partial r},\, \frac{\partial\tau}{\partial\phi},\, 0)\tau r dr d\phi d\eta \qquad (4.30)$$

We will work in this last case, but before looking at perturbations to the flow, let us analyze the freeze-out surface due to the background, when the only dependece is in the r-coordinate. Then, the freeze-out time can be calculated by solving

$$\frac{d\tau_{fo}}{dr} = -\frac{(\partial T_B/\partial r)}{(\partial T_B/\partial\tau)} . \qquad (4.31)$$

The red curve in the left plot in Figure (4.1) shows the freeze-out time calculated in this way, when the freeze-out temperature is taken to be $T_{fo} = 120$ MeV, while the plot on the right shows the transverse velocity evaluated at the freeze-out time. The shape of the obtained freeze-out surface for large values of the radial coordinate ($r > 9$ fm) is qualitatively different from what is expected to occur in real collisions. The initial tail of Gubser's flow energy density is power-like as seen in Figure (3.1), and so a tail is also present in the freeze-out time profile: for smaller times the freeze-out surface is at large r, while for later times it rises. This behavior is not compatible with the more realistic behavior of the fireball starting with a smaller radius (~ 7 fm) and expanding at later times, which would yield a freeze-out surface that moves outwardly instead of inwardly for increasing times . The main effect of this difference is the sign of the particle flow direction, determined by the sign of $p^\mu d^3\Sigma_\mu$. If one simply does not include the almost vertical part of the freeze-out surface in the calculations, the particle number, energy and momentum are not conserved across the surface, but the error is small, about 2% for central collisions [18].

Because the tail obtained for the freeze-out surface in the Gubser case is far from reality, and because in the real case, the vertical part of the surface only
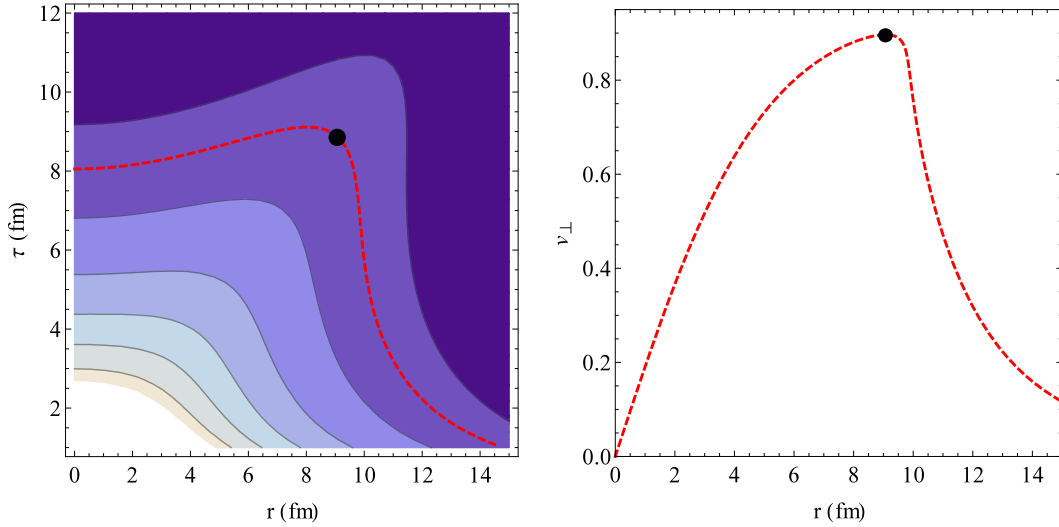
Figure 4.1: Temperature contour plot, with the freeze-out time profile (red dashed line) for the background SO(3) invariant flow (left). Transverse velocity profile for the SO(3)-invariant flow at freeze-out (right). The black disk on both plots indicates the position of the maximum of the transverse velocity at freeze-out. Isothermal freeze-out was considered, with $T_{fo} = 120$ MeV.

contributes a small part of the total number of particles, we will ignore the integration over r outside the point of maximal flow at $r = 9.07$ fm, indicated by a black disk in both plots in Figure (4.1).

4.2   An Initial Bump-like Perturbation

In this section we explore the effects that a local initial perturbation such as the one described in Section (3.5), has on the final particle distribution. The initial perturbation is a Gaussian that evolves in time to become an expanding circle until freeze-out time, when sound stops propagating, and the excess of energy density in the zones where the cirlce was last generate an excess in the freeze-out surface, and also of particles that is seen in the azimuthal particle distribution.

4.2.1   Freeze-out Surface and the Single Particle Distribution

The perturbations produce two different effects in the final particle distribution function: they modify the flow velocity, and they modify the freeze-out surface.

The first effect is simply the perturbed velocity added to the background flow,

$$u_\mu = u_{B\,\mu} + \delta u_\mu \,, \tag{4.32}$$

while the second effect is related to the perturbation to the temperature/energy density. For a hot spot, the deformation in the temperature profile is an excess in the temperature in a localized zone, compared to the background temperature in the same region. As we use the isothermal freeze-out prescription,

$$T_B(\tau, r) + \delta T(\tau, r, \phi) = T_{fo} \,, \tag{4.33}$$

the excess in temperature translates into an excess of time till freeze-out, so the perturbation to the temperature generates a deformation to the freeze-out surface,

$$\tau_{fo}(r, \phi) = \tau_B(r) + \delta\tau(r, \phi) \,, \tag{4.34}$$

such as the one shown in Figure (4.2) for a perturbation initially placed at $r = 4.1$ fm, in the ideal case. Because we work in the small perturbation
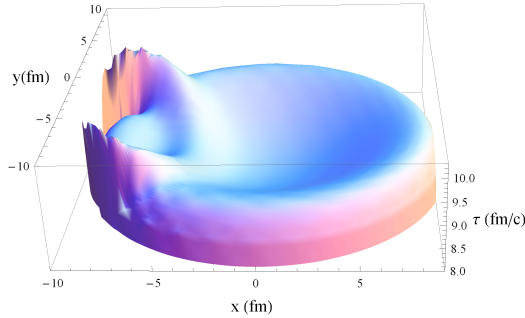
Figure 4.2: Freeze-out surface $\tau(x, y)$ produced by an initial Gaussian perturbation on top of the SO(3)-invariant flow in the inviscid case. Isothermal freeze-out was considered, with $T_{fo} = 120$ MeV.

approximation, we will only include terms up to first order in $\delta\tau(r, \phi)$, so the four-velocity in the exponent of the Cooper-Frye formula (4.1) will be approximated by

$$u_\mu = u_{B\,\mu}(\tau_B) + \delta u_\mu(\tau_B) + \delta u_{S\,\mu} \,, \tag{4.35}$$

where the first term comes just from the background, the second term is the perturbation to the velocity, and the third term is the modification to the

background velocity from the freeze-out surface

$$\delta u_{S\,\mu} = \frac{du_{B\,\mu}(\tau_B + \delta\tau)}{d(\delta\tau)}\bigg|_{\delta\tau=0}\delta\tau\,. \tag{4.36}$$

The perturbation to the freeze-out surface is plotted in Figure 4.3 for two cases: the ideal case, and a case with shear viscosity to entropy ratio $\eta/s = 0.134$. Both plots present a similar shape for the freeze-out deformation: the remains

Figure 4.3: Excess of freeze-out surface $\delta\tau(x,y)$. Ideal case (left) and visocus case with $\eta/s = 0.134$ (right) . Only the half of the surface that is affected by the perturbation is shown.
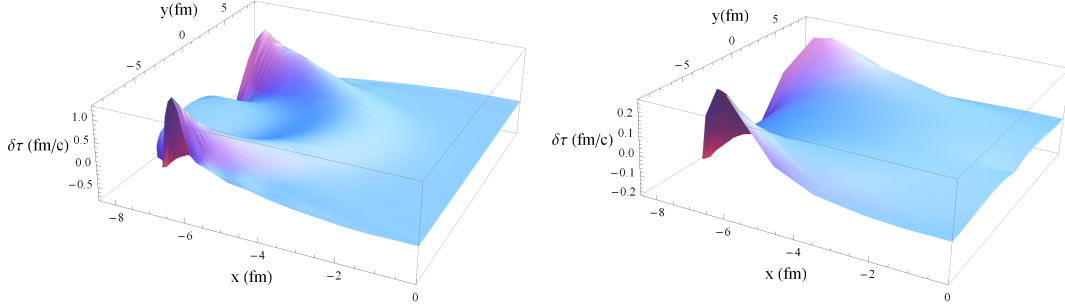
of the expanding sound circle meeting the edge of the fireball. The main difference between the two cases is the size of the deformation, that is much larger in the ideal case, but gets damped in the viscous case. It is also posible to see that when viscosity is included the peaks are wider than in the ideal case, and the shape in general is softer: all the changes are less abrupt. With all the ingredients required by the Cooper-Frye method–the momentum, the velocity, the temperature and the freeze-out surface–we estimate the particle distribution at freeze-out using the maximum of the exponent approximation. The results obtained for a perturbation initially located at $r = 4.1$ fm are presented in Figure (4.4), for the ideal case (top plot) and for the case when the shear viscosity to entropy ratio i s $\eta/s = 0.16$ (bottom plot). The different colors of the curves plotted represent different widths of the initial Gaussian perturbations: the magenta lines are for an initial width of 0.4 fm, while the blue lines are for a width of 1 fm. The magnitude of the latter ones is larger than the former because while we changed the width of the Gaussian, we did not vary its height, so when a larger width is used, the total energy of the perturbation is larger, and this translates into an increased number of particles at freeze-out.

Because we were mainly interested in studying the shapes of the final particle distribution functions, and on understanding the effects that viscosity
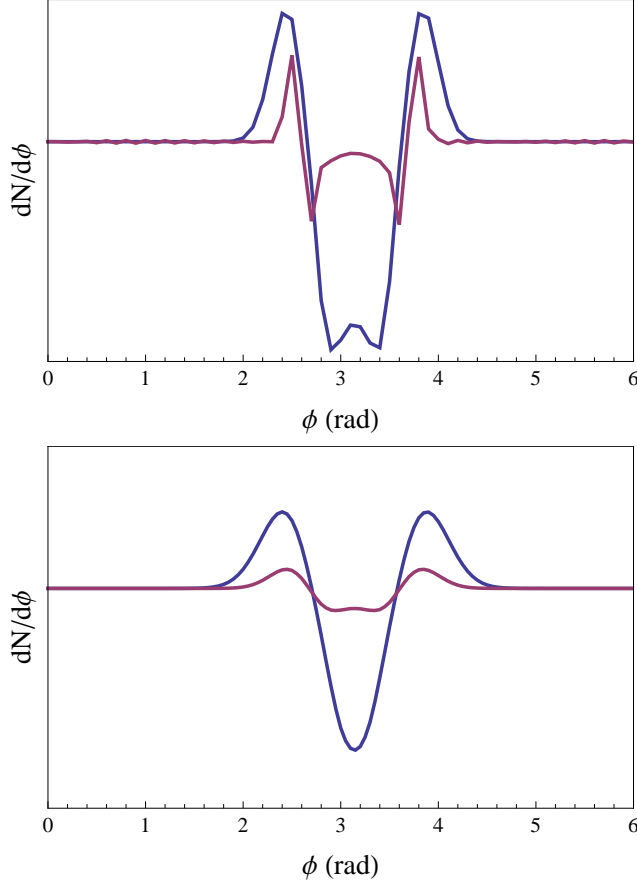
Figure 4.4: Single particle distribution (arbitratry units) for initial Gaussian with widths 0.4 fm (magenta) and 1 fm (blue), for the ideal case (top) and the case with viscosity to entropy ratio $\eta/s = 0.16$ (bottom).

and the width of the Gaussian have on the final result, we took a qualitative approach only. The principal features of the particle distribution are two horns with a dip in the middle, that are centered around the original azimuthal position of the perturbation. This characteristic shape is the remnant of the original expanding sound circle as it intersects the edge of the fireball. In the ideal case it is possible to see high frequency oscillations on the curve that are due to the arbitrary limit of the number of terms used ($l < l_{max} = 30$) in the expansion in spherical harmonics of the Gaussian. These oscillations disappear when we include viscosity, because as described in Section (3.4.3), given enough time, viscosity kills all harmonics with $l \gtrsim 10$. Other effects of viscosity are to dampen and broaden the peaks and smooth out the curves.

4.2.2 The two-Particle Correlations and the Power Spectrum

To calculate the two particle correlation we take the product of two single-particle distributions and perform the averaging over the random axial position of the initial perturbation,

$$\frac{dN}{d\left(\Delta\Phi\right)} \sim \int \frac{dN}{d\left(\Phi_1 - \psi\right)} \frac{dN}{d\left(\Phi_2 - \psi\right)} d\psi \,. \tag{4.37}$$

Because we work in perfectly central collisions, after taking the average, the original dependence of the two angles Φ_1 and Φ_2, becomes a dependence on only the azimuthal difference $\Delta\Phi = \Phi_1 - \Phi_2$. For non-central collisions the situation is more complicated because the direction of the impact parameter, which breaks the axial symmetry, must also be taken into account.

Our results for the two particle distributions for three different values of shear viscosity to entropy ratio are shown in Figure (4.5) together with a plot from ATLAS [24] for comparison. Note first their distinctive shape, with a larger peak centered at $\Delta\Phi = 0$, when both particles belong to the same maximum of the single particle distribution, and two smaller peaks around $\Delta\Phi = \pi$, when the two particles belong to two different peaks, connected by a flat region between them. This shape presents the general features, found in two particle correlations for central collisions measured in experiments (*e. g.* Figure (4.5)); however, there some differences that we proceed to discuss.

The first thing that one notices when comparing our calculated plots to the experimental data is that when there is no viscosity or the viscosity is small, there appears some extra structure in the two particle correlation: There are two smaller peaks at both sides of the large $\Delta\Phi = 0$ one. The additional peaks originate from the correlation between one of the peaks in the single particle distribution with the matter inside the circle, that is what is left of the original Gaussian. These extra peaks are attenuated when viscosity is used, and for $\eta/s = 0.134$ they have already disappeared. The extra structure also vanishes in the case when a larger width of the initial perturbation is used, because in this case, as well as in the cases with larger viscosity the matter between the two horns in the single particle distribution functions (see Figure (4.4)) is small or non-existent.

The characteristic two particle correlation with a large peak at $\Delta\Phi = 0$ and two smaller peaks joined by a plateau on the away side, were found by experiments at both RHIC and LHC, for central collisions of heavy ions. Together with the result from ATLAS presented in Figure (4.5), ALICE [60] has similar results for the same centrality $0\% - 1\%$, while the STAR collaboration
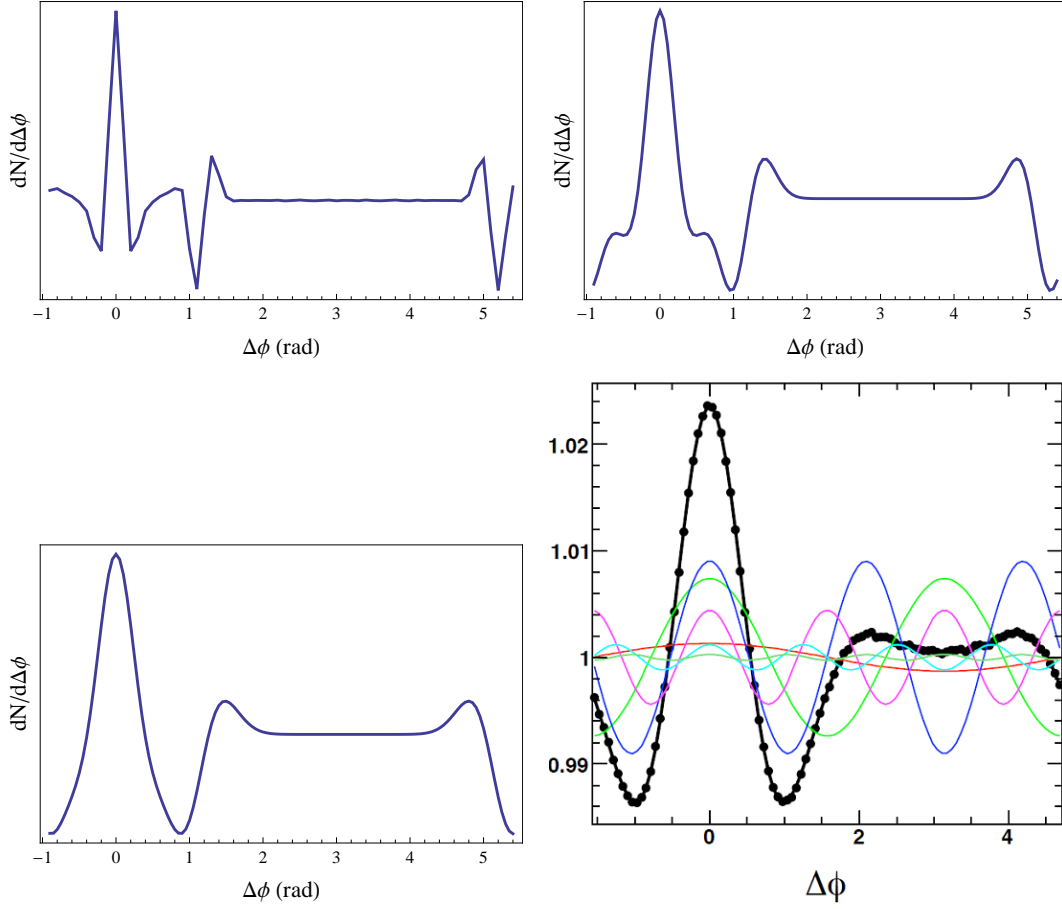
Figure 4.5: Two particle correlation, produced by a Gaussian perturbation on top of the SO(3)-invariant flow at initial time, as a function of the azimuthal angle difference $\Delta\Phi$ (rad). The top left plot was obtained in the ideal case, while the top right and the bottom left plots correspond to calculations including viscosity, with $\eta/s = 1/(4\pi)$ and $\eta/s = 0.134$, respectively. The bottom right plot, taken from [24] , was measured at LHC by the ATLAS collaboration for the most central $(0\% - 1\%)$ collisions.

[61] also measures the same structure for a wider centrality range $(0\% - 12\%)$. Comparing our calculated two-particle distributions to these data we find a great similarity between their shapes, especially for the higher shear viscosity to entropy ratio. The width of the main peak is correctly reproduced, provided the viscosity is correct. Also the double hump structure on the away side, with the correct shape of the plateau in between is found, but the length of the plateau, and thus the location of the two peaks on the away side is different. While in experiment the peaks are located at about $\Delta\Phi \sim \pm 2$ in our

calculations they are located closer to $\Delta\Phi \sim \pm 1.4$. This shift in the location of the peaks is because we keep the equation of state $\epsilon = 3p$ fixed through the whole evolution and thus the velocity of sound is also constant, and also the shape/size of the freeze-out surface is not quite realistic in our analytic approach.

Let us emphasize that this nontrivial shape comes from the hydrodynamical calculation itself, with the initial condition simply being a local hot spot. Sound propagates starting from the initial perturbation by a distance comparable to the fireball radius. The angular positions of the secondary peaks depend entirely on the ratio of the sound horizon to the size of the fireball (the speed of sound and the freeze-out time).

Now we turn to an equivalent description of the results from two particle correlations: the so-called power spectra for the two-particle correlation functions. It can be calculated from either the Fourier transform of the correlator as a function of $\Delta\Phi$, or from the modulus squared of the flow harmonics in the single particle spectrum v_n^2. In this last form the expansion of the two particle correlation function is

$$\frac{dN}{d\Delta\Phi} = 1 + 2\sum_m |v_m|^2 \cos\left(m\Delta\Phi\right), \qquad (4.38)$$

so it carries the same information as the flow coefficients, and thus the power spectrum of harmonics, in which the $|v_m|^2$ coefficients are plotted versus m. (Notice that these v_m are the coefficients of the Fourier expansion of the particle distribution and are not to be confused with the velocity coefficients $v_l(\rho)$ of the perturbation discussed in Chapter 3.) The main advantage of studying the power spectrum is that the behavior of all the harmonics, and in particular the existence of higher harmonics, becomes more visible compared to the two-particle correlation itself.

The results obtained for the spectral plot are presented in Figure (4.6) for four different values of viscosity to entropy ratio $\eta/s = 0$, 0.08, 0.134, 0.16 and for three different widths of the initial Gaussian perturbation $0.4, 0.7$ and 1 fm. For all cases the curves present maxima and minima, resembling the structure of the power spectrum of the angular harmonics of the CMB distribution over the sky such as the famous Figure 7 of Reference [62]. In both the Big and the Little Bang, the time allocated to the hydrodynamical stage of the evolution is limited by the so-called freeze-out time τ_{fo}, after which the collision rates in matter can no longer keep up with the system's expansion. At this time the propagation stops and each harmonic has at this moment a different phase of oscillation.

While the CMB measurements read the temperature perturbation $\delta(fo)$
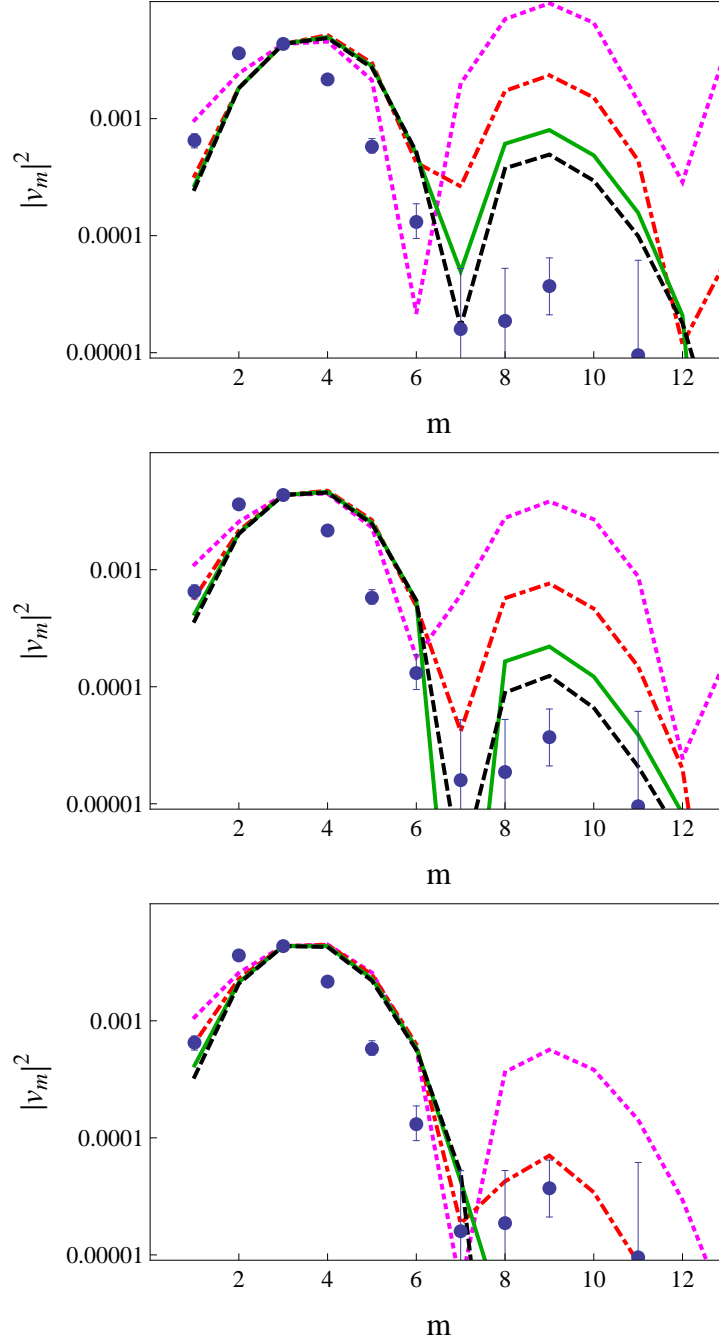
Figure 4.6: Spectral plots for three widths of the initial perturbation 0.4, 0.7 and 1 fm, from top to bottom. The magenta (small-dashed), the (red) dash-dotted, the (green) solid, and (black) dashed curves are for $\eta/s = 0, 0.08, 0.134, 0.16$, respectively. The data points are preliminary data from ATLAS reported at QM2011 and in [24]. Similar data (not shown here) have been reported by the PHENIX[63] and STAR[64] collaborations. All the curves are arbitrarily normalized to fit the third harmonic.)

directly from the sky, and thus the nodes of $\delta_l(fo)$ correspond to the minima, in the Little Bang one has to calculate the specific combination of the temperature and the flow perturbations. The nodes of this observable combination give rise to the accoustic minima and maxima, and as the figure shows, they are rather insensitive to many details such as dissipation.

The three plots in Figure (4.6) correspond to three different widths of the initial perturbation, 0.4, 0.7, and 1 fm, and they show that the values of the flow coefficients depend significantly on this parameter, especially for high harmonics. The larger the width of the initial perturbation, the smaller the height of the larger harmonics in the power spectrum. This can be explained by going back to the description of the original perturbation as a sum of spherical harmonics. In principle, to describe a function you need an infinite number of terms, and this is in fact true if you have a very thin Gaussian resembling a δ-function, but when the Gaussian is more spread out, the terms with higher values of l, m contribute less, and this is the effect that we are looking at in these three plots.

The different curves on each plot correspond to different viscosities (see caption), and they show the effect that this parameter has on the flow coefficients: it dampens higher harmonics. This is to be expected, as higher harmonics of the flow have higher gradients of the flow. One can also see from these figures that the fit to the viscosity value must be done together with the fit to the initial size, as they have an influence in the damping of the higher coefficients of the flow.

We do not attempt an actual fit here, because to do so, an accurate knowledge of the initial conditions, in particular of the with of the initial Gaussian, would be necessary. Such knowledge would include the size of the created hot-spot right after the collision and its evolution in the pre-hydrodynamical stage, where this size should grow. To define the particular value one needs to know the non-equilibrium physics at this stage.

One more comment on the plots in Figure (4.6) is perhaps in order: all the curves look shifted towards greater m-values than the data points– this is especially noticeable for $m = 4, ..., 6$. Larger m corresponds to smaller angular size of the sound circles. This happens because we have not fitted the freeze-out temperature and time τ_{fo} to these data: Decreasing the former and increasing the latter one can certainly get a better fit. We have not done so because our calculations were done for conformal matter with fixed speed of sound and ϵ/T^4, which can only give us an approximate idea of the evolution of the background and perturbation, but cannot accurately describe real collisions.

So far we have demonstrated some qualitative features of the one-body spectrum and two-body correlations resulting from a local perturbation, se-
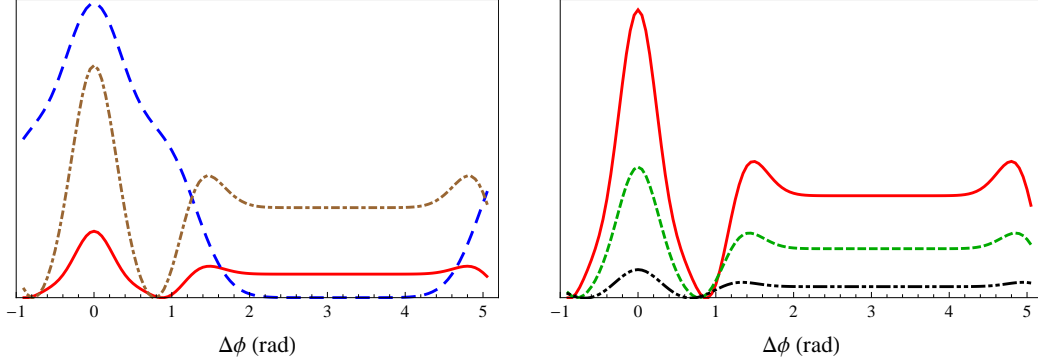
Figure 4.7: (Left) The two particle distribution in arbitrary units as a function of azimuthal angle difference $\Delta\Phi$ (rad), for $r = 2$ fm (blue long-dashed line), $r = 3$ fm (brown dash-dotted line), and $r = 4.1$ fm (red solid line). (Right) The two particle distribution in arbitrary units as a function of azimuthal angle difference $\Delta\Phi$ (rad), for $r = 4.1$ fm (red solid line), $r = 4.7$ fm (green short-dashed line), and $r = 5.5$ fm (black dashed double dotted line). All plots are from the same value of viscosity to entropy ration $\eta/s = 0.134$.

lecting one typical location. In principle, perturbations can be located at any position within the fireball, and now we provide further detail on the modifications to the two-particle correlations depending on the location of the hot spot. Because we only consider central collisions, by location we mean the radial position of the hot spot. As shown in Figure (4.7), changing the location of the spot visibly affects the shape of the two-particle correlation. When the spot is located near the center of the fireball, the two particle correlation presents only one peak located at $\Delta\Phi = 0$ and no structure on the away side. The characteristic two peaks appear when the initial perturbation is located not too close to the center ($r \sim 3 - 5$ fm), that is when the expanding sound circle has sufficient time to reach the edge of the fireball, such that two separate peaks appear in the single-particle correlation.

Furthermore, as one can see, the amplitude of the modulation decreases in this case. This happens not because of a change of the hot-spot amplitude (which is the same in all cases), but because of the (partial) cancellation between hydro perturbations for velocities of the first type (in the sound wave) and the second type (extra radial flow stemming from the modification of the freeze-out surface). As we have discovered, the very sign of the projection of the former on the radial direction depends on the position of the initial perturbation. For perturbations located near the center of the fireball it is positive, but as the hot spot gets located at larger r, it decreases, becoming negative until it gets as large as the second one and cancels it, when the hot spot is

located at the very edge of the fireball.

We find that the radial position of the initial perturbation affects the final two-particle correlation but that, for perturbations that are not too close to the center of the fireball initially, the final shape obtained is quite similar, with the length of flat region on the away side growing a bit as the initial location becomes more peripheral.

In real heavy ion collisions more than one hot spot may exist, and one may wonder if there will be an interaction between the different perturbations that would change the shape of the calculated two particle correlations. We argue that this is not the case, because in the linear approximation the sound waves would just pass each other without interfering, and there should be no correlation between the different signals. The case of an initial condition with more than one perturbation was studied by the Brazilian group [65], and they indeed found that the presence of numerous tubular structures (that they use to preserve the rapidity independence) did not alter the shape of the two-particle correlation found when compared with the results obtained for just one tube.

Chapter 5

Perturbations in the η-direction

In the previous chapters (2,3,4) we have discussed the origins of initial state fluctuations in the transverse plane and their effects to final particle distributions after the hydrodynamic evolution. Now, we focus on perturbations that are localized in the longitudinal direction, so the rapidity invariance of the perturbations that we used before is now lost.

5.1   QGP clusters

There are many sources of fluctuations in heavy ion collisions. Up to now, we have only described initial state fluctuations that perturb the smooth background of the QGP, and how these disturbances evolve hydrodynamically. Together with these fluctuations, there are also fluctuations that occur during the hydrodynamical expansion of the fireball, and that follow from the dissipation-fluctuation theorem, the theoretical grounds of which have been recently studied by Kapusta, Muller and Stephanov [66]. Also, it is expected that as the system expands and its temperature passes through the phase transition region $T \approx T_c$, from QGP to the hadronic phase, there will be enhanced critical fluctuations [67]. They are expected to be enhanced near the second-order critical point [68], and this idea motivated the current downward energy scan program at RHIC.

We propose a different strategy to search for critical fluctuations, by using the sound they emit. In a near-ideal fluid sound is the only long-lived propagating mode. The underlying assumption that we make is that the "acoustic" properties of the matter are there not only during the QGP era, but are maintained for the time period between the critical region $(T \approx T_c \approx 170\,MeV)$ and the final (kinetic) freeze-out $(T \approx 120\,MeV)$.

It is very likely that in the region near T_c an inhomogeneous intermediate

state will form, and that by its end, certain QGP clusters will remain.We propose that, instead of slowly evaporating, the QGP clusters undergo a Rayleigh-type collapse, transferring (part of) their energy/entropy into outgoing shocks/sounds. These "mini-Bangs", as we will call them, are the source of sound spheres, distorted by flow. They should be distinguishable from sounds caused by the initial state perturbations, because the latter ones originate at early times and are rapidity-independent, while the late-time "mini-Bangs" have sound waves propagating in the longitudinal (rapidity) direction as well as in the transverse plane.

These clusters produced around T_c are not the only sources of perturbations in the longitudinal direction, jets are dependent on rapidity as well. As the trigger p_t grows the contribution of the jet fragmentation also grows, and beyond say 10 GeV it becomes dominant. Whatever the model of jet quenching, it is clear that some fraction of the energy goes into the medium and thus jets must also induce a sound wave [69]. From a hydrodynamical point of view, these sounds are similar to those from the "mini-bangs", and differ only by the fact that jet quenching deposits energy along the light-like trajectory rather than at a particular space-time point.

5.2   Sound Propagation From the Cluster

The main idea in the work we now describe is that in the near-T_c region, after most of the QGP has transformed into hadronic matter, some clusters of QGP still remain, and that under the right conditions they will collapse releasing energy in the form of sound to the medium. The idea of the collapsing cluster was inspired in collapsing bubbles of air in water, in experiments of sonoluminescence (for a review of the subject see [70]). The change in the radius of the bubble is given by the Rayleigh-Plesset equation

$$\ddot{R}R + \frac{3}{2}\dot{R}^2 = \frac{1}{\rho}\left(p - 4\eta\frac{\dot{R}}{R}\right) , \qquad (5.1)$$

where $R(t)$ describes the radius of the bubble as a function of time, ρ is the density, p the pressure and η the shear viscosity. The solution to this equation shows the collapse of the radius, and details of the calculation and the solution can be found in Appendix A.

In what follows, we will only focus on the effects that the changing radius of the cluster has on the medium: When the radius of a cluster rapidly decreases, it produces spherical sound waves that expand and propagate through it. This effect is similar to what happens when a Gaussian perturbation is placed in the

medium: it too generates divergent sound waves. We will use this relation to look at the effect that the presence of clusters could have on the final particle distribution.

The propagating sound wave generated by the collapse of the QGP cluster propagates on an hadronic background, which of course has many differences with the QGP, one of them being the speed of sound. We however ignore this difference for the time being, in order to use the SO(3)-invariant flow described in Chapter 3. In this work we only aim to obtain a qualitative description of the propagating sounds, and the Gubser-Yarom framework provides very nice analytical tools to do so, as discussed in Chapters 3 and 4. There are now two differences with the previous study: (i) the perturbation is not defined at initial time, but at some "hadronization" surface; (ii) the perturbation will now depend on η as well as on θ and ϕ, and thus the temperature in the rescaled frame will take the form

$$\hat{T} = \frac{\hat{T}_0}{(\cosh \rho)^{2/3}} \left(1 + \sum_{klm} c_{klm} \delta_{kl}(\rho) Y_{lm}(\theta, \phi) e^{ik\eta} \right) , \qquad (5.2)$$

while the perturbations to the velocity, also in the rescaled frame, correspond to

$$\hat{u}_\theta = \sum_{klm} c_{klm} v_{kl}(\rho) \partial_\theta Y_{lm}(\theta, \phi) e^{ik\eta} , \qquad (5.3)$$

$$\hat{u}_\phi = \sum_{klm} c_{klm} v_{kl}(\rho) \partial_\phi Y_{lm}(\theta, \phi) e^{ik\eta} , \qquad (5.4)$$

$$\hat{u}_\eta = \sum_{klm} c_{klm} v_{kl}^\eta(\rho) Y_{lm}(\theta, \phi) e^{ik\eta} . \qquad (5.5)$$

The ρ-dependent functions now depend not only on l but also on k, and they can be computed from the sistem of three coupled differential equations described in [35]

$$\frac{d\boldsymbol{w}}{d\rho} = -\Gamma \boldsymbol{w}, \qquad \boldsymbol{w} = \begin{pmatrix} \delta_{kl} \\ v_{kl} \\ v_{kl}^\eta \end{pmatrix} \qquad (5.6)$$

with

$$\Gamma_{11} = \frac{H_0 \tanh^2\rho}{3\hat{T}_B} \tag{5.7}$$

$$\Gamma_{12} = \frac{l(l+1)\left(H_0\tanh\rho - \hat{T}_B\right)}{3\hat{T}_B \cosh^2\rho} \tag{5.8}$$

$$\Gamma_{13} = \frac{ik\left(2H_0\tanh\rho + \hat{T}_B\right)}{3\hat{T}_B} \tag{5.9}$$

$$\Gamma_{21} = 1 + \frac{2H_0\tanh\rho}{H_0\tanh\rho - 2\hat{T}_B} \tag{5.10}$$

$$\Gamma_{22} = \frac{8\hat{T}_B^2\tanh\rho + H_0\hat{T}_B\left(-4\left(3l(l+1)-10\right)(\cosh\rho)^{-2} - 9k^2 - 16\right) + 6H_0^2\tanh^3\rho}{6\hat{T}_B\left(H_0\tanh\rho - 2\hat{T}_B\right)} \tag{5.11}$$

$$\Gamma_{23} = \frac{iH_0k}{2H_0\tanh\rho - 2\hat{T}_B} \tag{5.12}$$

$$\Gamma_{31} = \frac{ik\left(3H_0\tanh\rho + \hat{T}_B\right)}{H_0\tanh\rho + \hat{T}_B} \tag{5.13}$$

$$\Gamma_{32} = \frac{il(l+1)kH_0}{4\cosh^2\rho\left(H_0\tanh\rho + \hat{T}_B\right)} \tag{5.14}$$

$$\Gamma_{33} = \frac{\hat{T}_B\left((9l(l+1)-4)H_0(\cosh\rho)^{-2} + 4H_0(3k^2+4) - 8\hat{T}_B\tanh\rho\right) + 12H_0^2\tanh^3\rho}{12\hat{T}_B\left(H_0\tanh\rho + \hat{T}_B\right)} \tag{5.15}$$

that is an extension of Eqn. (3.82) and (3.86) to include the perturbations in η. Once the solution to this system of equations is found, the c_{klm} coefficients need to be calculated for the chosen Gaussian that will generate the expanding sound wave. The only thing needed now to start studying the sound originating from the perturbation is its location and the time when it appears.

We expect the QGP clusters to appear when the temperature reaches the critical value ~ 175 MeV, this means that they should be placed on the isotherm $T = T_c$ that corresponds to the dashed magenta curve in Figure (5.1). Having specified the surface on top of which the clusters can appear, we just need to select a spatial location for them.

The transverse momenta of the final particles in the region we are interested
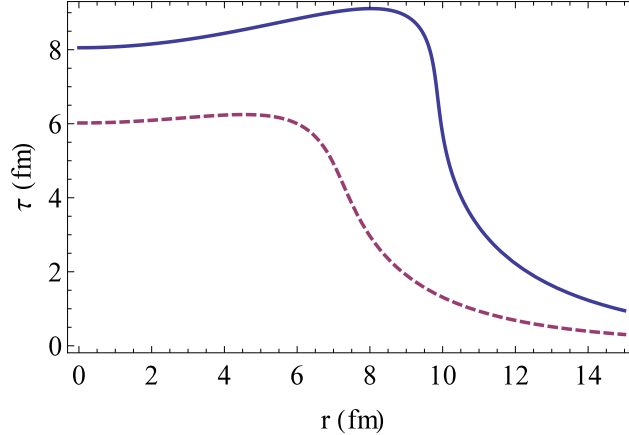
Figure 5.1: Isothermal surfaces for $T_c = 175$ MeV (blue solid line) and $T_{fo} = 120$ MeV (magenta dashed line). The sound emission from near-T_c phenomena is expected at the former surface, and its propagation ends on the latter one.

in studying– say 1.2 to 2.4 GeV, which is well described by hydrodynamics – exceed the freeze out temperature $T_f \approx 120 \, MeV$ by a large factor ranging from 10 to 20. If those particles were produced by the pure tail of the thermodynamic Boltzmann factor, its probability would be truly negligible. But the hydrodynamical expansion makes a big difference: in the moving fluid the exponent is not the energy in the lab frame but in the frame co-moving with the fluid, $p^\mu u_\mu$, which is smaller than the momentum itself by the so called "blue shift factor"

$$\frac{p^\mu u_\mu}{T_f} \approx \frac{p_T}{T_f} \sqrt{\frac{1 - v_\perp}{1 + v_\perp}} . \tag{5.16}$$

It depends on the local transverse flow velocity $v_\perp$, that varies over the surface Σ, with a maximum near the edge. The transverse flow velocity reaches at LHC $v_\perp \sim 0.8c$, for which this factor is $\sim 1/3$, reducing the quantity in Boltzmann's exponent to only $\sim 3..7$. It is much smaller than p_t/T_f, but still can be considered a large parameter. This blue shift narrows the contribution from the surface integral to the particle spectra to a relatively small vicinity of the radial position $r = r_*$ where r_* is the location of the *maximal transverse flow*. Furthermore, assuming for simplicity zero impact parameter (central collisions) and rapidity independence of the system, we conclude that at such p_t the observed particles come from the "freeze-out cylinder", with radius $r = r^*$, depicted in Figure (5.2). The large transverse flow strongly enhances
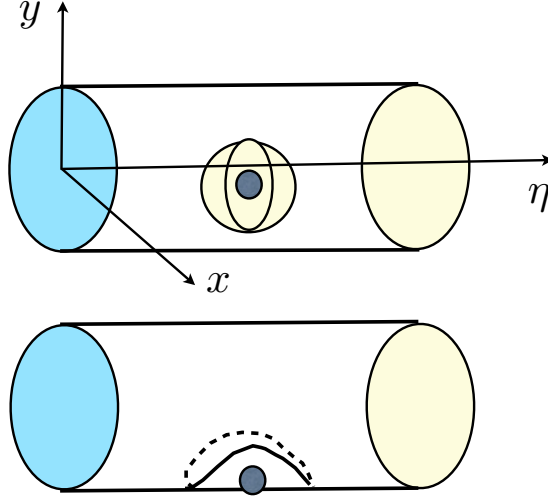
71

Figure 5.2: The schematic representation of the freeze-out cylinder and a sound perturbation, for "internal" (upper picture) and "peripheral" (lower picture) sources. In the latter case we show the intersection of the sound sphere and the freeze-out cylinder.

the contribution of this cylinder, basically projecting it onto the detector.

Sound perturbations, propagating on top of the background flow form distorted sound spheres around the origination point. These perturbations fall into two classes: (a) the ones with sound spheres that never reach the maximum flow region on the freeze-out surface, or "internal" ones, and (b) the ones with sound spheres that cross the freeze-out cylinder, or "peripheral' ones', see Figure (5.2). For the reasons discussed in the previous paragraph the latter perturbations should be dominant over the former, as they benefit maximally from the blue-shift effect. Thus we come to conclusion that clusters located not too far from cylinder of radius $r = r*$ are the only ones that can can be observed.

The distance from the edge of the cylinder at which the cluster must be placed in order to be detected is determined by the distance the sound can travel between its emission point and the final freeze out moment. Thus the corresponding perturbation should be located approximately at a "sound sphere" of radius $R_s = c_s(\tau_f - \tau_{emission})$ from the edge, as shown schematically in Figure (5.2)(b). As one can see from Figure(5.1), the time difference between the surface of critical temperature and the freeze-out surface is about $2\,fm/c$ for $r_{emission} < 6\,fm$, but grows to 6 fm/c at $r_{emission} \approx 8\,fm$. So, the
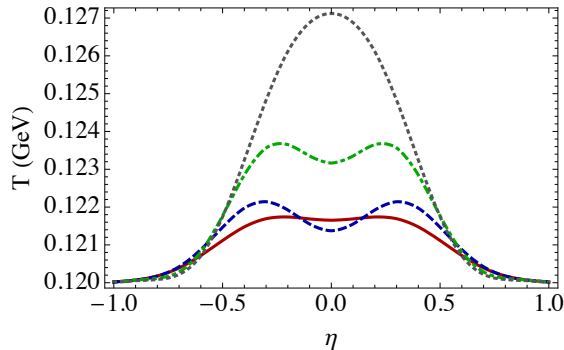
Figure 5.3: Temperature at the (zeroth order) freeze-out as a function of spatial rapidity η, for a perturbation placed at $r = 6$ on the isothermal $T = T_c$. The four different curves correspond to different cuts in the transverse plane coordinates $x = 6, 7, 8, 8.3 fm, y = 0\ fm$, (red, blue, green, gray, respectively).

nearer to the edge the cluster is, the greater time the perturbation will have to travel. Repeating the same argument as above, we expect that the observable effect is basically a projection of the intersection of the sound sphere and the freeze-out cylinder, where both the perturbation and blue-shift are maximal.

To get some signal from the perturbation, we placed it close to the edge ($r \sim 6$) of the expanding matter at the time when the medium reaches the critical temperature, and let it evolve until the system reaches freeze-out. A sample of results for the temperature perturbation is presented in Figure (5.3), corresponding to different cuts through the "sound sphere". One can see that at appropriate positions a double-peak structure in the longitudinal coordinate – represented by a spatial rapidity η – emerges, substituted by a single peak centered at the cluster rapidity (gray dotted line) when looking at the very edge of the fireball.

5.3   Particle spectra and correlations

To calculate the final particle distributions we used the Cooper-Frye method discussed in Section 4.1, implementing an approximate isothermal freeze-out prescription, taking as freeze-out surface the surface obtained by setting $T_{Back}(\tau, r) = T_{fo}$ (solid curve in Figure 5.1).

The integrals over r and η in (4.1) are computed using Mathematica's numerical integration, while we approximated the integral over ϕ by using the
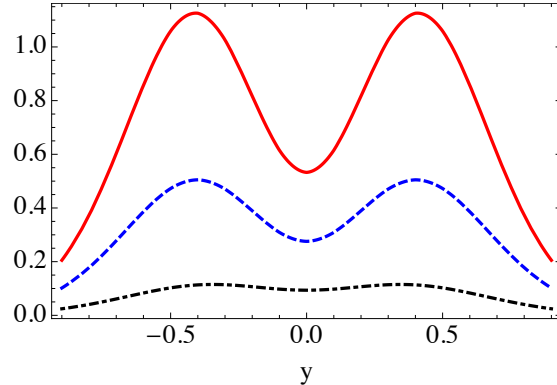
Figure 5.4: Single particle distribution as a function of rapidity y, for azimuthal angle Φ=0, 0.3, 0.6 (red,blue, black) counted from the cluster location, for $p_T = 1.5$ GeV. The original perturbation was placed at $r = 6$ fm.

saddle point method $\phi = \Phi$. The pseudorapidity integral was evaluated in the range $|\eta| < 5$, while the integral over r was calculated from $r = 0$ to $r = r^*$, where r^* is the value of the radius at which the background $v_\perp$ on the freeze-out surface reaches its maximum. A sample of the results is shown in Figure5.4 for pions at $p_\perp = 1.5$ Gev: here one can also find the characteristic double-peak shapes.

Here however comes the difficulty: in the theoretical calculation we may calculate all the distributions knowing the location of the original cluster. In particular, in Figure (5.4) the angle is counted from the cluster location. In experiment the location of the clusters in azimuth and rapidity ϕ_c, y_c is unknown, and thus we can only observe correlators, that are integrated over it. To reconstruct the original single-body distributions starting from the correlation functions of more than one particle is not a trivial task, as there does not exist a unique single particle distribution for every two particle correlation.

5.3.1 From the Single Particle Distribution to the Many-particle Correlation: a Simple Example

In principle, to determine the single particle distribution, an experiment should be able to measure a sample of n-body correlation functions. In the case of

correlations in rapidity, the many-particle correlations can be written as

$$\frac{dN}{dy_1 \ldots dy_n} = \int dy_c P(y_c) \prod_{i=1..n} f(y_i - y_c) \,, \tag{5.17}$$

where $P(y_c)$ is the probability to have a cluster at rapidity y_c, and $f(y_i - y_c)$ is the single particle distribution function produced by a cluster located at rapidity y_c, like, for example, the two-peak function presented in Figure (5.4).

As rapidity distributions are usually rather rapidity-independent, the probability of a cluster being at a given location $P(y_c)$ can be approximated by a constant. In this case, the n-body distribution depends only on rapidity differences–for two-particle correlations the dependence is only on $\Delta y = y_1 - y_2$. It is convenient to define Fourier transform of the single-particle distribution

$$\tilde{f}(k) = \int dy e^{iky} f(y) \,, \tag{5.18}$$

and rewrite the Fourier transform of the n-body spectrum in the form

$$\frac{d\tilde{N}}{dk_1 \ldots dk_n} = 2\pi\delta\left(\sum_{i=1..n} k_i\right) \prod_{i=1..n} \tilde{f}(k) \,, \tag{5.19}$$

where the delta function stems from the integral over the unknown cluster rapidity y_c, and results in the conservation of the momentum associated to rapidity–a consequence of the existence of translation invariance in this coordinate. A very special case is the two-body one, in which only one momentum remains since $k_2 = -k_1 = k$, and one can rewrite Equation (5.19) as the power spectrum

$$\frac{d\tilde{N}}{dk} \sim |\tilde{f}(k)|^2 \,, \tag{5.20}$$

that contains the square modulus of the harmonic amplitudes, but not the phase.

As a particular toy model, let's consider the $f(y)$ of a double-peaked shape, as the one we found for certain kinematic window and initial radial position of the cluster. If we describe the two peaks by the simple expression

$$f(y) = \frac{1}{2}(\delta(y - a) + \delta(y + a)) \,, \tag{5.21}$$

one finds the Fourier transform to be $\tilde{f}(k) = \cos ka$, such that the power

spectrum is given by

$$|\tilde{f}(k)|^2 = \frac{1}{4}(e^{2ika} + e^{-2ika} + 2)\,. \tag{5.22}$$

By taking the backwards Fourier transform of the power spectrum one finds the 2-particle correlation function: the three terms in this expression produce three peaks, two at $\Delta y = \pm 2a$ and one with an amplitude twice the one of the others located at $\Delta y = 0$.

This issue and expressions are close analogs of formulae which have been derived in the theory of correlators as a function of the azimuthal angle. In particular, a three-peak structure of the kind emerged from hydrodynamical calculations in our work as described in Chapter 4. Indeed, for central collisions the axial symmetry of the background flow, results in angular momentum zero for the observable harmonics of the many-body correlators.

As a side remark, we point out that while the experimental two-body correlator does indeed have the predicted shape with three maxima, that does *not* uniquely prove that the original spectrum has the predicted two-peaked shape. For example, various harmonics may have random phases, which are not observable in the power spectrum. For flow harmonics this remains unresolved, and further studies of many-body correlators could help elucidate this issue.

Given the single-particle perturbation function $f(y)$, all multi particle ones can be calculated, e.g. from the (approximate) relations above. We however cannot offer any straightforward inverse procedure, deriving $f(y)$ from measured correlators: comparing the calculated predictions with the measurements seems to be the only way. Since there are many multi body correlation functions, one should be able eventually get to convinced that the $f(y)$'s have certain shape, such as *e. g.* the one coming from the projected sound sphere.

5.3.2 Two-particle Correlation: Results

Let us now return to joint two-particle distributions, both in rapidity and angle

$$\frac{dN}{d\Delta\Phi d\Delta y} = \int \frac{dN}{d(y_1 - y_c)d(\Phi_1 - \psi_c)} \frac{dN}{d(y_2 - y_c)d(\Phi_2 - \psi_c)} d\psi dy\,, \tag{5.23}$$

where y_c and ψ_c represent the rapidity and azimuthal location of the cluster respectively. Unfortunately, as one can see from Figure (5.1), the time for sound propagation under consideration is rather limited to about 2 fm, except in the improbable case of a cluster at very large $r > 6\,fm$. Thus the sound-
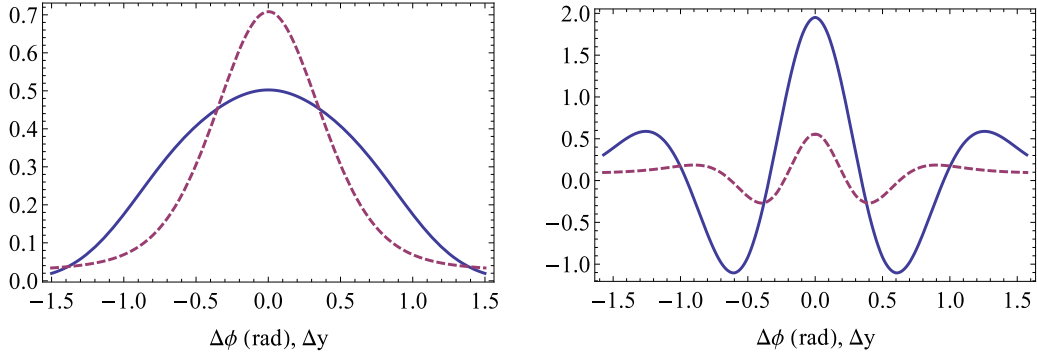
Figure 5.5: Two particle correlation functions for a cluster located initially at: (Left) $r = 6$ fm, and (Right) $r = 6.5$ fm. The solid (blue) curve corresponds to the correlation in $\Delta\eta$ with $|\Delta\Phi| < 0.87$, and the dashed (magenta) curve corresponds to the correlation in $\Delta\Phi$ with $|\Delta\eta| < 0.8$. In both cases the single particle distribution functions had been normalized such that their integral was 1.

induced peaks in rapidity are only shifted by about $\pm 1/2$ unit of rapidity, as the single-particle distribution in Figure (5.4) shows, which in most kinematics is not enough to see the peaks in the observable correlators.

We study the case with asymmetric kinematics, in which the trigger is a higher momentum particle and serves to determine the cluster location, while the associate particles have smaller $p_\perp$, and are sensitive to the double-hump region of the fireball. We calculate the two particle correlation with one particle with $p_\perp = 1.5$ GeV and one with $p_T = 2.5$ GeV. We integrate over $\Delta\phi$ in the range $|\Delta\phi| < 0.87$, to obtain the particle correlations projected in $\Delta\eta$, and integrate over $|\Delta\eta| < 0.8$, to generate the two particle correlation projected in $\Delta\Phi$. We present the results in Figure (5.5) for two initial locations of the perturbation, at $r = 6$ fm and $r = 6.5$ fm. The correlations obtained are very different, because the time that the sound circle had to propagate depends on the initial location of the perturbation.

The shape of the particle distributions, and the two-particle correlations shown in Figure (5.5) vary greatly, depending on the initial radial position of the perturbation. For a perturbation located initially at $r = 6$ fm one finds a two-particle correlation in $\Delta\eta$ with only one peak, while for that at $r = 6.5$ fm there are three peaks very well defined. The difference happens, because for the different sound origination points, the evolution will be longer at some places and shorter at others. Furthermore, to produce a noticeable effect the perturbation must be placed near the edge of the fireball—if it is located close to the center the sound circles will not reach the edge.
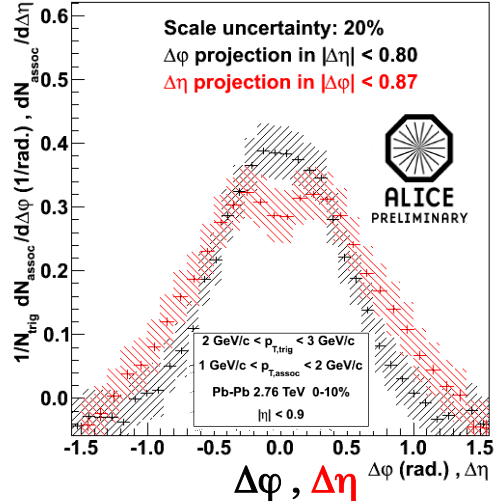
Figure 5.6: Correlation functions of two charged hadrons in the kinematic range defined in the figure, as a function of pseudorapidity and azimuthal angle differences between the two particles, taken from [72].

5.3.3 Phenomenology

Experiments at RHIC have not focused so much on rapidity correlations. We have only Phobos collaboration data [71], which used their large rapidity coverage due to the silicon detector. These data display rather strong modifications of the two-particle correlators in AA, relative to pp. The analysis of that data using some version of a cluster model has been reported in [71], and it showed that the charged multiplicity per cluster in AuAu collisions is significantly larger that what is seen pp collisions, up to $\langle N_{ch} \rangle \sim 6$ charged particles (or up to 10 including neutrals). Furthermore, the produced clusters do not decay isotropically but are instead more extended in (pseudo)rapidity. The width of the cluster decay changes from about 0.8 in pp to about 1.4 at mid-central collisions, a quite substantial broadening.

The first LHC data on two-particle pseudorapidity correlations provided further puzzles. As seen in Figure (5.6) (from ALICE collaboration [72]), the observed correlator presents variations from a Gaussian shape: the top of the curve is flat, with a double hump structure.

We propose the idea that the increased width in rapidity and the modified shape are caused by the sound waves emitted by the decaying clusters. Our calculations above produced a variety of shapes of the two-particle correlators, from near-Gaussian to three-peak ones, but we did not reproduce the two peaked shape form ALICE.

Before we argued that known examples of cluster collapse lead to efficient (nearly complete) transfer of its stored energy into the shocks/sounds, but in practice the efficiency of this process is hard to evaluate, and some smaller cluster may remain after partially collapsing. If one assumes a two-component model of the particle source, in which certain number of secondaries, proportional to a parameter A, originate from the QGP cluster itself, while a number proportional to a parameter B come from the sound emitted from its collapse, the two-particle correlator, projected on the rapidity difference Δy, can be written in a form containing three terms

$$\frac{dN_{corr}}{d\Delta y} = A^2 f_{cc}(\Delta y) + AB f_{cs}(\Delta y) + B^2 f_{ss}(\Delta y) \tag{5.24}$$

The first term stands for both secondaries coming from the cluster decay: as it is expected to decay isotropically the function $f_{cc}(\Delta y)$ is the same near-Gaussian distribution as is well known for the two-body resonance decays. The second term has a trigger coming from the cluster, fixing its rapidity, and the second from the sound: we expect the function $f_{cs}(\Delta y)$ to show the double peaked shape originating from the sound single particle distribution. The third term $\sim B^2$ is the convolution of the two single-particle ones just specified, averaged over the unobserved rapidity of the cluster, that was calculated in the preceding section for some particular cases.

With our calculations we did not obtain the expected two-peaked structure in the rapidity correlation, however more studies exploring different conditions for the perturbation (*e. g.* different widths, and locations) are needed to determine if the sounds from the QCD phase transition can be "heard".

Chapter 6

Summary

The final particle correlations measured by different experiments studying the collision of heavy ions present some characteristic features that depend on the azimuthal angular difference between the particles, but not on the difference in rapidity. In two-particle correlations, for example, the data show very defined correlations in $\Delta\Phi$, that are elongated in $\Delta\eta$. This independence on the longitudinal direction implies that the origin of these features is in the initial conditions of the matter created in the collision. The idea is that because the collision occurs at zero rapidity, and the created matter then expands longitudinally, the transverse distribution created at the initial time expands in the longitudinal direction, thus generating the rapidity independence of the measured correlations.

We studied fluctuating initial conditions using the Glauber Monte Carlo method, and found that the participant anisotropy coefficients–the anisotropy coefficients calculated in the center of mass of the participant or wounded nucleons–are non-zero for all the centrality ranges. For very central collisions, all the anisotropy coefficients were found to originate from fluctuations, and, excepting ϵ_1, to be of similar magnitudes, of the order $\epsilon_n \sim 0.1$. The case of the dipole asymmetry, when $n = 1$, is a little different from the others, because in the center of mass of the wounded nucleons the average $< x >$ and $< y >$ are zero, so the true dipole is also zero, and the calculated ϵ_1 is about 0.05. This result indicates that before the hydrodynamic evolution at least the first six harmonics have similar values, and in principle there is no reason to single out just the triangularity ϵ_3, over the other terms in the expansion.

For more peripheral collisions, the most important anisotropy coefficient is the ellipticity ϵ_2, because the almond-like shape of the overlap region contributes to make this deformation more sizeable. The other terms in the expansion are by no means negligible, but they still exist because of fluctuations: the variance of the anisotropy coefficients has approximately the same value

as the coefficients themselves, except in the $n = 2$ case.

In this description, to each anisotropy parameter there is an associated angle ψ_n, that indicates the direction of the major axis of the distribution, and that can be related to the angle that describes the direction of greater flow during the hydrodynamic expansion. We calculated the distribution of these angles for collisions in the centrality range determined by $100 < N_{\text{part}} < 300$, and found that the distributions for n even, are very well defined, and that they show an alignment with the y axis: that is, the major axis of the distribution defined by ϵ_n and ψ_n is in the direction of the tips of the almond-like overlap region in the case with even values of the integer n.

The situation for the distribution of the ψ_n angle is somewhat different in the cases when n takes odd values. The ψ_1-distribution is also correlated (though only weakly) with the direction of the tips of the almond, but ψ_3 and ψ_5 present a completely flat distribution. Further study of these quantities showed that while the ψ_n with odd n are not correlated to the mayor axis of the elliptic distribution, they do present non-trivial correlations among themselves. For example, one of the cases we studied indicated that the condition $3\psi_3 - \psi_1 = \pi$ is satisfied for many of the events.

Two-particle correlations in central collisions show no dependence on the phases ψ_n (or ψ_n^F); however, this is not the case for three- or more-particle correlations, nor for two-particle correlations in the non-central case. These latter correlators depend on the phases, in particular for three particles the important phase is the combination $n_1\psi_{n_1} + n_2\psi_{n_2} + n_3\psi_{n_3}$, where the integers must satisfy the triangular condition $n_1 + n_2 + n_3 = 0$.

We understood the non-trivial correlation of the phases of the deformations to be caused by the presence of hot/cold spots in the initial matter distribution, so we proceeded to investigate what the evolution of such a hot spot would be, and its effect on the final particle distribution. To study the hydrodynamic evolution of the fireball and its perturbations, we used an analytic solution called the SO(3)-invariant flow, an extension to Bjorken's flow that includes radial flow. We placed an initial Gaussian perturbation on top of the background fireball, and let it evolve. The original Gaussian propagated from its center as an expanding circle, and by freeze-out it had reached the edge of the expanding matter, contributing two peaks to the freeze-out surface and to the single particle distribution.

We studied the two-particle correlations and the flow coefficients for different widths of the initial Gaussian perturbation, and for different viscosities. For the appropriate values of viscosity and/or widths of the perturbation, we found that the shape of the two-particle correlation produced by just one initial Gaussian perturbation agrees quite well with the data, presenting one large

peak located at $\Delta\Phi = 0$ and two smaller peaks connected by a flat region on the away side.

We also studied the power spectrum of the flow coefficients that, even though carries the same information as the two particle correlation, allows for a better understanding of the higher harmonics of the flow. We found these plots to present a shape with maxima and minima that reminded us of the power spectrum of the angular harmonics of the cosmic microwave background radiation. The effect that the presence of viscosity has on the spectra is to decrease the contribution from the higher harmonics of the flow: the greater the viscosity, the smaller the higher harmonics become. This relationship could in principle be used to determine the value of the shear viscosity to entropy ratio η/s; however, our ignorance about the initial conditions prevents us from doing this. The problem is that the width of the initial Gaussian perturbation has the same effect that viscosity has: it damps the higher harmonics, so without an a priori knowledge of the initial conditions it is not possible for us to fix the viscosity.

It is necessary to mention that we have worked in a very idealized situation. The SO(3)-invariant flow that we have used to describe the hydrodynamic evolution of the fireball, is only useful to study perfectly central collisions when the matter being considered is conformally invariant. While this might be true for the QGP phase, it is certainly not so for the hadron gas, but we kept the evolution going even after the chemical freeze-out had occurred. The difference between the conformal and non-conformal regimes is in the equation of state, and because of this, also in the speed of sound. Different values for the speed of sound would certainly affect our results, but the difference would be not in the general features that we were able to reproduce, but in details such as the exact separation between the two peaks in the single-particle distribution, or the length of the flat region in the away side of two-particle correlations.

Even though, as we have said, the description obtained by using the SO(3)-invariant flow is not perfectly accurate, and many assumptions must be done, it is an analytical tool very useful for describing the general picture of what happens to the fireball and to its perturbations. Encouraged by our successful results in studying perturbations in the transverse plane, we decided to study also perturbations in the longitudinal direction. These are not initial time perturbations, they appear when the matter is near the critical temperature, as clusters of remnant QGP in a hadron gas medium. The idea is that as the pressure of the background becomes higher than the one of the clusters, they suffer a Rayleigh-type collapse, generating an expanding sound wave. Because placing a Gaussian perturbation on the background produces the same effect, we put one near the edge of the fireball on the isotherm $T = T_c$, and allowed

it to evolve. We found that the resulting two-particle correlations obtained following this procedure vary greatly depending on the radial location, because due to the shape of the isotherm the time that the perturbation has to evolve changes drastically for perturbations initially located at $r < 6$ fm and $r > 6$ fm. We suggest that measured correlations in rapidity may originate from this phenomenon, especially in the case with one of the particles coming from the not completely collapsed cluster, and the other one from the perturbation due to the sound circle. Again we must emphasize that the results obtained are only qualitative, because we are using a conformal solution, in principle valid only during the QGP phase, to describe the evolution of the hadron gas, so the true effects of critical perturbations may differ from the calculated ones.

Appendix A

A Drop's Collapse

A.1 The Rayleigh collapse

This appendix contains well known material worked out by people who study sonoluminescence, for a review see *e. g.* [70], that is given for self-consistency. All of the calculations are non-relativistic, so they are only presented here to give an idea of how a collapsing bubble behaves.

The equation that describes the radius of the bubble as a function of time may be derived starting from Euler's hydrodynamic equations

$$
\begin{aligned}
\rho[\partial_t \boldsymbol{u} + (\boldsymbol{u}\boldsymbol{\nabla})\boldsymbol{u}] &= -\boldsymbol{\nabla}p\,, \\
\partial_t \rho + \boldsymbol{\nabla}(\rho\boldsymbol{u}) &= 0\,.
\end{aligned}
\tag{A.1}
$$

The flow is assumed to preserve spherical symmetry, and the flow potential is defined by

$$
\boldsymbol{u} = \boldsymbol{\nabla}\phi(r,t)\,.
\tag{A.2}
$$

Then, one finds that Euler's equations become

$$
\rho\left(\partial_t\phi + \frac{1}{2}(\partial_r\phi)^2\right) = -p\,.
\tag{A.3}
$$

$$
\partial_t\rho + \partial_r\phi\partial_r\rho + \rho\nabla^2\phi = 0
\tag{A.4}
$$

Combining the two equations and using $dp/d\rho = c^2, dh = dp/\rho$ where h is the enhtalpy, and c is the sound velocity (the speed of light in our units is 1), one obtains a single equation for the flow potential

$$
\boldsymbol{\nabla}^2\phi - \frac{1}{c^2}\partial_t^2\phi = \frac{u}{c^2}(\partial_t u - \partial_r h)\,.
\tag{A.5}
$$

Now comes the crucial step: if all flows are slow compared to c, the Laplacian term is the dominant one. It then provides a simple Coulomb-like solution to the potential

$$\phi \sim f_1(t)\frac{1}{r} + f_2(t)\,, \qquad (A.6)$$

as a function of r. The two time dependent functions should be matched to the boundary conditions of the problem. One of them is at the bubble wall located at some $R(t)$: the condition matches the flow velocity with the wall speed

$$u_r = \partial_r\phi = \dot{R}\,, \qquad (A.7)$$

where the dot denotes the time derivative. This condition fixes one of the functions in the solution

$$\phi = -\frac{\dot{R}R^2}{r} + f_2(t)\,, \qquad (A.8)$$

and putting it back into Euler equation in the form (A.3) one finds, taking it at $r = R$, the ordinary differential equation for $R(t)$

$$\ddot{R}R + (2 - 1/2)\dot{R}^2 = \frac{p(r \to \infty, t)}{\rho}\,, \qquad (A.9)$$

where the $(1/2)$ comes from the second term of (A.3) and the r.h.s. is the effective pressure far from the bubble.

If the r.h.s. is positive, the system is stable, but as it crosses into the negative a collapse takes place. What was discovered by Lord Rayleigh is that even if the r.h.s. is put to zero, the equation admits a simple analytic solution (known as the original Rayleigh collapse solution)

$$R(t) \sim (t_* - t)^{2/5}\,. \qquad (A.10)$$

While the time-dependent singularity has a positive power, it is less than one, and thus produces an *infinite velocity*

$$\dot{R} \sim (t_* - t)^{-3/5}\,, \qquad (A.11)$$

at $t = t_*$. Needless to say, large velocity is incompatible with the approximation of small $u \ll c$ made above: therefore the near-collapse stage should be treated separately and more accurately (see below).
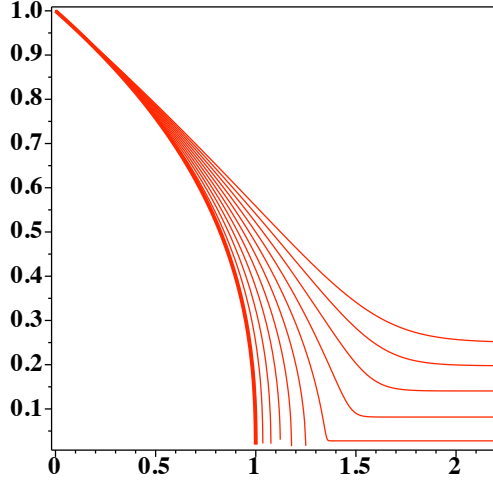
Figure A.1: The time evolution of the drop radius $R(t)$, for the values of $\eta/\rho = 0.01..0.1$ with a 0.01 step.

A comprehensive review [70] on sonoluminiscence includes both the theoretical and the phenomenological discussion of the shock waves produced by the collapsing air bubbles in water, under the influence of small-amplitude sounds driving an effective pressure to negative at each sound cycle. The reader interested in details can find it in this review: let us only mention that the observed shocks from collapsing bubbles have velocities of about 4 km/c, few times the speed of sound in water $c = 1.4$ km/s, suggesting the pressure in the collapse reaching a range as high as 40-60 kbar. Those values also imply a reduction of the bubble's volume by a huge factor $\sim 10^6$. Emission of light, indicating very high temperatures $T \sim 1\,eV \gg T_{r\to\infty}$, gave the name of *sonoluminiscence* to the whole phenomenon. One last comment is that these experiments found a rather high efficiency $\sim O(1/2)$ of the energy transferred into the shocks/sounds.

A.2   The collapse with the viscosity and sound radiation

The r.h.s. of the equation for the $R(t)$ can include a number of extra terms. The most obvious of them is the bulk pressure, which drives the collapse. The next is the surface tension, preventing collapse of too small bubbles because its role grows as $1/R$ at small R. Ignoring those terms for now, we focus on the dissipative effect of the flow due to viscosity. With the standard Navier-Stokes

term on the r.h.s. Equation (A.9) becomes

$$\ddot{R}R + \frac{3}{2}\dot{R}^2 = -\frac{4\eta\dot{R}}{\rho R} \, . \tag{A.12}$$

Solving this equation with variable value of the viscosity we found its critical magnitude capable to turn the catastrophic Rayleigh collapse into a "soft landing". In Fig. (A.2) we show a set of solutions with increasing values of $\eta * T/\rho$, showing how the collapse can be stopped by viscosity. The value of the ratio $\eta * T/\rho > 0.6$ is needed for this to happen. For smaller values it goes into the Rayleigh singularity, which simply stops our numerical solver (we use default one on Maple 16).

The second effect we study is the sound radiation. For a spherical source with a time-dependent volume $V(t) = (4\pi/3)R(t)^3$ the outgoing wave solution at large distances is (see hydrodynamics textbooks such as [54])

$$\phi = -\frac{\dot{V}(t - r/c)}{4\pi r} \, , \tag{A.13}$$

corresponding to the flow velocity of radiated sound

$$v_r = \dot{R} = \frac{\ddot{V}}{4\pi r c} \, , \tag{A.14}$$

resulting in the intensity of the sound radiation

$$I = \frac{\rho}{4\pi c}|\ddot{V}|^2 \, , \tag{A.15}$$

at large distances. In Fig.A.2 we plot the time evolution of the volume acceleration squared (to which sound radiation intensity is proportional) for five trajectories, generated by smooth *viscosity-induced* end of the collapse. What one can see from those figures is that the sound radiation has a sharp peak at certain moment, which becomes much more pronounced as the viscosity is reduced toward its critical value mentioned above. This peak in the sound emission represents the "mini-bang" we are discuss in Chapter 5.
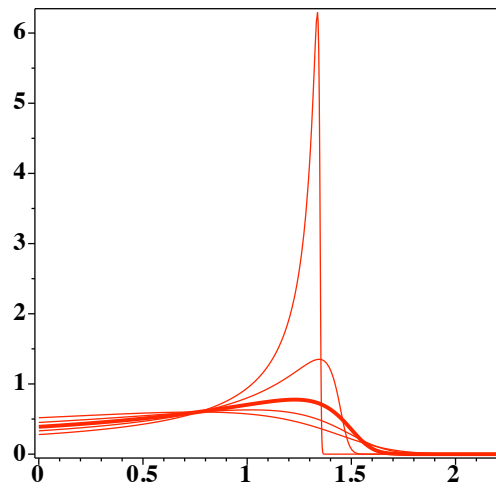
Figure A.2: The time evolution of the quantity $|\ddot{V}(t)|^2$, entering the sound radiation intensity, for the values of $\eta/\rho = 0.06, 0.07, 0.08, 0.09, 0.1$.

Bibliography

[1] E. Rutherford, *The scattering of alpha and beta particles by matter and the structure of the atom*, *Phil.Mag.* **21** (1911) 669–688.

[2] M. Gell-Mann, *Symmetries of baryons and mesons*, *Phys.Rev.* **125** (1962) 1067–1084.

[3] M. Gell-Mann, *A Schematic Model of Baryons and Mesons*, *Phys.Lett.* **8** (1964) 214–215.

[4] Y. Ne'eman, *Derivation of strong interactions from a gauge invariance*, *Nucl.Phys.* **26** (1961) 222–229.

[5] D. Gross and F. Wilczek, *Ultraviolet Behavior of Nonabelian Gauge Theories*, *Phys.Rev.Lett.* **30** (1973) 1343–1346.

[6] H. D. Politzer, *Reliable Perturbative Results for Strong Interactions?*, *Phys.Rev.Lett.* **30** (1973) 1346–1349.

[7] S. Bethke, *Experimental tests of asymptotic freedom*, *Prog.Part.Nucl.Phys.* **58** (2007) 351–386, [hep-ex/0606035].

[8] E. V. Shuryak, *Quantum Chromodynamics and the Theory of Superdense Matter*, *Phys.Rept.* **61** (1980) 71–158.

[9] U. W. Heinz and M. Jacob, *Evidence for a new state of matter: An Assessment of the results from the CERN lead beam program*, nucl-th/0002042.

[10] **BRAHMS Collaboration** Collaboration, I. Arsene *et al.*, *Quark gluon plasma and color glass condensate at RHIC? The Perspective from the BRAHMS experiment*, *Nucl.Phys.* **A757** (2005) 1–27, [nucl-ex/0410020].

[11] **PHENIX Collaboration** Collaboration, K. Adcox *et al.*, *Formation of dense partonic matter in relativistic nucleus-nucleus collisions at RHIC: Experimental evaluation by the PHENIX collaboration*, *Nucl.Phys.* **A757** (2005) 184–283, [nucl-ex/0410003].

[12] B. Back, M. Baker, M. Ballintijn, D. Barton, B. Becker, *et al.*, *The PHOBOS perspective on discoveries at RHIC*, *Nucl.Phys.* **A757** (2005) 28–101, [nucl-ex/0410022].

[13] **STAR Collaboration** Collaboration, J. Adams *et al.*, *Experimental and theoretical challenges in the search for the quark gluon plasma: The STAR Collaboration's critical assessment of the evidence from RHIC collisions*, *Nucl.Phys.* **A757** (2005) 102–183, [nucl-ex/0501009].

[14] F. Karsch, *Lattice QCD at high temperature and density*, *Lect.Notes Phys.* **583** (2002) 209–249, [hep-lat/0106019].

[15] G. Policastro, D. Son, and A. Starinets, *The Shear viscosity of strongly coupled N=4 supersymmetric Yang-Mills plasma*, *Phys.Rev.Lett.* **87** (2001) 081601, [hep-th/0104066].

[16] P. Kovtun, D. Son, and A. Starinets, *Viscosity in strongly interacting quantum field theories from black hole physics*, *Phys.Rev.Lett.* **94** (2005) 111601, [hep-th/0405231].

[17] J. M. Maldacena, *The Large N limit of superconformal field theories and supergravity*, *Adv.Theor.Math.Phys.* **2** (1998) 231–252, [hep-th/9711200].

[18] D. Teaney, J. Lauret, and E. Shuryak, *A Hydrodynamic description of heavy ion collisions at the SPS and RHIC*, nucl-th/0110037.

[19] D. Teaney, J. Lauret, and E. V. Shuryak, *Flow at the SPS and RHIC as a quark gluon plasma signature*, *Phys.Rev.Lett.* **86** (2001) 4783–4786, [nucl-th/0011058].

[20] C. Nonaka and S. A. Bass, *Space-time evolution of bulk QCD matter*, *Phys.Rev.* **C75** (2007) 014902, [nucl-th/0607018].

[21] T. Hirano and Y. Nara, *Eccentricity fluctuation effects on elliptic flow in relativistic heavy ion collisions*, *Phys.Rev.* **C79** (2009) 064904, [0904.4080].

[22] D. A. Teaney, *Viscous Hydrodynamics and the Quark Gluon Plasma*, 0905.2433.

[23] B. Alver and G. Roland, *Collision geometry fluctuations and triangular flow in heavy-ion collisions*, *Phys.Rev.* **C81** (2010) 054905, [1003.0194].

[24] J. Jia, *Measurement of elliptic and higher order flow from ATLAS experiment at the LHC*, *J.Phys.* **G38** (2011) 124012, [1107.1468].

[25] **PHENIX Collaboration** Collaboration, A. Adare *et al.*, *Measurements of Higher-Order Flow Harmonics in Au+Au Collisions at $\sqrt{s_{NN}} = 200$ GeV*, *Phys.Rev.Lett.* **107** (2011) 252301, [1105.3928].

[26] **ALICE Collaboration** Collaboration, K. Aamodt *et al.*, *Harmonic decomposition of two-particle angular correlations in Pb-Pb collisions at $\sqrt{s_{NN}} = 2.76$ TeV*, *Phys.Lett.* **B708** (2012) 249–264, [1109.2501].

[27] **CMS Collaboration** Collaboration, S. Chatrchyan *et al.*, *Centrality dependence of dihadron correlations and azimuthal anisotropy harmonics in PbPb collisions at $\sqrt{s_{NN}} = 2.76$ TeV*, *Eur.Phys.J.* **C72** (2012) 2012, [1201.3158].

[28] **ATLAS Collaboration** Collaboration, G. Aad *et al.*, *Measurement of the azimuthal anisotropy for charged particle production in $\sqrt{s_{NN}} = 2.76$ TeV lead-lead collisions with the ATLAS detector*, *Phys.Rev.* **C86** (2012) 014907, [1203.3087].

[29] **STAR Collaboration** Collaboration, L. Adamczyk *et al.*, *Third Harmonic Flow of Charged Particles in Au+Au Collisions at sqrtsNN = 200 GeV*, 1301.2187.

[30] P. Staig and E. Shuryak, *The Fate of the Initial State Fluctuations in Heavy Ion Collisions. II The Fluctuations and Sounds*, *Phys.Rev.* **C84** (2011) 034908, [1008.3139].

[31] P. Staig and E. Shuryak, *The Fate of the Initial State Fluctuations in Heavy Ion Collisions. III The Second Act of Hydrodynamics*, *Phys.Rev.* **C84** (2011) 044912, [1105.0676].

[32] P. Staig and E. Shuryak, *Sound Propagation on Top of the Fireball*, 1109.6633.

[33] E. Shuryak and P. Staig, *The Sounds of the QCD Phase Transition*, 1306.2938.

[34] S. S. Gubser, *Symmetry constraints on generalizations of Bjorken flow*, *Phys.Rev.* **D82** (2010) 085027, [1006.0006].

[35] S. S. Gubser and A. Yarom, *Conformal hydrodynamics in Minkowski and de Sitter spacetimes*, *Nucl.Phys.* **B846** (2011) 469–511, [1012.1314].

[36] J. Bjorken, *Highly Relativistic Nucleus-Nucleus Collisions: The Central Rapidity Region*, *Phys.Rev.* **D27** (1983) 140–151.

[37] M. L. Miller, K. Reygers, S. J. Sanders, and P. Steinberg, *Glauber modeling in high energy nuclear collisions*, *Ann.Rev.Nucl.Part.Sci.* **57** (2007) 205–243, [nucl-ex/0701025].

[38] R. C. Barret and D. F. Jackson, *Nuclear Sizes and Structure*. Clarendon Press Oxford, 1977.

[39] D. Kharzeev, C. Lourenco, M. Nardi, and H. Satz, *A Quantitative analysis of charmonium suppression in nuclear collisions*, *Z.Phys.* **C74** (1997) 307–318, [hep-ph/9612217].

[40] Z. Qiu and U. W. Heinz, *Event-by-event shape and flow fluctuations of relativistic heavy-ion collision fireballs*, *Phys.Rev.* **C84** (2011) 024911, [1104.0650].

[41] B. Alver, M. Baker, C. Loizides, and P. Steinberg, *The PHOBOS Glauber Monte Carlo*, 0805.4411.

[42] B. Blaettel, G. Baym, L. Frankfurt, H. Heiselberg, and M. Strikman, *Cross-section fluctuations, inelastic Glauber shadowing and ultrarelativistic heavy ion collisions*, *Nucl.Phys.* **A544** (1992) 479C–482C.

[43] G. Baym, B. Blattel, L. Frankfurt, H. Heiselberg, and M. Strikman, *Correlations and fluctuations in high-energy nuclear collisions*, *Phys.Rev.* **C52** (1995) 1604–1617, [nucl-th/9502038].

[44] H. Petersen, G.-Y. Qin, S. A. Bass, and B. Muller, *Triangular flow in event-by-event ideal hydrodynamics in Au+Au collisions at $\sqrt{s_{\mathrm{NN}}} = 200A$ GeV*, *Phys.Rev.* **C82** (2010) 041901, [1008.0625].

[45] B. Schenke, S. Jeon, and C. Gale, *Elliptic and triangular flow in event-by-event (3+1)D viscous hydrodynamics*, *Phys.Rev.Lett.* **106** (2011) 042301, [1009.3244].

[46] F. G. Gardim, F. Grassi, M. Luzum, and J.-Y. Ollitrault, *Anisotropic flow in event-by-event ideal hydrodynamic simulations of $\sqrt{s_{NN}} = 200$ GeV Au+Au collisions*, *Phys.Rev.Lett.* **109** (2012) 202302, [1203.2882].

[47] D. Teaney and L. Yan, *Triangularity and Dipole Asymmetry in Heavy Ion Collisions*, Phys.Rev. **C83** (2011) 064904, [1010.1876].

[48] D. Teaney and L. Yan, *Non linearities in the harmonic spectrum of heavy ion collisions with ideal and viscous hydrodynamics*, Phys.Rev. **C86** (2012) 044908, [1206.1905].

[49] S. Mrowczynski and E. V. Shuryak, *Elliptic flow fluctuations*, Acta Phys.Polon. **B34** (2003) 4241–4256, [nucl-th/0208052].

[50] S. S. Gubser, S. S. Pufu, and A. Yarom, *Entropy production in collisions of gravitational shock waves and of heavy ions*, Phys.Rev. **D78** (2008) 066014, [0805.1551].

[51] F. Karsch, E. Laermann, and A. Peikert, *The Pressure in two flavor, (2+1)-flavor and three flavor QCD*, Phys.Lett. **B478** (2000) 447–455, [hep-lat/0002003].

[52] **ALICE Collaboration** Collaboration, K. Aamodt *et al.*, *Centrality dependence of the charged-particle multiplicity density at mid-rapidity in Pb-Pb collisions at $\sqrt{s_{NN}} = 2.76$ TeV*, Phys.Rev.Lett. **106** (2011) 032301, [1012.1657].

[53] I. Gradshtein and Ryzhik, *Table of Integrals, Series and Products*. 1965.

[54] L. D. Landau and E. M. Lifshitz, *Fluid Mechanics*. 1959.

[55] R. A. Lacey, Y. Gu, X. Gong, D. Reynolds, N. Ajitanand, *et al.*, *Is anisotropic flow really acoustic?*, 1301.0165.

[56] F. Cooper and G. Frye, *Comment on the Single Particle Distribution in the Hydrodynamic and Statistical Thermodynamic Models of Multiparticle Production*, Phys.Rev. **D10** (1974) 186.

[57] U. W. Heinz, *Concepts of heavy ion physics*, hep-ph/0407360.

[58] B. Schenke, S. Jeon, and C. Gale, *(3+1)D hydrodynamic simulation of relativistic heavy-ion collisions*, Phys.Rev. **C82** (2010) 014903, [1004.1408].

[59] P. Ruuskanen, *TRANSVERSE HYDRODYNAMICS WITH A FIRST ORDER PHASE TRANSITION IN VERY HIGH-ENERGY NUCLEAR COLLISIONS*, Acta Phys.Polon. **B18** (1987) 551.

[60] A. Adare, *Triggered di-hadron correlations in Pb-Pb collisions from the ALICE experiment, J.Phys.* **G38** (2011) 124091, [1107.0285].

[61] **STAR Collaboration** Collaboration, M. Aggarwal *et al.*, *Azimuthal di-hadron correlations in d+Au and Au+Au collisions at $\sqrt{s_{NN}} = 200$ GeV from STAR, Phys.Rev.* **C82** (2010) 024912, [1004.2377].

[62] **WMAP Collaboration** Collaboration, E. Komatsu *et al.*, *Seven-Year Wilkinson Microwave Anisotropy Probe (WMAP) Observations: Cosmological Interpretation, Astrophys.J.Suppl.* **192** (2011) 18, [1001.4538].

[63] R. Lacey, *Phenix measurements of higher-order flow harmonics in au+au collisions at $root_s = 200 gev$, Talk at Quark Matter* (2011).

[64] **STAR Collaboration** Collaboration, P. Sorensen, *Higher Flow Harmonics in Heavy Ion Collisions from STAR, J.Phys.* **G38** (2011) 124029, [1110.0737].

[65] Y. Hama, R. P. Andrade, F. Grassi, J. Noronha, and W.-L. Qian, *Further results on peripheral-tube model for ridge correlation, Acta Phys.Polon.Supp.* **6** (2013) 513–518, [1212.6554].

[66] J. Kapusta, B. Muller, and M. Stephanov, *Relativistic Theory of Hydrodynamic Fluctuations with Applications to Heavy Ion Collisions, Phys.Rev.* **C85** (2012) 054906, [1112.6405].

[67] E. V. Shuryak, *Event per event analysis of heavy ion collisions and thermodynamical fluctuations, Phys.Lett.* **B423** (1998) 9–14, [hep-ph/9704456].

[68] M. A. Stephanov, K. Rajagopal, and E. V. Shuryak, *Signatures of the tricritical point in QCD, Phys.Rev.Lett.* **81** (1998) 4816–4819, [hep-ph/9806219].

[69] J. Casalderrey-Solana, E. Shuryak, and D. Teaney, *Conical flow induced by quenched QCD jets, J.Phys.Conf.Ser.* **27** (2005) 22–31, [hep-ph/0411315].

[70] M. P. Brenner, S. Hilgenfeldt, and D. Lohse, *Single-bubble sonoluminescence, Rev.Mod.Phys.* **74** (2002) 425–484.

[71] **PHOBOS Collaboration** Collaboration, B. Alver *et al.*, *System size dependence of cluster properties from two-particle angular correlations in*

Cu+Cu and Au+Au collisions at s(NN)**(1/2) = 200-GeV, Phys.Rev. **C81** (2010) 024904, [0812.1172].

[72] **ALICE collaboration** Collaboration, J. F. Grosse-Oetringhaus,
Hadron Correlations Measured with ALICE, 1208.1445.